

B.Sc. in Mechanical Engineering Thesis

# **RISING DYNAMICS OF AN INITIALLY SPHERICAL BUBBLE IN QUIESCENT LIQUID BOUNDED BY A CORNER**

A thesis submitted by

**S. M. Mahfuzul Hasan**  
**1610082**

**Hasan Tareq Mahin**  
**1610043**

Submitted in partial fulfillment of the requirements for the degree of Bachelor of Science in  
Mechanical Engineering

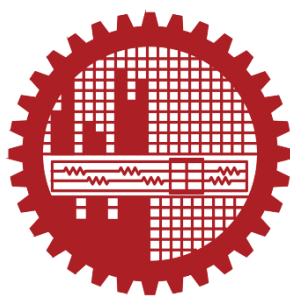
Under the supervision of

**Dr. A. B. M. Toufique Hasan**

Professor

Department of Mechanical Engineering

Bangladesh University of Engineering and Technology



BANGLADESH UNIVERSITY OF ENGINEERING AND TECHNOLOGY

DHAKA, BANGLADESH

MAY 2022

## **DECLARATION**

This is to certify that the work presented in this thesis, titled, “RISING DYNAMICS OF AN INITIALLY SPHERICAL BUBBLE IN QUIESCENT LIQUID BOUNDED BY A CORNER”, is the outcome of the investigation and research carried out by us under the supervision of Dr. A. B. M. Toufique Hasan.

This is hereby declared that this thesis or any part of this thesis has not been submitted elsewhere for the award of any degree or diploma.

.....

S. M. Mahfuzul Hasan

1610082

.....

Hasan Tareq Mahin

1610043

# CERTIFICATION

This thesis titled, "**RISING DYNAMICS OF AN INITIALLY SPHERICAL BUBBLE IN QUIESCENT LIQUID BOUNDED BY A CORNER**", submitted by the group as mentioned below has been accepted as satisfactory in partial fulfillment of the requirements for the degree B.Sc. in Mechanical Engineering in May 2022.

**Group Members:**

**S. M. Mahfuzul Hasan**

**Hasan Tareq Mahin**

**Supervisor:**

.....  
Dr. A. B. M. Toufique Hasan  
Professor  
Department of Mechanical Engineering  
Bangladesh University of Engineering and Technology

## **ACKNOWLEDGEMENT**

All the praises to the Almighty Allah. Without His wish, this work wouldn't have been possible to accomplish.

We would like to express our sincere gratitude to our supervisor, Dr. A. B. M. Toufique Hasan for encouraging us to take upon this endeavor of exploring a completely unknown and then-unfathomable topic and platform as our thesis. His constant support to have the aspiration of keep doing the good work no matter how hard and tough the situations become worked as a major factor in completing this thesis. His suggestions and criticisms helped us immensely to get a grip on the methodology that constitute research. We are immensely grateful to him for letting us have the lab facilities to carry out the computational work that would hardly be possible otherwise.

Special thanks to Stéphane Popinet and others for developing a wonderful fluid flow solver, specially for interfacial flow *Basilisk* and other community members who contributed and is contributing to the constant development of this software program.

Lastly, we are forever indebted to our respective families for always supporting us through thick and thin and never giving up on us. We are here at this stage because of them.

The present study has been carried out with computational resource support from Higher Education Quality Enhancement Project (HEQEP), AIF (2nd Round)-Sub-Project CP 3111, UGC, MoE, Government of Bangladesh (Contract No. 34/2014).

## **ABSTRACT**

Three-dimensional numerical simulations are performed to study two-wall effect on the dynamics of rising bubble in quiescent liquid. The phenomena associated with the dynamics of a rising bubble that are investigated in present study are bubble trajectory, shape, velocity and vorticity. An effort is made to establish the intimate connections between these phenomena and how two vertical walls act as a destabilizing factor in the behavior of a rising bubble. A finite volume approach coupled with VOF (volume-of-fluid) method is employed to solve the Navier-Stokes and volume fraction equation simultaneously to achieve the numerical results. From the study, it is found that two vertical walls induce path instability along with diagonal migration of bubble in three-dimensional space and critical value of conditional parameter, Galilei number is found at which the path instability occurs. The critical value is found to be lower than what it is for unbounded situation. Also, the onset of spiraling motion, that is of great interest for the study of bubble dynamics, is achieved pretty earlier in the oscillating bubble regime which further testifies the instability induced by bubble-walls interaction. Wake structure is found to be major factor at influencing other phenomena associated with dynamics of rising bubble. Bubble inertia is greatly affected because of the wakes formed between the bubble and walls at initial phases and this proves to be crucial at later time for bubble to conform to a particular rising motion.

# Nomenclature

$\rho$	Density
$\mathbf{u}$	Velocity field
$p$	Pressure
$t$	Time
$\mu$	Dynamic viscosity
$\sigma$	Interfacial tension
$\kappa$	Interfacial curvature
$\mathbf{g}$	Gravitational acceleration
$c$	Volume fraction
$d$	Bubble diameter
$Ga$	Galilei number
$Eo$	Eötvös number
$Mo$	Morton number
$Re$	Reynolds number
$We$	Weber number
$D$	Deformation tensor
$A$	Amplitude
$f$	Frequency
$\delta$	Percentage difference
$x$	Bubble position along x axis
$y$	Bubble position along y axis
$z$	Bubble position along z axis
$u$	Bubble velocity
$F$	Dimensionless wall force
$\omega$	Streamwise vorticity

## Subscript

$n$	Normal direction
$t, r$	Tangential direction
$l$	Liquid
$g$	Gas
$r$	Ratio
$x$	x- component
$y$	y- component
$z$	z- component
$c$	Center

# Contents

<b>DECLARATION.....</b>	i
<b>CERTIFICATION.....</b>	ii
<b>ACKNOWLEDGEMENT.....</b>	iii
<b>ABSTRACT.....</b>	iv
<b>Nomenclature .....</b>	v
<b>List of Figures.....</b>	viii
<b>List of Tables .....</b>	xii
<b>CHAPTER 1</b>	
<b>INTRODUCTION.....</b>	1
<b>1.1 Background .....</b>	1
<b>1.2 Motivation.....</b>	3
<b>1.3 Objectives.....</b>	4
<b>1.4 Outline of the thesis .....</b>	4
<b>CHAPTER 2</b>	
<b>LITERATURE REVIEW .....</b>	5
<b>CHAPTER 3</b>	
<b>COMPUTATIONAL METHOD.....</b>	8
<b>3.1 Basics of CFD .....</b>	8
<b>3.2 Applications of CFD .....</b>	8
<b>3.3 Strategy of CFD.....</b>	9
<b>3.3.1 Discretization.....</b>	9
<b>3.4 Basilisk .....</b>	10
<b>3.4.1 Grids.....</b>	10
<b>3.4.2 Tree-based Grid Adaptivity .....</b>	12
<b>3.4.3 Fields and Stencils.....</b>	13
<b>3.4.4 Boundary Conditions.....</b>	13

<b>3.5 Formulation.....</b>	14
<b>3.5.1 Governing Equations .....</b>	14
<b>3.5.2 Numerical Technique.....</b>	16
<b>3.5.3 Geometry .....</b>	19
<b>3.5.3.1 Computational Domain .....</b>	19
<b>3.5.3.2 Parameters Definition.....</b>	20
<b>3.5.3.3 Mesh .....</b>	21
<b>3.5.3.4 Boundary Conditions.....</b>	27
<b>3.6 Validation.....</b>	27
<b>3.6.1 Grid Independence Test .....</b>	27
<b>3.6.2 Unbounded Condition.....</b>	29
<b>3.6.2.1 Comparison with Experimental Results .....</b>	29
<b>3.6.2.2 Comparison with Numeral Simulation .....</b>	30
<b>3.6.3 With Vertical Wall.....</b>	32

## CHAPTER 4

<b>RESULTS AND DISCUSSION .....</b>	37
<b>4.1 Case-1 (Ga = 40).....</b>	38
<b>4.2 Case-2 (Ga = 55).....</b>	44
<b>4.3 Case-3 (Ga = 57).....</b>	51
<b>4.4 Case-4 (Ga = 60).....</b>	58
<b>4.5 Case-5 (Ga = 61).....</b>	64
<b>4.6 Case-6 (Ga = 62).....</b>	71
<b>4.7 Case-7 (Ga = 63.36).....</b>	77
<b>4.8 Case-8 (Ga = 70).....</b>	84
<b>4.9 Case-9 (Ga = 90.51).....</b>	91

<b>CHAPTER 5 .....</b>	101
------------------------	-----

<b>CONCLUSIONS .....</b>	101
--------------------------	-----

<b>Recommendations .....</b>	102
------------------------------	-----

<b>References.....</b>	103
------------------------	-----

# List of Figures

Figure 1.1: Collected pictures of (a) agitated stream of rising bubbles underwater (b) liquid sand-air fluidized bed system (luminous substances are air bubbles). ....	1
Figure 1.2: Experiments on different bubbles (a) Single-threaded wake behind a rectilinear rising bubble [1] (b) Train of bubble rising for a constant flow rate of air in a nozzle [2] .....	2
Figure 3.1: Typical discretization of domain in CFD .....	9
Figure 3.2: (a) sample uniform grid (b) sample non-uniform grid [Higher-order adaptive methods for fluid dynamics] (c) sample adaptive grid.....	11
Figure 3.3: Multigrid structure (combination of different levels of refinement) .....	11
Figure 3.4: (a) Cell arrangement in Tree-grid structure (Quadtree) (b) Equivalent quadtree structure	12
Figure 3.5: $3 \times 3$ stencils.....	13
Figure 3.6: Ghost cells outside boundary with different values than inside cells.....	14
Figure 3.7: Schematic of computational domain (a) Isometric view ( $100d \times 100d \times 100d$ ) domain where d is bubble diameter) (b) Right-side view (c) Front view of the domain. Initial distance of bubble from both rear and left-side wall is $L (= 0.75d)$ . The bubble is kept at $4d$ distance initially as well from the bottom wall so that the bottom wall has no effect on the dynamics. It is to be noted that bubble size is exaggerated for better visibility since the actual bubble size is way too small compared to domain...	19
Figure 3.8: Spatio-temporal evolution of grid in and around bubble at $t = 0, 1, 2, 3, 5, 6$ for case-7 ( $Ga = 63.36, Eo = 16, \rho_r = 1000, \mu_r = 100$ ). Red solid line represents bubble surface. ....	26
Figure 3.9: Grid dependency test for two different maximum level of refinement (a) <i>level 12</i> (b) <i>level 13</i> at $t = 9$ . For <i>level 12</i> , smallest grid size is $\Delta x = \Delta y = 0.0244$ and for <i>level 13</i> , smallest grid size is $\Delta x = \Delta y = 0.0122$ . Two refinement criteria implemented are velocity field and bubble surface. ....	27
Figure 3.10: Effect on bubble shapes for two different maximum level of refinement at $t = 9$ . Green and red solid lines correspond to bubble surface for <i>level 12</i> and <i>level 13</i> respectively. ....	28
Figure 3.11: Time histories of Reynolds number for two different refinement level. It further shows that coarser grid induces instability earlier and persists longer than finer grid though the terminal Reynolds number converges to a certain magnitude.....	28
Figure 3.12: Comparison between terminal Reynolds number obtained from Bhaga and Weber [8] and present simulation. ....	29
Figure 3.13: Comparison of terminal bubble shape from present simulation to Bhaga and Weber [8].... (a) $Eo = 116, Mo = 5.51$ (b) $Eo = 339, Mo = 43.1$ (c) $Eo = 116, Mo = 0.103$ (d) $Eo = 115, Mo = 4.63 \times 10^{-3}$ . Red solid lines correspond to bubble shapes from present simulation. ....	30
Figure 3.14: (a) Variation of $x_c$ along vertical path $y_c$ (front view of bubble trajectory) (b) Variation of $z_c$ along vertical path $y_c$ (right side view of bubble trajectory). ....	31

Figure 3.15: Spatio-temporal variation of bubble shapes (a) top view (b) right side view (c) front view at $t = 10, 20, 30, 40, 50$ . (i), (iii) and (v) correspond to present results and (ii), (iv) and (vi) correspond to results from Zhang et al. [24].....	31
Figure 3.16: Iso-contours of the streamwise vorticity $\omega_y = \pm 0.15$ at $t = 20, 40$ from (i) present simulation (ii) Zhang et al. [24].....	32
Figure 3.17: Schematic of the computational domain as illustrated in Zhang et al. [24], where domain is $100d \times 100d \times 100d$ , distance from wall in x- direction $S = 0.75d$ , distance from bottom wall in y-direction is $4d$ , and the parameters are taken as $Ga = 90.51$ , $Eo = 16$ , $\rho_r = 1000$ , $\mu_r = 100$ for both unbounded and wall conditions.....	32
Figure 3.18: (a) Variation of $x_c$ along vertical path $y_c$ (front view of bubble trajectory) (b) Variation of $z_c$ along vertical path $y_c$ (right side view of bubble trajectory).....	33
Figure 3.19: Time histories of (a) x- velocity component (b) y- velocity component (c) z- velocity component.....	34
Figure 3.20: Time histories of non-dimensional force in the wall-normal direction on bubble. ....	35
Figure 3.21: Spatio-temporal variation of bubble shapes (a) top view (b) right side view (c) front view at $t = 10, 20, 30, 40, 50$ . (i), (iii) and (v) correspond to present results and (ii), (iv) and (vi) correspond to results from Zhang et al. [24].....	35
Figure 3.22: Iso-contours of the streamwise vorticity $\omega_y = \pm 0.15$ at $t = 20, 40$ from (i) present simulation (ii) Zhang et al. [24].....	36
Figure 4.1: (a) Variation of $x_c$ (front view of bubble trajectory) and $z_c$ (side view of bubble trajectory) along $y_c$ (b) Top view of bubble trajectory (c) Three-dimensional bubble trajectory.....	38
Figure 4.2: Time histories of (a) x- component and z- component of velocity (b) y- component of velocity (c) Reynolds number.....	39
Figure 4.3: Spatio-temporal variation of bubble shape in rear, left-side and bottom view (from left to right) at $t = 1, 2, 3, 5, 7, 9, 10, 15, 20, 25, 30, 40, 60$ .....	41
Figure 4.4: Rear (left) and left-side (right) view of iso-contours of spatio-temporal variation of streamwise vorticity $\omega_y = \pm 0.15$ ( $\omega_y = +0.15$ for green and $\omega_y = -0.15$ for red) at $t = 1, 2, 3, 5, 7, 9, 10, 15, 20, 25, 30, 40, 60$ .....	43
Figure 4.5: (a) Variation of $x_c$ (front view of bubble trajectory) and $z_c$ (side view of bubble trajectory) along $y_c$ (b) Top view of bubble trajectory (c) Three-dimensional bubble trajectory.....	44
Figure 4.6: Time histories of (a) x- component and z- component of velocity (b) y- component of velocity (c) Reynolds number.....	45
Figure 4.7: Spatio-temporal variation of bubble shape in rear, left-side and bottom view (from left to right) at $t = 1, 2, 3, 5, 7, 9, 10, 15, 20, 30, 40, 60$ .....	47
Figure 4.8: Rear (left) and left-side (right) view of iso-contours of spatio-temporal variation of streamwise vorticity $\omega_y = \pm 0.15$ ( $\omega_y = +0.15$ for green and $\omega_y = -0.15$ for red) at $t = 1, 2, 3, 5, 7, 9, 10, 15, 20, 30, 40$ .....	49

Figure 4.9: (a) Variation of $x_c$ (front view of bubble trajectory) and $z_c$ (side view of bubble trajectory) along $y_c$ (b) Top view of bubble trajectory (c) Three-dimensional bubble trajectory.....	51
Figure 4.10: Time histories of (a) x- component and z- component of velocity (b) y- component of velocity (c) Reynolds number.....	52
Figure 4.11: Spatio-temporal variation of bubble shape in rear, left-side and bottom view (from left to right) at $t = 1, 2, 3, 5, 7, 10, 20, 30, 40, 50, 60$ .....	54
Figure 4.12: Rear (left) and left-side (right) view of iso-contours of spatio-temporal variation of streamwise vorticity $\omega_y = \pm 0.15$ ( $\omega_y = +0.15$ for green and $\omega_y = -0.15$ for red) at $t = 1, 2, 3, 5, 7, 9, 10, 15, 20, 30, 40$ .....	56
Figure 4.13: (a) Variation of $x_c$ (front view of bubble trajectory) and $z_c$ (side view of bubble trajectory) along $y_c$ (b) Top view of bubble trajectory (c) Three-dimensional bubble trajectory.....	58
Figure 4.14: Time histories of (a) x- component and z- component of velocity (b) y- component of velocity (c) Reynolds number.....	59
Figure 4.15: Spatio-temporal variation of bubble shape in rear, left-side and bottom view (from left to right) at $t = 1, 2, 3, 5, 7, 9, 10, 15, 20, 30, 40$ .....	61
Figure 4.16: Rear (left) and left-side (right) view of iso-contours of spatio-temporal variation of streamwise vorticity $\omega_y = \pm 0.15$ ( $\omega_y = +0.15$ for green and $\omega_y = -0.15$ for red) at $t = 1, 2, 3, 5, 7, 10, 15, 20, 30$ .....	63
Figure 4.17: (a) Variation of $x_c$ (front view of bubble trajectory) and $z_c$ (side view of bubble trajectory) along $y_c$ (b) Top view of bubble trajectory (c) Three-dimensional bubble trajectory.....	64
Figure 4.18: Time histories of (a) x- component and z- component of velocity (b) y- component of velocity (c) Reynolds number.....	65
Figure 4.19: Spatio-temporal variation of bubble shape in rear, left-side and bottom view (from left to right) at $t = 1, 2, 3, 5, 7, 10, 20, 30, 40, 50, 60$ .....	67
Figure 4.20: Rear (left) and left-side (right) view of iso-contours of spatio-temporal variation of streamwise vorticity $\omega_y = \pm 0.15$ ( $\omega_y = +0.15$ for green and $\omega_y = -0.15$ for red) at $t = 1, 2, 3, 5, 7, 9, 10, 15, 20, 30, 40, 60, 70$ .....	69
Figure 4.21: (a) Variation of $x_c$ (front view of bubble trajectory) and $z_c$ (side view of bubble trajectory) along $y_c$ (b) Top view of bubble trajectory (c) Three-dimensional bubble trajectory.....	71
Figure 4.22: Time histories of (a) x- component and z- component of velocity (b) y- component of velocity (c) Reynolds number.....	72
Figure 4.23: Spatio-temporal variation of bubble shape in rear, left-side and bottom view (from left to right) at $t = 1, 2, 3, 5, 7, 10, 20, 30, 40, 60, 70, 80$ .....	74
Figure 4.24: Rear (left) and left-side (right) view of iso-contours of spatio-temporal variation of streamwise vorticity $\omega_y = \pm 0.15$ ( $\omega_y = +0.15$ for green and $\omega_y = -0.15$ for red) at $t = 1, 2, 3, 5, 10, 20, 30, 40, 60, 70$ .....	76

Figure 4.25: (a) Variation of $x_c$ (front view of bubble trajectory) and $z_c$ (side view of bubble trajectory) along $y_c$ (b) Top view of bubble trajectory (c) Three-dimensional bubble trajectory.....	77
Figure 4.26: Time histories of (a) x- component and z- component of velocity (b) y- component of velocity (c) Reynolds number.....	78
Figure 4.27: Spatio-temporal variation of bubble shape in rear, left-side and bottom view (from left to right) at $t = 1, 2, 3, 5, 7, 10, 20, 30, 40, 60, 70$ .....	80
Figure 4.28: Rear (left) and left-side (right) view of iso-contours of spatio-temporal variation of streamwise vorticity $\omega_y = \pm 0.15$ ( $\omega_y = +0.15$ for green and $\omega_y = -0.15$ for red) at $t = 1, 2, 3, 5, 7, 10, 15, 20, 30, 40, 60$ .....	82
Figure 4.29: (a) Variation of $x_c$ (front view of bubble trajectory) and $z_c$ (side view of bubble trajectory) along $y_c$ (b) Top view of bubble trajectory (c) Three-dimensional bubble trajectory.....	84
Figure 4.30: Time histories of (a) x- component and z- component of velocity (b) y- component of velocity (c) Reynolds number.....	85
Figure 4.31: Spatio-temporal variation of bubble shape in rear, left-side and bottom view (from left to right) at $t = 1, 2, 3, 5, 10, 15, 20, 30, 40, 50$ .....	87
Figure 4.32: Rear (left) and left-side (right) view of iso-contours of spatio-temporal variation of streamwise vorticity $\omega_y = \pm 0.15$ ( $\omega_y = +0.15$ for green and $\omega_y = -0.15$ for red) at $t = 1, 5, 10, 20, 30, 40, 50$ .....	89
Figure 4.33: (a) Variation of $x_c$ (front view of bubble trajectory) and $z_c$ (side view of bubble trajectory) along $y_c$ (b) Top view of bubble trajectory (c) Three-dimensional bubble trajectory.....	91
Figure 4.34: Time histories of (a) x- component and z- component of velocity (b) y- component of velocity (c) Reynolds number.....	92
Figure 4.35: Time histories of the dimensionless force in the wall-normal direction.....	93
Figure 4.36: Spatio-temporal variation of bubble shape in rear, left-side and bottom view (from left to right) at $t = 1, 2, 3, 5, 10, 20, 30, 40, 60, 70, 80$ .....	95
Figure 4.37: Rear (left) and left-side (right) view of iso-contours of spatio-temporal variation of streamwise vorticity $\omega_y = \pm 0.15$ ( $\omega_y = +0.15$ for green and $\omega_y = -0.15$ for red) at $t = 1, 2, 5, 10, 20, 30, 50, 70$ .....	97
Figure 4.38: The effect of Galilei number on amplitude and frequency of the lateral (wall-normal direction) oscillation with presence of two walls.....	99
Figure 4.39: Distinct regimes obtained from present study .....	99

# List of Tables

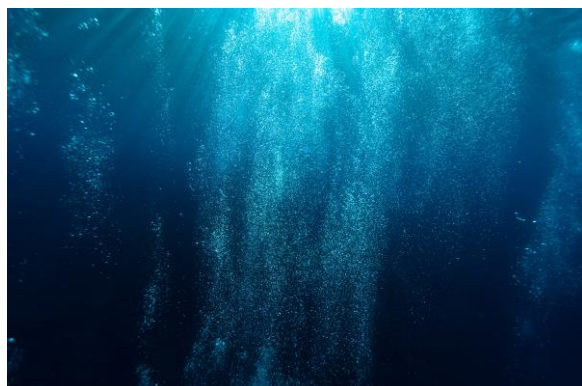
Table 3.1: Comparison between two different maximum levels of refinement.....	28
Table 3.2: Cases validated .....	29
Table 4.1: Total cases studied.....	37
Table 4.2: Identified regimes and corresponding trajectories .....	100

# CHAPTER 1

## INTRODUCTION

### 1.1 Background

Multiphase flow is flow of two or more than two thermodynamic phases that co-exist simultaneously with each other. When the immiscible phases are separated by an interface in a particular multiphase fluid flow system, then it is called interfacial flow. The instances of multiphase flow are significantly abundant in nature and it has a wide range of applications in different fields such as, ocean, nuclear, mechanical, aerospace, chemical engineering. The instances found in chemical reactors, cavitation, multiphase mixture transport, fluidized bed, particle transport in blood, rocket engines, contamination spreading, ink-jet printing, crystallization, multiphase cooling, drying of gases, water treatment by aeration of chemical and biological reactors, air entrainment in oceans/rivers, carbon capture and storage and many more industrial processes. All these applications have called for a good understanding of the physics of bubbles in viscous liquids which have paved ways for researchers to take on the endeavor to study the sheer complex physics of interfacial flow.



(a)



(b)

Figure 1.1: Collected pictures of (a) agitated stream of rising bubbles underwater (b) liquid sand-air fluidized bed system (luminous substances are air bubbles).

Figure 1.1 shows two of the instances of bubbly flow in nature and industry. Figure 1.1a shows flurry bubble rising agitatedly from underwater to ocean surface. This is quite a natural phenomenon that is encountered in ocean engineering. Figure 1.1b shows air bubbles riding up in fluidized bed combustion. It's an experiment done to simulate how bubbly flow occurs in fluidized bed used industrial application.

The complex yet fascinating dynamics of bubble in liquid has been pondered over for a very long time by the researchers. Huge number of works have been conducted to understand the physics of how a bubble behaves at certain conditions both in experimental and numerical studies. For us to delve into the works that inspired us to take on the thesis, first and foremost, it is important to define what a bubble really is.

Bubble can be defined as a globule of one fluid in another. To define it more technically, it can be said that a globule that has lower density than the liquid that is surrounding it, is called a bubble. So, it can be safely said the density ratio that is, the ratio of bubble density and surrounding liquid density is less than 1. As the bubble density is lower than the surrounding liquid, it gets pushed up because of a effect known as *buoyancy*. Consequently, there induces certain dynamics in the bubble rising up due to buoyancy effect. The dynamics is studied in different forms of bubble's behavioral phenomena such as, its path, shapes, velocity, wake induced etc.

The forces that act on a rising bubble are mainly viscous force, gravitational force and buoyancy force. Additionally, surface tension force also acts on the bubble that helps the bubble to retain minimum surface area possible. Other external forces like electric, magnetic forces can act on the bubble depending on the environment. The bubble is separated from its surrounding liquid by an *interface*, also known as *bubble surface*. Because of the interface that exists between the two phases, the corresponding fluid flow is known as interfacial flow.

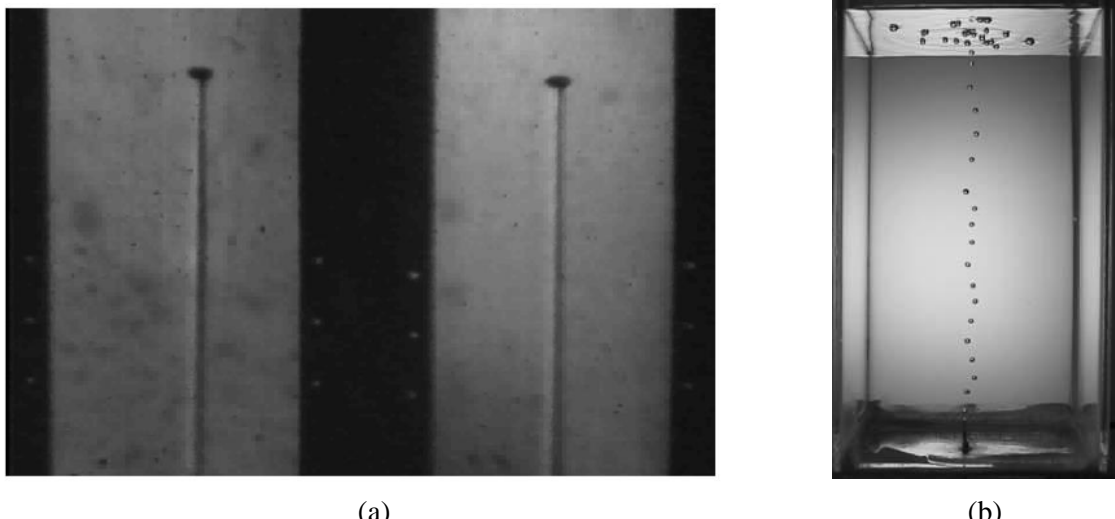


Figure 1.2: Experiments on different bubbles (a) Single-threaded wake behind a rectilinear rising bubble [1] (b) Train of bubble rising for a constant flow rate of air in a nozzle [2]

A number of parameters are to be considered for the description of the dynamics of a single rising bubble viz. the density and viscosity of bubble, the density and viscosity of surrounding liquid, interfacial tension of bubble-liquid interface, gravitational acceleration. For the complexity of handling all these parameters, simplification has to be adopted. As a result, all these parameters are incorporated into four dimensionless number that would give a more general description of the dynamics of rising bubble. These dimensionless parameters are broadly discussed in Chapter 3.

## 1.2 Motivation

The motion of a gas bubble rising due to gravity in a liquid has been studied from many centuries ago and continues to be a problem of great interest today. The first documentation of rising bubble dates back to 1500s when Leonardo da Vinci observed the spiraling motion of rising bubble as pointed out by Ohl et al. [3]. From there, the term *Leonardo's Paradox* became a popular phrase to denote path instability that is the onset of oscillating motion of bubble. Over the past few decades, thousands of published works have made reasonable efforts to integrate different regimes of bubble motion with somewhat mutual models with different range of parameters.

Both experimental and numerical studies were carried out in attempts to get a broader picture of the physics associated with rising bubble. From last century, a great deal of experimental researches of freely rising bubble in unbounded condition were done [4, 5, 6, 7, 8, 9, 10, 11, 12, 13]. Different bubble regimes were identified in those experiments along with significant observations about terminal velocity, shapes and wakes. Path instability got special attention as the bubble deviate from a straight trajectory to a more unstable one like zigzagging or spiraling. Much of the focus was given to find critical aspects causing the path instability and an intimate relation between the wake formed on and behind the bubble and the path instability was reported in various literature.

After the development of numerous numerical techniques and schemes, researches on common models as experimental works were conducted and results echoing the outcome of experimental researches were obtained. It opened a doorway to evaluate rising bubble dynamics in unbounded condition by varying a great range of associated parameters. A remarkable set of papers [14, 15, 16, 17, 18, 19] was published to define different bubble regimes based on bubble shape and path. Path instability was further investigated extensively to acquire a more general understanding of the dynamics.

In recent times, the wall effect on bubble rising dynamics has been a topic of great interest among research community. Some of the works [20, 21, 22, 23, 24] that have been published, though shed a good light on the topic but the understanding of near-wall bubble behavior is far from being complete. Most of the researches till now to observe wall effect are for single bubble near a vertical wall. To the best of our knowledge, there is not still any significant work done on the effect of two vertical walls that adjoin to form a corner on a single bubble. We believe, the difference in effect between single vertical wall and two vertical walls will provide another dimension in the understanding of near-wall behavior of a rising bubble. As the dynamics against a vertical wall is actively being researched, extending the complexity by adding another vertical wall to form a corner can prove to unravel the yet unknown aspect of near-wall behavior of a rising bubble.

So, based on the works done by other researchers till date, we embarked upon taking up a thesis that focuses on the dynamics of a single rising bubble in quiescent liquid with two adjoining vertical walls that form a corner. We conduct a fully 3D simulation to study the dynamics of a rising bubble in the vicinity of two adjoining vertical walls that form a corner using open-source software program *Basilisk* developed by S. Popinet.

## 1.3 Objectives

The primary objective of our study, in a broader sense, is to observe the dynamics shown by a rising bubble near a corner formed by two adjoining walls. To put it into perspective, some of the key objectives that constitute the primary objective are mentioned below:

- i) Studying paths, shapes, velocity and wakes of rising bubble near two vertical walls for different cases based on varied parameters.
- ii) Establishing a general understanding of interconnectedness among the behavioral phenomena shown by the rising bubble near walls.
- iii) Identifying distinct regimes based on bubble trajectory.
- iv) Studying path instability due to bubble-walls interaction and finding the exact value of parameter (Galilei number) given other parameters remain constant for which the path instability is fully developed.

All in all, a number of 3D numerical simulations were performed to study the rising dynamics of a bubble near a corner.

## 1.4 Outline of the thesis

The next chapter, *Chapter 2*, gives an overview of the works done by other researchers so far to study the complex nature of dynamics of rising bubble. It discusses the phenomena already established today through clinical literatures, the active works that are still going on to address some more obscure phenomena correspond to rising dynamics of bubble. Near-wall behaviors of bubble are also reported and the evolution of such studies in recent times.

In *Chapter 3*, numerical methods and formulations are described in great details. The techniques to solve Navier-Stokes equations along with a volume fraction equation were discussed rigorously to get into the unknown aspect of how the numerical solvers work. We deployed the partial differential equations solver *Basilisk* throughout our study and used open-source code to obtain the results. Next, The validation of both experimental and numerical works done by other researchers was done extensively to test the results from our numerical solver against the outcome obtained by the said researchers.

In *Chapter 4*, we present the results of our current study and discuss the phenomena observed. The parameters in use- *density ratio*, *viscosity ratio*, *Eötvös number* and *Galilei number* are varied where first three of the mentioned parameters are kept constant at certain values and only Galilei number is varied. The increasing Galilei number showcases different overall dynamics of the bubble and those variations are discussed briefly for every simulation done. We shed light on to the achievement of the abovementioned objectives in section 1.3 and provide reasoning for the physics involved while achieving such targets.

*Chapter 5* draws the conclusions of our study and points out the findings from our study. Further remarks are made about the future works that can be carried out from this study.

# CHAPTER 2

## LITERATURE REVIEW

A great deal of works has been accomplished both experimentally and numerically on bubble dynamics. Bubble shape, path, rising velocity, wake structures are the features that have been researched extensively and findings have been published in some excellent piece of works.

Haberman and Morton [4] first undertook a fundamental study of bubbles in various liquids experimentally. They argued that complete description of air bubbles motion couldn't be possible by using non-dimensional parameters containing the usual physical properties of liquids (viz. density, surface tension, viscosity). They also identified three types of bubble shapes viz. spherical, ellipsoidal, spherical cap. They also presented an effect of container wall on bubble's rising velocity. Following their work, there were a stream of experimental works that were published. Saffman [5] conducted an experiment on bubble trajectory with an initial bubble shape of oblate spheroids instead of spherical and he identified three regimes of trajectory viz. rectilinear, zigzag, and uniform spiral. He also pointed out that the regime of trajectory is dependent on the size of the bubble. Hartunian and Sears [6] conducted an experimental and theoretical study to measure the size and terminal velocity of small gas bubbles at threshold of path instability (i.e. path of rising bubble stops following a vertical straight line and switches to zigzag or spiral motion). He specified two separate criteria for the onset of bubble instability and presented a stability curve. Tsuge and Hibino [7] performed similar experimental study to obtain the onset of bubble oscillatory motion.

Bhaga and Weber [8] found tremendous experimental results upon using various air bubble-aqueous sugar solution systems. They identified several findings- including various shape regimes (viz. oblate ellipsoidal, oblate ellipsoidal cap, spherical cap, skirted), correlation between terminal velocity and shapes regimes, wake structure around bubble. They implemented a *hydrogen bubble tracer* technique to visualize flow field around rising bubble. They prepared a plot of bubble shape regimes on a *Eo-Re* plane which proves to be very important in later researches. Duineveld [9] experimented on bubble shapes and velocities at high Reynolds number using *hyper clean* water that gave him good agreement with theoretical results for small bubbles but not for large bubbles. Other researchers also conducted experiments to study path instability by observing terminal velocity [10], shape oscillations [11], streamwise vorticity [12].

de Vries et al. (2002) [13] focused on the wake structure at high Reynolds number using a *Schlieren* optics technique. They measured the magnitude of lift force experienced by bubble because of the wake structure in zigzagging or spiraling bubble. They also performed experiments to observe the collision between the bubble and vertical wall which affected the already established wake structure to a more coherent one.

Path instability, though, has been investigated extensively in modern times, the discovery of the phenomenon dates way back when Leonardo Da Vinci noted it in his notebook as mentioned by Ohl et al. [3]. Three-dimensional numerical simulations have been performed to study the dynamics of bubble, more specifically, the path instability. Bunner and Tryggvason [14] carried out three-dimensional simulation of evolution of 91 bubbles by solving the Navier-Stokes equation by front tracking/finite

difference method. Magnaudet and Mougin [15] studied wake instability by carrying out Direct Numerical Simulation (DNS) of flow past a fixed oblate spheroidal bubble. They found a critical aspect ratio (the length ratio of major axis to minor axis) for which the onset of instability occurs as aspect ratio of bubble is a function of the strength of vorticity at surface. They used a finite-volume scheme through code developed by themselves.

Cano-Lozano et al. [16] similarly used a fixed axisymmetric but a bubble of realistic shape to determine a neutral curve to detect the onset of path instability. They also reported that the fore-and-aft asymmetry of the axisymmetric bubble is a relevant parameter that affects the strength of the azimuthal vorticity along the neutral curve. They used *Gerris Flow Solver* to perform the simulations and further with the shape and terminal velocity obtained they performed three-dimensional, incompressible numerical simulation of flow around the bubble by using *OpenFoam*. They continued their investigation by implementing a global Linear Stability Approach (LSA) to the bubble of fore-aft asymmetric shape [18] extending the work of Tchoufag et al. [25, 26] simulating free rising of nearly spheroidal deformable bubble that focused on bubble with oblate spheroidal or spheroidal shape. Both fixed and freely rising bubble were simulated and effect of shape asymmetry on wake instability was reported. *FreeFem++* [New development in FreeFem++] was used to implement the LSA approach after simulation using *Gerris Flow Solver*. On their following work [17], they provided a phase diagram on Bo-Ga plane identifying different regimes of trajectories (viz. rectilinear, planar zigzag, flattened spiral, spiral, chaotic) distinct by critical curves which they again performed on *Gerris Flow Solver*.

Hua and Lou [27] used an improved numerical algorithm for front tracking and *SIMPLE* algorithm for solving Navier-Stokes equation by finite volume method. Gaudlitz and Adams [28] adopted a DNS that used *Hybrid particle-level-set* (HPLS) method [29] in combination with level set methods [30] for description of phase interface instead of purely level set methods.

Tripathi et al. [19] carried out three-dimensional simulation using *Gerris Flow Solver* on bubbles at unbounded condition and generated a phase plot on Ga-Eo plane based on different shapes of bubble. The regimes they identified were typically as- axisymmetric, asymmetric (non-oscillatory and oscillatory), break-up (peripheral and central). They stretched on the point of connection between shape asymmetry and path instability. They didn't embrace the idea of cause and effect between those two phenomena rather chose to believe that both shape asymmetry and path instability goes hand in hand. Sharaf et al. [31] conducted experiments to validate the results obtained by Tripathi et al. [19] and they found very good agreement of the phase plot with that of Tripathi et al. [19] except for they didn't get the central break-up region in their experiments.

While three-dimensional bubble simulation has been extensively researched for decades now, wall effects on bubble dynamics is relatively a newer research interest. Krishna et al. [20] experimentally investigated the wall effect on a bubble in a column and found that the rising velocity of bubble is a function of bubble to column diameter ratio. As the bubble to column diameter ratio increased, bubble motion became progressively retarded. This phenomenon was attributed as *wall effect* on the bubble. Further experiments conducted by Takemura et al. [21] found similar result of bubble motion retardation while the bubble was released in the vicinity of vertical wall and a repulsive lift force caused bubble to move away from wall. It was also noted that wall effect was greater if the initial separation between bubble and wall was smaller.

Takemura and Magnaudet [32] experimented on transverse force induced by wall on bubble for  $0 \leq Re \leq 100$  and concluded that at moderate Reynolds number, wall-induced repulsive force on contaminated spherical bubble was due to interaction of wall with far-field particle wake. They also noted that for  $Re < 35$ , clean spherical bubble always migrated away from wall while for larger values

of  $Re$ , bubble was attracted for most cases based on separation between wall and bubble. Zaruba et al. [33] reported sliding (when the bubble is small) and bouncing motion (under certain experimental parameters). The bouncing motion was happened with a constant amplitude because of the damping effect during wall collision was counteracted by extra energy induced by shape oscillation for  $Re = 220$ -1000. Figueroa-Espinoza [22] reported the zigzag motion of bubble within a channel in presence of two walls on both side for  $Re > 70$  while the oscillation of motion increases with increasing  $Re$ . For  $70 < Re < 100$ , bubble didn't touch either of the wall but for larger  $Re$ , repeated collisions ensued. Jeong and Park [23] reported after experiments at high  $Re$  that the period of lateral oscillation of bubble is dependent on initial bubble-wall separation and the change in wake structure because of the wall interaction. They speculated that the source of deformable bubble maintaining its relatively constant kinematics was the excess surface energy across the bubble-wall collision.

Zhang et al. [24] simulated bubbles at presence of a vertical wall at three different regimes (viz. steady, planar zigzag, spiral) and investigated the spiral regime in detail. They reported the decreasing trend of amplitude and frequency of oscillatory bubble motion with decreasing Galilei number while other three dimensionless parameters (viz. density ratio, viscosity ratio, Eötvös number) were constant to certain values. They also noted that the initial distance indeed had an effect on lateral migration of bubble from wall as found by previous researchers but the wall normal dimensionless force, amplitude and frequency converged to similar magnitude even though the wall-bubble initial distance was different. They argued that wall serves as a destabilizing factor for the wake structure behind bubble in the wall-normal direction but a stabilizing factor in the spanwise direction. They specified a critical Galilei number for which the complete transition from steady to oscillating regime happened and it was found to be less than that of unbounded condition suggesting the destabilizing factor that can be attributed to the presence of wall to the phenomenon of path instability.

# CHAPTER 3

## COMPUTATIONAL METHOD

### 3.1 Basics of CFD

The field of fluid dynamics deals with the flow of liquids and gases. To solve a definite fluid dynamics problem, various desired properties of the flow such as, velocity, pressure, temperature etc. have to be obtained. Initial experimental researches were instrumental to formulate empirical or semi-empirical laws that would later govern fluid flows. These laws panned out to be vital at solving wide range of complex fluid dynamics problems. Computational fluid dynamics constitutes a new third approach in the philosophical study and development of the whole discipline of fluid dynamics. The advent of the high-speed digital computer combined with the development of accurate numerical algorithms for solving physical problems on these computers have revolutionized the way we practice fluid dynamics today. Computational fluid dynamics is today an equal partner with pure theory and pure experiment in the analysis and solution of fluid dynamics problems. Since, the field of fluid dynamics is built onto conservation laws, the governing equations for a fluid can be presented as conservation of mass and conservation of momentum equation.

Conservation of mass equation:

$$\frac{\partial \rho}{\partial t} + \nabla \cdot (\rho \mathbf{u}) = 0 \quad (3.1.1)$$

Conservation of momentum equation:

$$\frac{\partial(\rho \mathbf{u})}{\partial t} + \mathbf{u} \cdot \nabla(\rho \mathbf{u}) = -\nabla p + \nabla \tau_{ij} + \rho \mathbf{g} \quad (3.1.2)$$

These equations along with the conservation of energy equation form a set of coupled, non-linear partial differential equations. It is not possible to solve these equations analytically for most engineering problems. However, it is possible to obtain approximate computer-based solutions to the governing equations for a variety of engineering problems. This is the subject matter of Computational Fluid Dynamics.

### 3.2 Applications of CFD

CFD can be useful for wide range of applications and some of the instances are given below:

- i. CFD can be used to simulate problems related to external aerodynamics such as, flow over a vehicle, interaction of propellers or rotors with the aircraft fuselage etc.
- ii. CFD can be used to simulate internal flow dynamics such as, gas flow through gas-pipeline, bubbly flow through a column etc.
- iii. CFD is being used increasingly in the study of circulatory and respiratory systems and contributing to the growth of Bio-medical engineering.
- iv. CFD is useful for the study of dynamics of ocean waves as part of disaster management studies (e.g. damage caused by tsunami).
- v. CFD can be used to predict future weather condition based on current weather condition.

CFD is attractive to industry since it is more cost-effective than physical testing. However, one must note that complex flow simulations are challenging and error-prone and it takes a lot of engineering expertise to obtain validated solutions.

### 3.3 Strategy of CFD

Basic steps involved with CFD:

- i. Geometry or domain of a specific problem is defined.
- ii. Discretization of the domain occupied by fluid to finite discrete volumes. This is called meshing. It can be uniform, non-uniform, adaptive (changes as the simulation progresses).
- iii. Mathematical modeling i.e. governing equation(s), boundary conditions, initial conditions (transient problems).
- iv. Choosing a numerical solver for solving the governing equation(s) using boundary conditions or initial conditions or both.
- v. Starting the simulation and iterative solution till a steady-state is reached or advancing of time for unsteady solution of transient problems.
- vi. Post-processing to visualize and analyze the solution.

#### 3.3.1 Discretization

The strategy of CFD is to replace the continuous problem domain with a discrete domain using a grid. In the continuous domain, each flow variable is defined at every point in the domain. For instance, the pressure  $u$  in the continuous 2D domain shown in the figure below would be given as,

$$u = u(x, y); 0 < x < 1, 0 < y < 1 \quad (3.3.1.1)$$

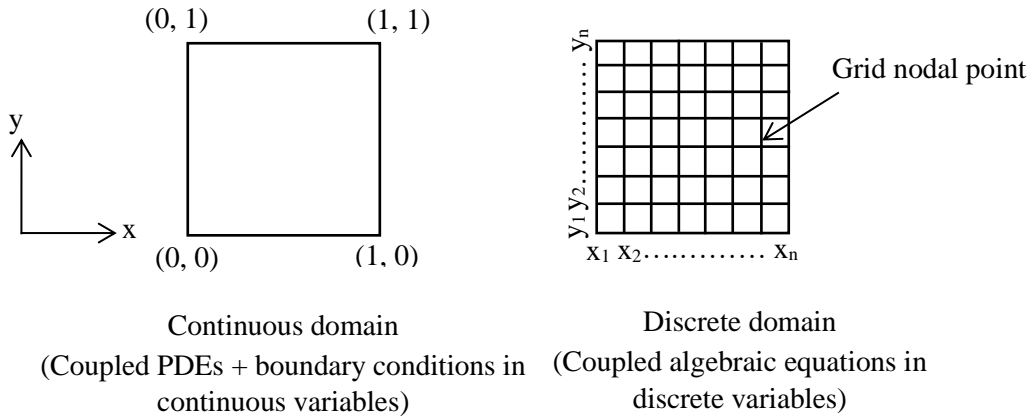


Figure 3.1: Typical discretization of domain in CFD

In the discrete domain, each flow variable is defined only at the grid nodal points. So, in the discrete domain shown below, the pressure would be defined only at the N grid points.

$$u_i = u(x_i, y_i); i = 1, 2, 3, \dots, n \quad (3.3.1.2)$$

In a CFD solution, one would directly solve for the relevant flow variables only at the nodal points. The values at other locations are determined by interpolating the values at the grid points. The governing partial differential equations and boundary conditions are defined in terms of the continuous variables

such as  $p$ ,  $u$  etc. One can approximate these in the discrete domain in terms of the discrete variables  $p_i$ ,  $u_i$  etc. The discrete system is a large set of coupled algebraic equations in the discrete variables. Setting up the discrete system and solving it involves a very large number of repetitive calculations. This method of deriving the discrete equation using Taylor's series expansions is called the finite difference method. However, most commercial CFD codes use the finite-volume or finite-element methods which are better suited for Modeling flow past complex geometries.

## 3.4 Basilisk

Basilisk is the name of a free software program for the solution of partial differential equations on adaptive Cartesian meshes. It is the successor of Gerris and is developed by the same authors [34].

### 3.4.1 Grids

As stated earlier, computational schemes are started off by converting continuous fluid field variables to discrete fluid field variables. As a result, values of the field variables are obtained at discrete locations of the domain. This transformation, consequently, converts the partial differential equation(s) to a set of simultaneous algebraic equations. That is accomplished by dividing the original domain into number of discrete finite volume cells (referred to Figure 3.1). Those discrete finite volume cells are called grids/cells. Different types of grids that are available in Basilisk [35]:

- i. **Uniform Grid:** The grid spacing is uniform throughout the domain or the grid level (level of refinement) is constant throughout (Figure. 3.2a).
- ii. **Non-Uniform Grid:** The grid spacing is not the same throughout the domain. There are parts of the domain where level of refinement is high, and there are parts where level of refinement is low (Figure 3.2b).
- iii. **Adaptive Grid:** Quite a large number of flows showcase differing behaviors in different parts of it flow region. There can be places in domain where the flow field varies significantly either spatially or temporally or both. And there can be places where flow field doesn't vary much spatially or temporally, hence rendering the flow field sort of unchanged and uninteresting. Such behaviors can be observed in flows with vorticity generating boundary layers, intermittent turbulent flows etc. So, developing a grid structure became important in evaluating a constantly changing and evolving fluid flow. The AMR approach by Berger and Colella (1989) [36] and The Quad/Octree approach by Coirier (1994) [37], Howell and Bell (1997) [38], Khokhlov (1998) [39] played vital roles in developing the adaptive grid structure. While the AMR framework uses standard discretization algorithms on a hierarchy of regular Cartesian grids which interact with each other through boundary conditions, the Quad/Octree schemes, adapt the discretization operators in a way that they may be usable at coarse/fine cell boundaries (Figure 3.2c).

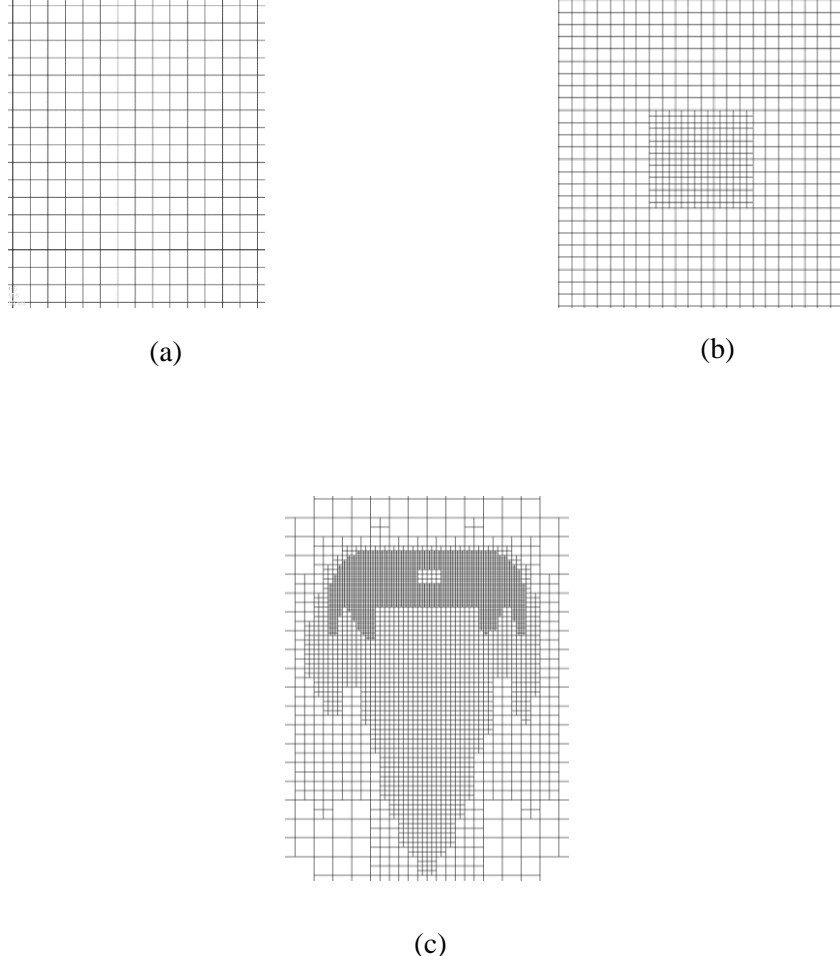


Figure 3.2: (a) sample uniform grid (b) sample non-uniform grid [Higher-order adaptive methods for fluid dynamics] (c) sample adaptive grid.

Basilisk employs grid-level (level of refinement) to identify each finite volume cell. The implementation of such technique is facilitated by multigrid (multiple resolution grid) or tree-grid (bitrees for 1D, quadtrees for 2D, octrees for 3D).

Multigrid has more than one spatial resolution. A multi-resolution grid forms when one or more “levels of refinement” are added. For a multigrid with “L” levels of refinement, the grid consists of  $2^L \times 2^L$  cells at the maximum resolution [40]. The size of the cell is formulated by,  $\Delta = 1/2^L$  where “L” is the grid-level (maximum level of refinement). Successive spatial refinement is achieved by starting from the coarsest grid level (level = 0, no. of cells = 1) to maximum finest grid level (level = N, no. of cells =  $2^N$ ).

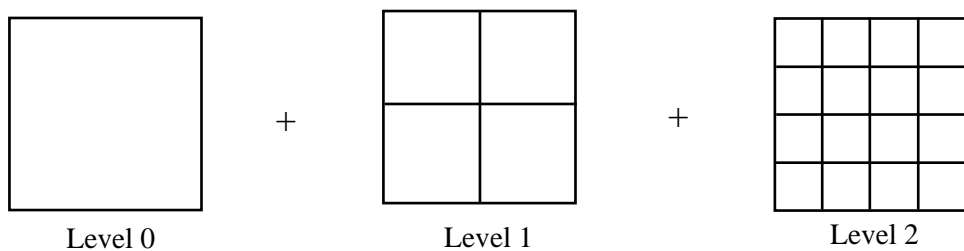


Figure 3.3: Multigrid structure (combination of different levels of refinement)

While multigrid doesn't have variable spatial resolution, tree-grid provides just that. All cells illustrated at Figure 3.4 of "Level 2" can be attributed to one of the four cells of "Level 1". The four cells that exist on a higher level are called the 'children' of the cell at the lower level. Therefore, the low-level cell is a 'parent'. The parent cell in this example is also a child, its parent is the root cell. An obvious way of introducing a varying spatial resolution is to not initialize the children of some parents at a given level [40].

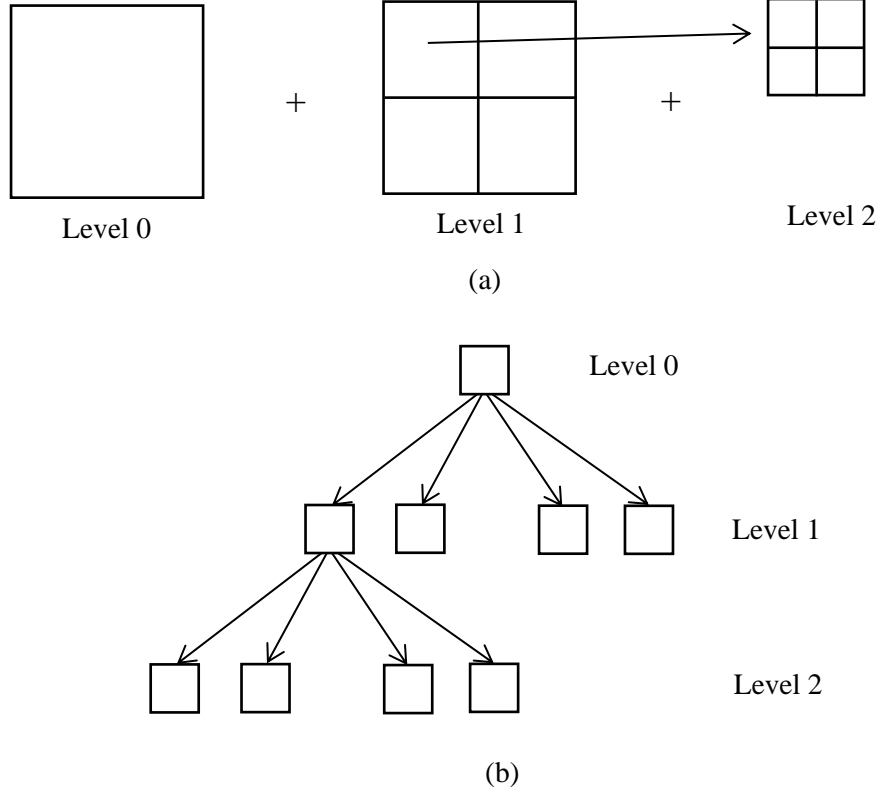


Figure 3.4: (a) Cell arrangement in Tree-grid structure (Quadtree) (b) Equivalent quadtree structure

Multigrid implementation is used for uniform grid and Tree-based structure is used for no-uniform or adaptive grid in Basilisk. For tree-based structure, quadtree is implemented in 2D simulations while octree is used predominantly in 3D simulations. Hence, octree is 3D equivalent of quadtree.

### 3.4.2 Tree-based Grid Adaptivity

Since the tree-based grid structures prove to be advantageous for refinement and coarsening of the mesh that varies in resolution and evolves over the timespan of the simulation, a decision algorithm is required for general implementation to facilitate such adaptivity known as AMR (Adaptive Mesh Refinement) [41]. A wavelet-based strategy is adopted to act as the adaptation algorithm.

The adaptive wavelet algorithm is based around the estimation of spatial discretization error on the flow field. The specific designated function (`adapt_wavelet()`) requires the user to define a list of fields that it will analyze for the refinement or coarsening. This list can consist of any combination of the existing scalar fields. In general, it makes sense to use the fields that appear in the equations that are being solved. Also, the adaptation criterion that is the maximum tolerated estimated discretization error for each field has to be defined. Finally, a maximum level (i.e., resolution) that the algorithm is allowed to employ should be provided. Error is evaluated to make decisions whether the grid cells need to be refined or coarsened. The cells can be too coarse, too fine or just fine. If the cells are estimated to be

too coarse, will be refined. Also, cells that need to be kept just at the resolution boundaries differing a single level are also refined. Too fine cells are coarsened only if all children of a parent cell are estimated as too fine and coarsening them won't violate the necessary requirements [40].

### 3.4.3 Fields and Stencils

*Field* constructs are used to store quantities discretized spatially. They can be seen as a generalization of C arrays. In Basilisk, there are three types of fields: scalar, vector and tensor. Scalar fields store scalars while Vector fields are a collection of D scalar fields (where D is the dimension of the spatial discretization) and tensor fields are a collection of D vector fields. Each of the components of the vector or tensor fields are accessed using the x, y or z field of the corresponding structure [42].

*Stencils* are used to access field values and their local neighbors. By default, Basilisk guarantees consistent field values in a 3x3 neighborhood (in 2D). This can be represented like shown below:

a [-1, 1]	a [0, 1]	a [1, 1]
a [-1, 0]	a [0, 0]	a [1, 0]
a [-1, -1]	a [0, -1]	a [1, -1]

Figure 3.5:  $3 \times 3$  stencils

### 3.4.4 Boundary Conditions

Boundary conditions are constraints that are added to CFD simulations to solve the converted set of simultaneous algebraic equations. Basilisk implements boundary conditions by adding cells outside of the domain boundary and the added cells are called ghost cells. The ghost cells' values are assigned in a manner that exact boundary constraints can be applied to boundary line. Simple Dirichlet, Neumann boundary conditions along with periodic and symmetry boundary conditions are the most prevalent in Basilisk.

*Symmetry* boundary condition is the default (that is when nothing is specified or prescribed) for any flow field. This boundary condition needs to maintain zero derivative of the flow field at the boundary line. For this, the ghost cells' values are assigned in such a way that symmetry is maintained across the boundary line. If we consider a boundary, a scalar field  $a$  and a vector field  $\mathbf{u}$ , *symmetry* boundary condition can be expressed on the boundary as [43]:

$$\partial_n \alpha = 0 \quad (3.4.4.1)$$

$$\partial_n \mathbf{u}_t = 0 \quad (3.4.4.2)$$

$$\mathbf{u}_n = 0 \quad (3.4.4.3)$$

where, n and t are the normal and tangential direction to the boundary respectively.

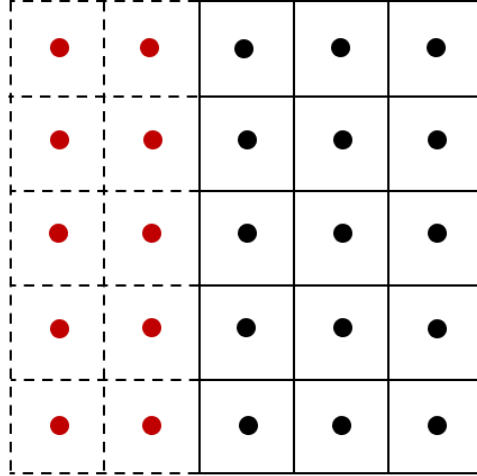


Figure 3.6: Ghost cells outside boundary with different values than inside cells

## 3.5 Formulation

### 3.5.1 Governing Equations

The dimensional governing equations for bubbly flow consist of mass and momentum conservation equations along with an advection equation for the volume fraction of the liquid phase.

The mass and momentum conservation equations are as follows respectively:

$$\nabla \cdot \mathbf{u} = 0 \quad (3.5.1.1)$$

$$\rho \left[ \frac{\partial \mathbf{u}}{\partial t} + \mathbf{u} \cdot \nabla \mathbf{u} \right] = -\nabla p + \nabla \cdot [\mu (\nabla \mathbf{u} + \nabla \mathbf{u}^T)] + \delta \sigma \kappa \mathbf{n} + \rho \mathbf{g} \quad (3.5.1.2)$$

The flow is assumed to be incompressible, Newtonian, laminar, isothermal, immiscible. Here,  $\mathbf{u}$  denotes the flow velocity field having three velocity components ( $u, v, w$ ) along three directions ( $x, y, z$ ),  $p$  is the pressure field,  $t$  is time,  $\mathbf{g}$  ( $= -g\mathbf{j}$ ) is the acceleration due to gravity where  $\mathbf{j}$  is the unit vector along the vertical direction,  $\sigma$  represents the interfacial tension (constant),  $\delta$  is the Dirac delta function that suggests that surface tension is concentrated on the interface,  $\kappa$  ( $= \nabla \cdot \mathbf{n}$ ) is the interfacial curvature,  $\mathbf{n}$  represents the outward unit normal vector to the interface.

The interface separating gas and liquid phases is obtained by approximating the solution of an advection equation given below:

$$\frac{\partial c}{\partial t} + \mathbf{u} \cdot \nabla c = 0 \quad (3.5.1.3)$$

where,  $c$  is the volume fraction of the principal phase ( $c = 0$  for air and  $c = 1$  for liquid for this instance).

The density,  $\rho$  is defined using arithmetic mean while the viscosity,  $\mu$  is defined using harmonic mean as harmonic mean of viscosity works better for higher density and viscosity ratios. The relations between density and viscosity are as follows:

$$\rho = c\rho_l + (1 - c)\rho_g \quad (3.5.1.4)$$

$$\frac{1}{\mu} = \frac{c}{\mu_l} + \frac{1-c}{\mu_g} \quad (3.5.1.5)$$

Scaling to render the governing equations dimensionless is as follows:

$$(x, y, z) = D(\bar{x}, \bar{y}, \bar{z})$$

$$t = \frac{d}{u} \bar{t}$$

$$\mathbf{u} = u \bar{\mathbf{u}}$$

$$\rho = \rho_l \bar{\rho} \quad (3.5.1.6)$$

$$\mu = \mu_l \bar{\mu}$$

$$\sigma = \frac{\bar{\sigma}}{d}$$

$$p = \rho_l u^2 \bar{p}$$

where,  $d$ ,  $u$  ( $= \sqrt{gd}$ ),  $t$  ( $= d/u$ ) are characteristic length, characteristic velocity and characteristic time respectively. Over-bar is designated to represent non-dimensional quantity. Dropping the over-bars, the governing equations in non-dimensional form stand out to be [19],

$$\nabla \cdot \mathbf{u} = 0 \quad (3.5.1.7)$$

$$\frac{\partial \mathbf{u}}{\partial t} + \mathbf{u} \cdot \nabla \mathbf{u} = -\nabla p + \frac{1}{Ga} \nabla \cdot [\mu (\nabla \mathbf{u} + \nabla \mathbf{u}^T)] + \delta \frac{\nabla \cdot \mathbf{n}}{Eo} \mathbf{n} - \rho \mathbf{j} \quad (3.5.1.8)$$

$$\frac{\partial c}{\partial t} + \mathbf{u} \cdot \nabla c = 0 \quad (3.5.1.9)$$

where,  $Ga$  ( $= \frac{\rho_l g^2 d^3}{\mu_l}$ ) is Galilei number

$Eo$  ( $= \frac{\rho_l g d^2}{\sigma}$ ) is Eötvös number.

And the non-dimensional density and dynamic viscosity are-

$$\rho = c + \frac{1-c}{\rho_r} \quad (3.5.1.10)$$

$$\frac{1}{\mu} = c + (1 - c)\mu_r \quad (3.5.1.11)$$

where,  $\rho_r (= \rho_l/\rho_g)$  and  $\mu_r (= \mu_l/\mu_g)$  are density ratio and dynamic viscosity ratio respectively.

### 3.5.2 Numerical Technique

Chorin [44] introduced an effective way of solving the Navier-Stokes equations numerically. The method known as *Projection Method* serves a key advantage in solving Navier-Stokes equations that is the computations of velocity and pressure fields are decoupled by using *Helmholtz Decomposition* which states that any vector field can be split into a divergence-free (solenoidal) part and an irrotational part. The algorithm which is executed in two stages, computes an intermediate velocity at each time step that does not satisfy the incompressibility constraint at the first stage. At the second stage, the pressure is used to project the intermediate velocity onto a space of divergence-free velocity field to get the next update of velocity and pressure.

First, the momentum equation can be split into two parts (by ignoring pressure gradient at first) for computing an intermediate velocity.

$$\frac{\mathbf{u}^* - \mathbf{u}^n}{\Delta t} = (-\mathbf{u}^n \cdot \nabla) \mathbf{u}^n + \vartheta \nabla^2 \mathbf{u}^n \quad (3.5.2.1)$$

where,  $\mathbf{u}^n$  is the velocity at  $n^{\text{th}}$  time-step.

At the second stage, known as *projection step*, final velocity is computed using the pressure gradient term, using equation 3.5.3.2.

$$\mathbf{u}^{n+1} = \mathbf{u}^* - \frac{\Delta t}{p} \nabla p^{n+1} \quad (3.5.2.2)$$

But the equation demands knowledge of the pressure gradient term at  $(n+1)^{\text{th}}$  time-step. This can be obtained by taking the divergence of equation 3.5.3.2 and applying the continuity condition on velocity  $\mathbf{u}^{n+1}$ .

$$\nabla \cdot \mathbf{u}^{n+1} = 0 \quad (3.5.2.3)$$

This gives Poisson equation in pressure.

$$\nabla^2 p^{n+1} = \frac{\rho}{\Delta t} \nabla \cdot \mathbf{u}^* \quad (3.5.2.4)$$

As a result,  $p^{n+1}$  can be obtained solving the Poisson equation and then, bac-substituted in equation 3.5.3.2 to get  $\mathbf{u}^{n+1}$ . The Poisson equation is solved by using octree-based multilevel solver [45].

Incompressible Navier-Stokes (centered) solver implements a generic time loop, a CFL-limited timestep, the Bell-Collela-Glaz advection scheme [46] and the implicit viscosity solver [47], Bell-Collela-Glaz advection scheme involves a 2<sup>nd</sup> order, unsplit, upwind method which is stable if certain CFL condition is satisfied. It is essentially a 2<sup>nd</sup> order projection method for solving Navier-Stokes equation improving the original projection algorithm provided by Chorin [44].

Steps to be executed for solving the full Navier-Stokes equation [35]:

1. A suitable timestep is computed based on velocity and grid spacing data that satisfies the CFL condition ( $CFL = 0.8$ ).
2. Intermediate advection velocity is computed using BCG algorithm.

$$\frac{u^{adv} - u^n}{\Delta t} = [(\mathbf{u} \cdot \nabla) \mathbf{u}]^{n+1} \quad (3.5.2.5)$$

3. The computed intermediate advection velocity at step-2 is corrected using the pressure gradient and source acceleration term from  $t = t^{n-1/2}$  so that the first iterate for the time-marching modified Crank–Nicholson scheme can be formed.
4. Corrected advection velocity is used to compute intermediate velocity  $u^*$  by implicit viscosity solver.

$$\frac{u^* - u^{adv}}{\Delta t} = \frac{1}{\rho} \nabla \cdot \mu(D^* + D^n) \quad (3.5.2.6)$$

where,  $D$  is deformation tensor.

5. Intermediate velocity  $u^*$  is corrected by omitting the pressure gradient and source acceleration terms' contributions from  $t = t^{n-1/2}$ .
6. BCG projection algorithm is used to compute pressure at  $(n+1/2)^{th}$  timestep by using *Poisson-Helmholtz* solver to solve the Poisson equation, similar to that of Chorin's. Then, it is used to compute cell-centered velocity  $u^{n+1}$ .
7.  $u^{n+1}$  is corrected taking into account the contribution of pressure gradient and source acceleration terms at  $t = t^{n+1/2}$ .
8. Finally,  $O(2)$  adaptive refinement is done to finish one cycle of time-marching.

The interface between the fluids is tracked with a Volume-Of-Fluid method. The simplest way to implement a multi-dimensional VOF advection scheme is to use dimension-splitting that is advecting the field along each dimension successively using a one-dimensional scheme. The advection equation 3.5.2.9 of volume fraction is solved using a piece-wise linear geometrical VOF scheme [48].

For interface reconstruction, interface normal  $\mathbf{n}$  is computed and intercept  $a$  corresponds to the plane of the cell that represents the interface.

$$\mathbf{n} \cdot \mathbf{x} = a \quad (3.5.2.7)$$

Next, volume fraction flux is computed to advance the interface that must not violate the specified CFL condition. The consequential advection scheme results in sharp interfaces, which is close to second-order accurate for practical applications [49]. To mitigate the problem of spurious currents, height function method combined with balanced-force surface tension discretization scheme is used [41].

While applying the AMR technique, a tolerance is set to the velocity field and bubble surface ( $\varepsilon = 0.01$ ). This helps to enforce finer resolution to places of high velocity and near bubble interface while the smallest grid size is used for a certain maximum level.

### 3.5.3 Geometry

#### 3.5.3.1 Computational Domain

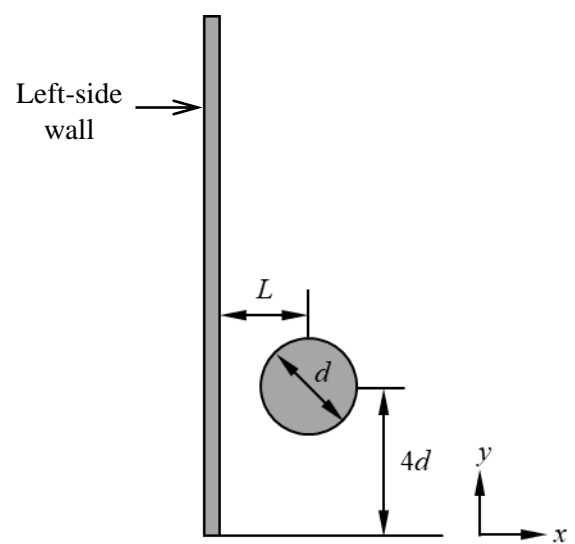
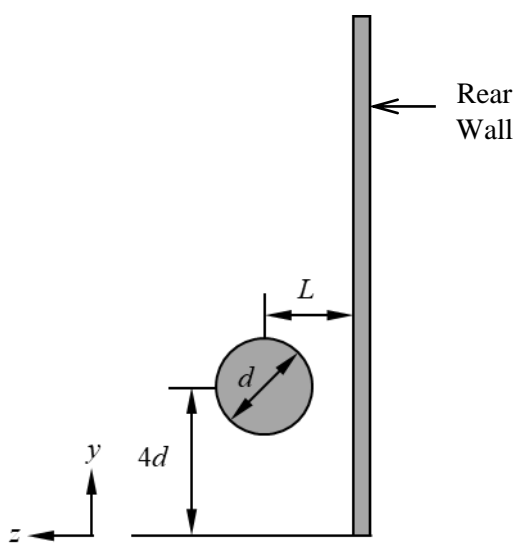
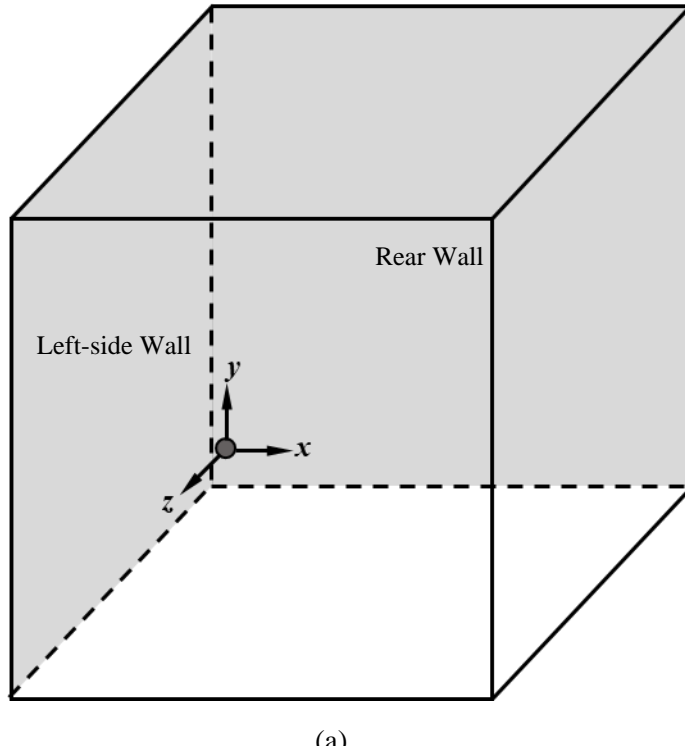


Figure 3.7: Schematic of computational domain (a) Isometric view ( $100d \times 100d \times 100d$ ) domain where  $d$  is bubble diameter) (b) Right-side view (c) Front view of the domain. Initial distance of bubble from both rear and left-side wall is  $L$  ( $= 0.75d$ ). The bubble is kept at  $4d$  distance initially as well from the bottom wall so that the bottom wall has no effect on the dynamics. It is to be noted that bubble size is exaggerated for better visibility since the actual bubble size is way too small compared to domain.

### 3.5.3.2 Parameters Definition

The problem of rising bubble can be characterized by four dimensionless numbers [25, 19, 17]. They are- density ratio  $\rho_r$ , viscosity ratio  $\mu_r$ , Eötvös number  $Eo$  and Galilei number  $Ga$ .

Density ratio is the ratio of liquid phase density to gas phase density. It is given by,

$$\rho_r = \rho_l / \rho_g \quad (3.5.3.2.1)$$

Viscosity ratio is the ratio of liquid phase dynamic viscosity to gas phase dynamic viscosity. It is given by,

$$\mu_r = \mu_l / \mu_g \quad (3.5.3.2.2)$$

Eötvös number is the ratio of gravitational force to surface tension force. It is given by,

$$Eo = \rho_l g d^2 / \sigma \quad (3.5.3.2.3)$$

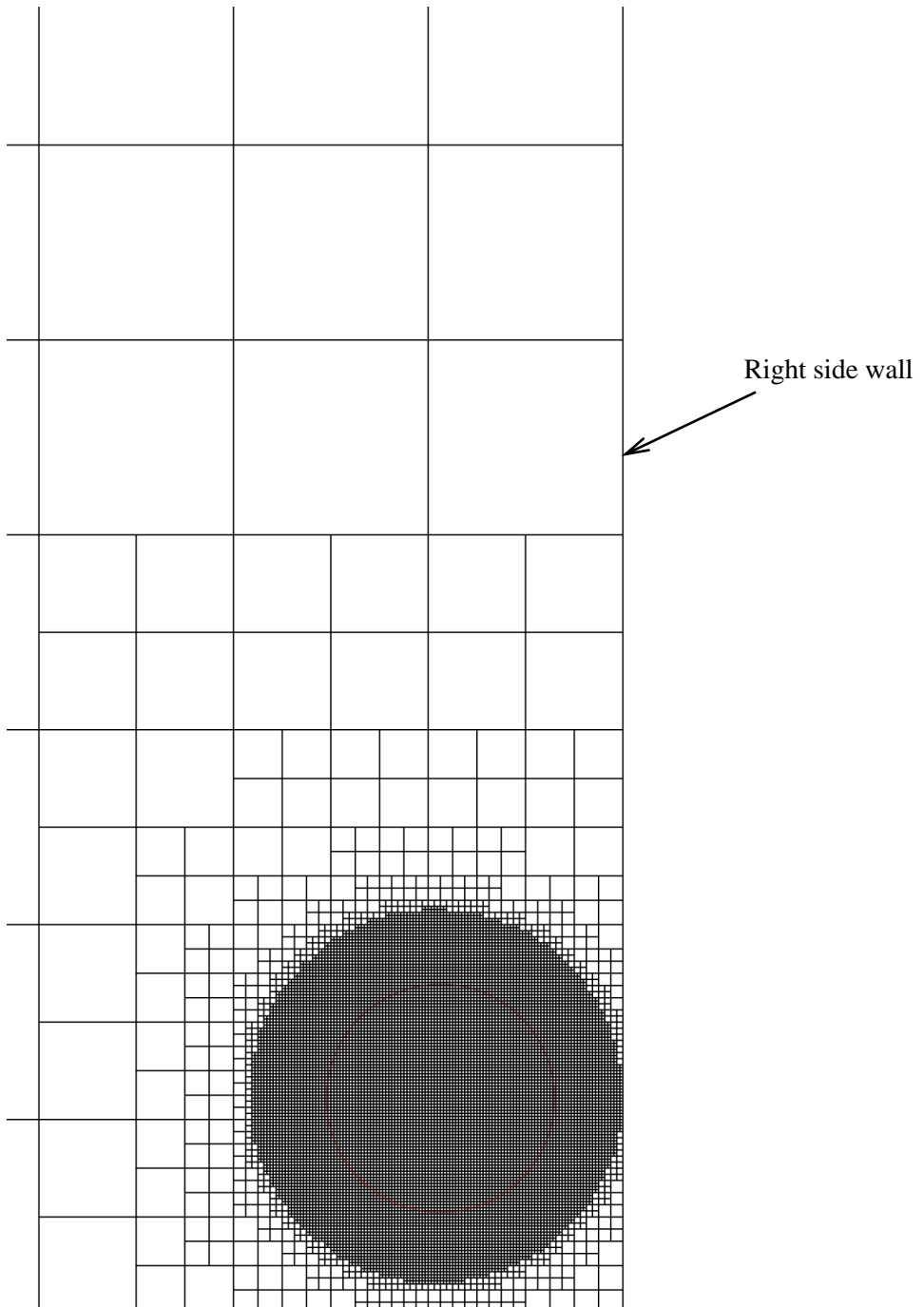
Galilei number is the ratio of gravitational force to viscous force. It is given by,

$$Ga = \rho_l g^{1/2} d^{3/2} / \mu_l \quad (3.5.3.2.4)$$

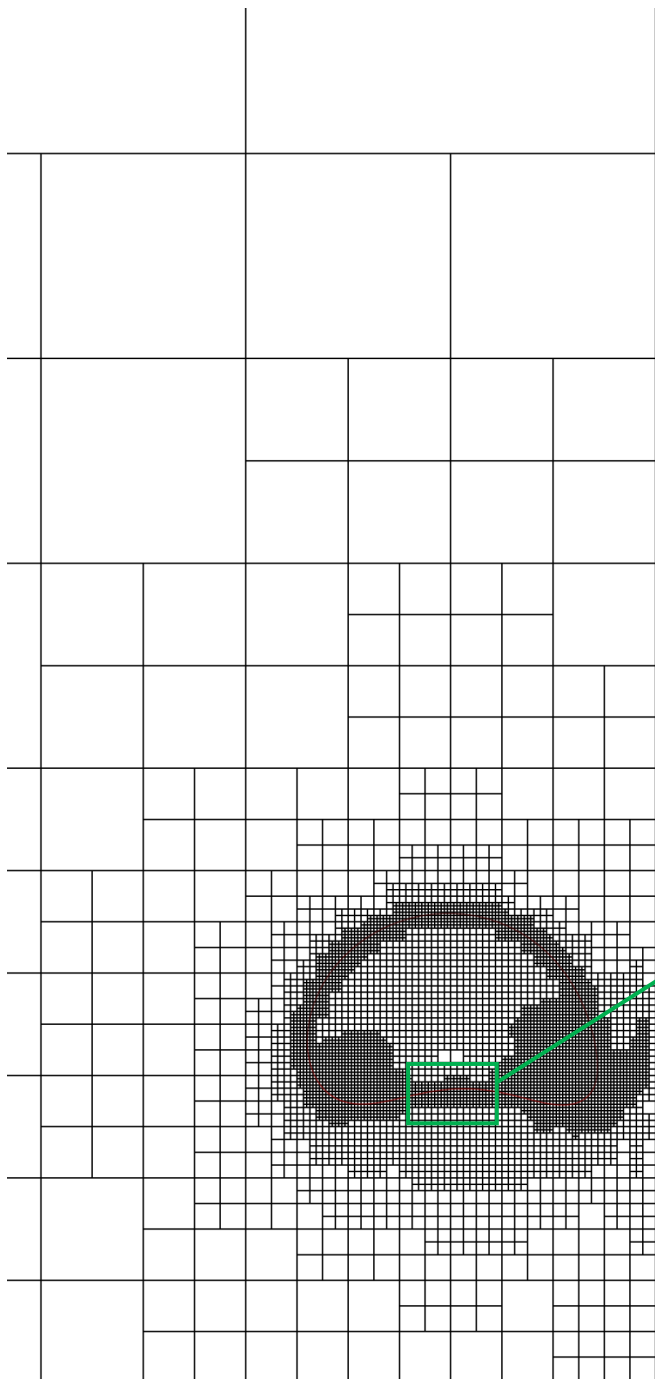
Eötvös number, also known as Bond number, is a variant of Weber number ( $We = \rho_l u^2 d / \sigma$ ) while Galilei number is a variant of Reynolds number ( $Re = \rho_l u d / \mu_l$ ) with the velocity scale being  $\sqrt{gd}$ . Weber number and Reynolds number include terminal rising velocity  $u$  that isn't known *priori*. Hence, Eötvös number and Galilei number are preferable to describe the dynamics of rising bubble as all properties are known *a priori*. In our study, fixed density ratio and viscosity ratio along with fixed Eötvös number ( $Eo = 16$ ) are taken at  $\rho_r = 1000$  and  $\mu_r = 100$  respectively. Since only Galilei number ( $Ga = 40, 55, 57, 60, 61, 62, 63.36, 70, 90.51$ ) is varied, Morton number ( $Mo = Eo^3/Ga^4 = g\mu_l^4/\rho_l\sigma^3$ ) number would be different for each case. As is known, Morton number is constant for a given liquid-gas system [19], we have to use different liquid-gas system for each case. So, the properties corresponding to Eötvös number and Galilei number will also change from one liquid-gas system to another.

Various combination of liquid and gas (which is air in our study) systems can be practically used to carry out the study. Ideally, water-air system is the most common example of it. Other liquid apart from water can be used [19], that has density close to water and if the viscosity ratio is considerably small, the dynamics becomes insensitive to it [50, 51].

### 3.5.3.3 Mesh

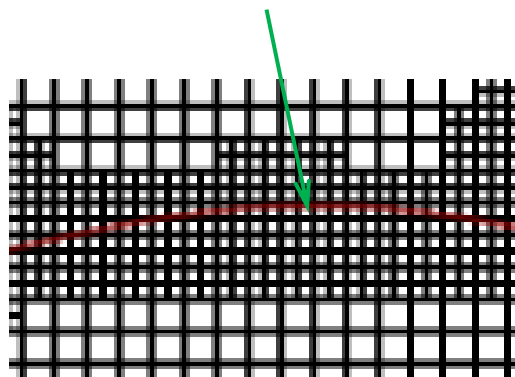


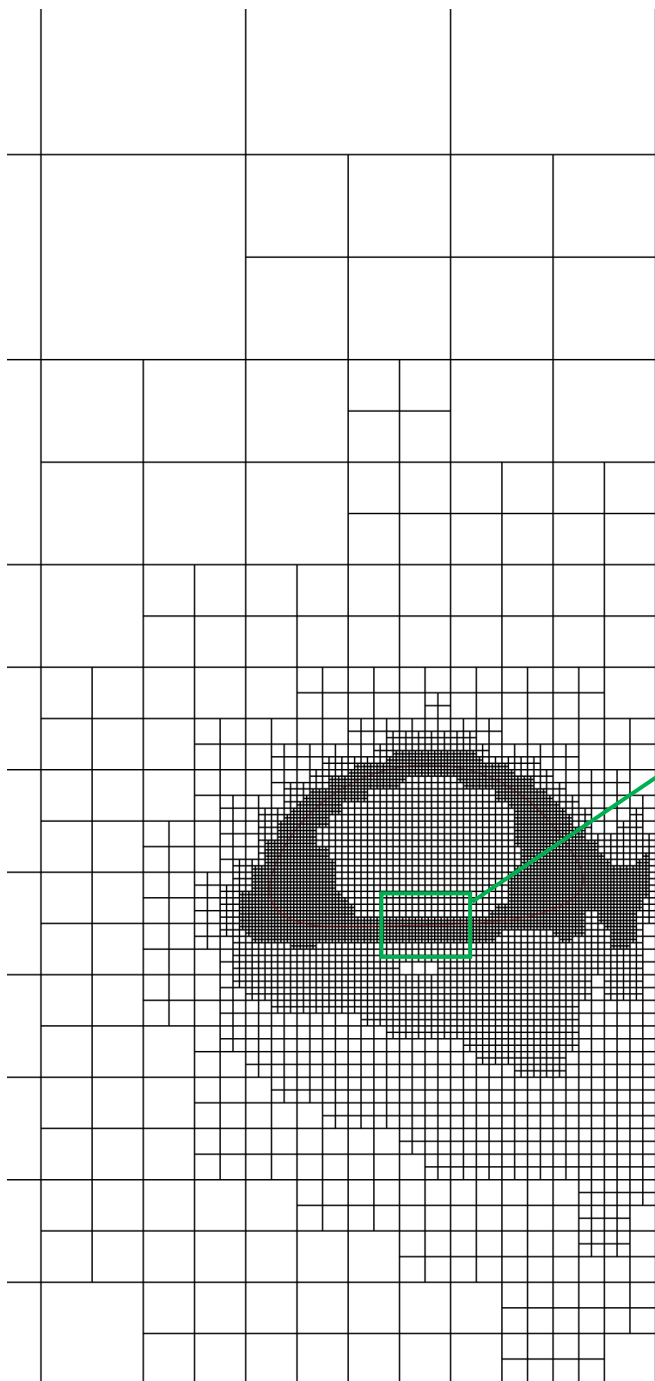
$t = 0$



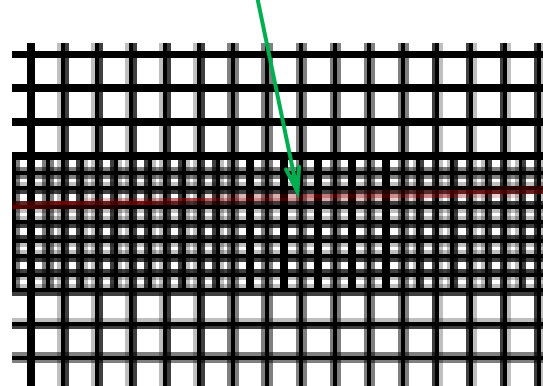
$t = 1$

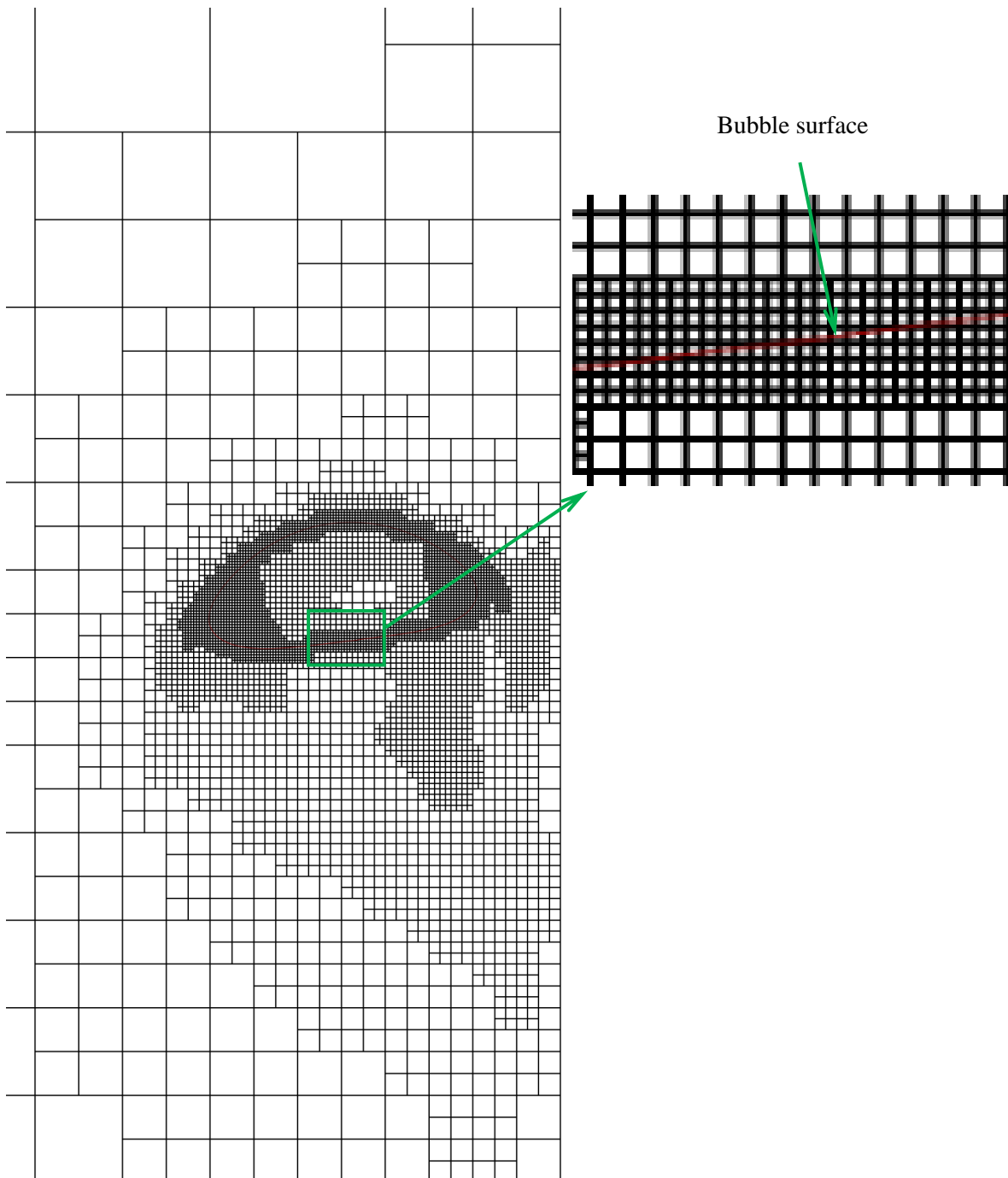
Bubble surface



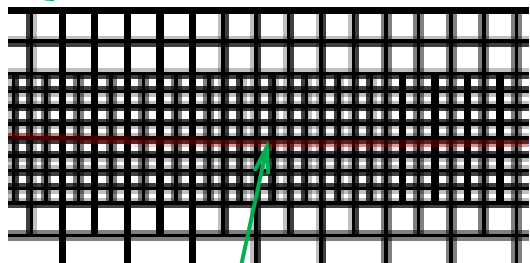
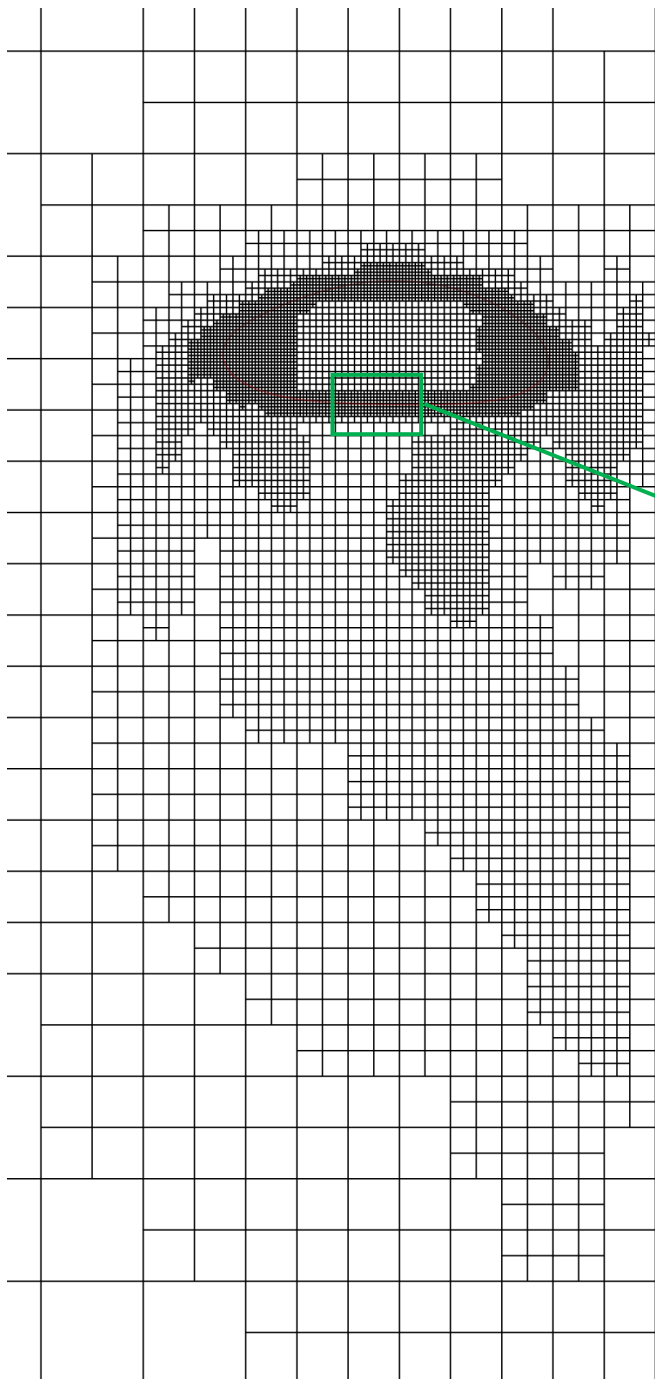


$t = 2$





$t = 3$



$t = 5$

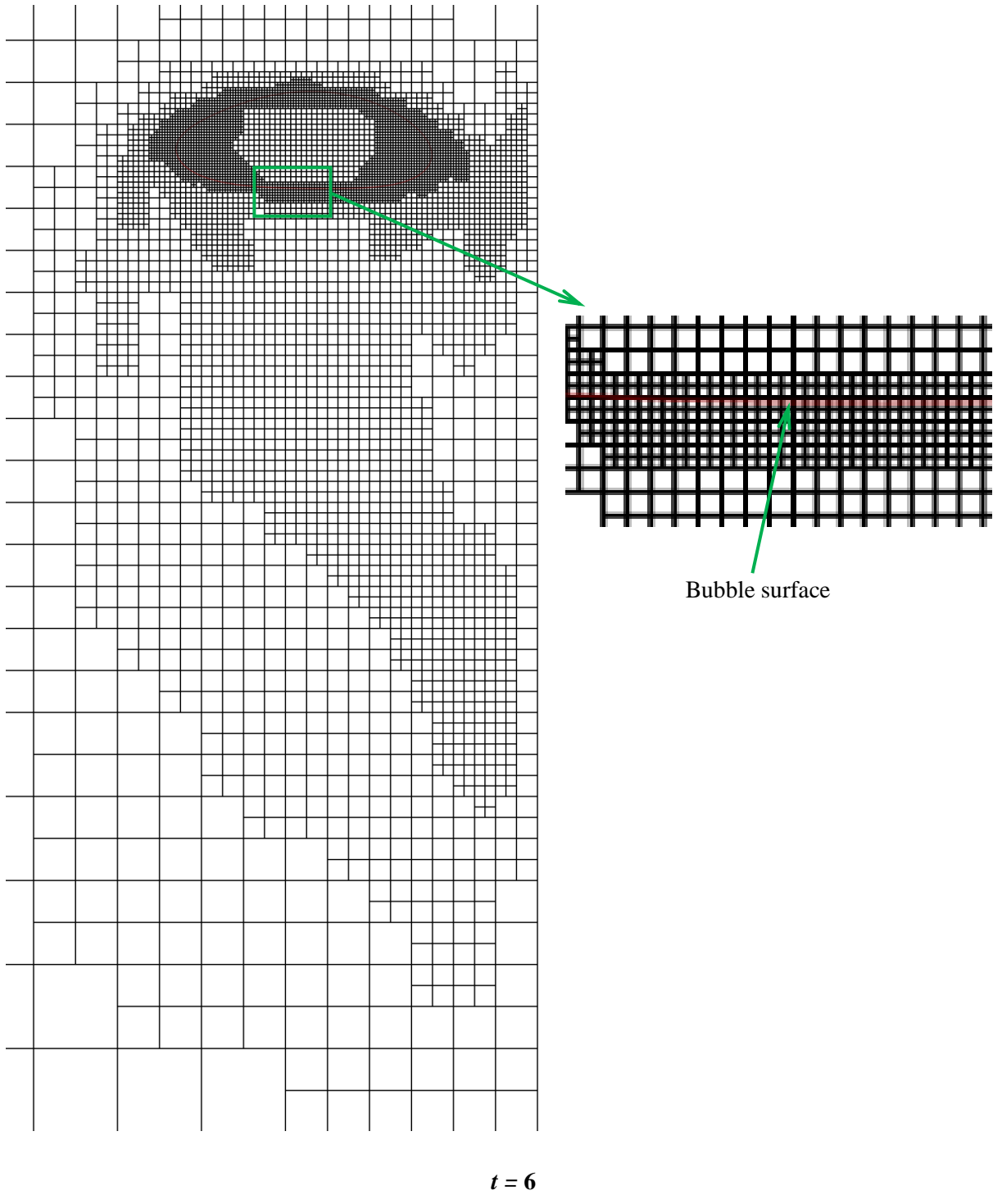


Figure 3.8: Spatio-temporal evolution of grid in and around bubble at  $t = 0, 1, 2, 3, 5, 6$  for case-7 ( $Ga = 63.36, Eo = 16, \rho_r = 1000, \mu_r = 100$ ). Red solid line represents bubble surface.

### 3.5.3.4 Boundary Conditions

*No slip and no penetration* condition are implemented on the *front, back, left, right* and *bottom* walls. That is to say, all components of velocity field  $\mathbf{u}$  are set to zero (simple Dirichlet conditions).

$$\begin{aligned}\mathbf{u}_t &= 0 \\ \mathbf{u}_r &= 0 \\ \mathbf{u}_n &= 0\end{aligned}\tag{3.5.3.4.1}$$

Where,  $t$  and  $r$  refer to two tangential components of velocity field on each wall and  $n$  refers to the normal component of velocity field on each wall.

*Symmetry* boundary condition is applied on the *top* wall. That is to set the normal derivative of tangential component of velocity field to *zero* (simple Neumann condition) and the normal component of velocity field to *zero* (simple Dirichlet condition) that has already been enforced in equation 3.5.3.4.1.

$$\partial_n \mathbf{u}_t = 0\tag{3.5.3.4.2}$$

## 3.6 Validation

### 3.6.1 Grid Independency Test

To seek out independency of result, a test against discretization error is performed by using different maximum level of refinement i.e. grid size. With the maximum level of refinement being higher, the smallest grid size becomes increasingly smaller. Two maximum level of refinement (*level* = 12 and 13) are used to compare the results such as, mesh density, bubble shapes, amplitude of oscillation in trajectory, time histories etc. Computational domain of  $100d \times 100d \times 100d$  is used for unbounded condition and the parameters are defined as,  $Ga = 90.51$ ,  $Eo = 16$ ,  $\rho_r = 1000$ ,  $\mu_r = 100$ .

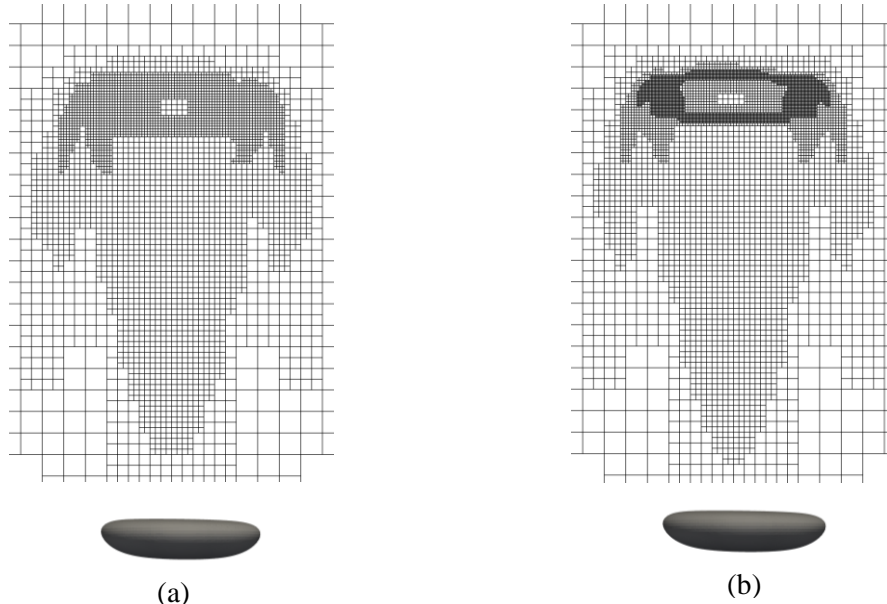


Figure 3.9: Grid dependency test for two different maximum level of refinement (a) *level* 12 (b) *level* 13 at  $t = 9$ . For *level* 12, smallest grid size is  $\Delta x = \Delta y = 0.0244$  and for *level* 13, smallest grid size is  $\Delta x = \Delta y = 0.0122$ . Two refinement criteria implemented are velocity field and bubble surface.



Figure 3.10: Effect on bubble shapes for two different maximum level of refinement at  $t = 9$ . Green and red solid lines correspond to bubble surface for *level 12* and *level 13* respectively.

Table 3.1: Comparison between two different maximum levels of refinement

Maximum level of refinement	Courant Number	$A_x$	$\delta_A$	$f_x$	$\delta_f$
12	0.8	0.396	-	0.116	-
13	0.8	0.380	4.04%	0.113	2.58%

Amplitude and frequency of bubble oscillation in  $x$ - direction are measured at two maximum different level of refinement. The difference in amplitude is 4.04%, while the difference in frequency is 2.58% when the maximum level is set from *level 12* to *level 13*. So, *level 13* that is finer grid converges to a more accurate result and the difference between the two levels are treated to be significant.

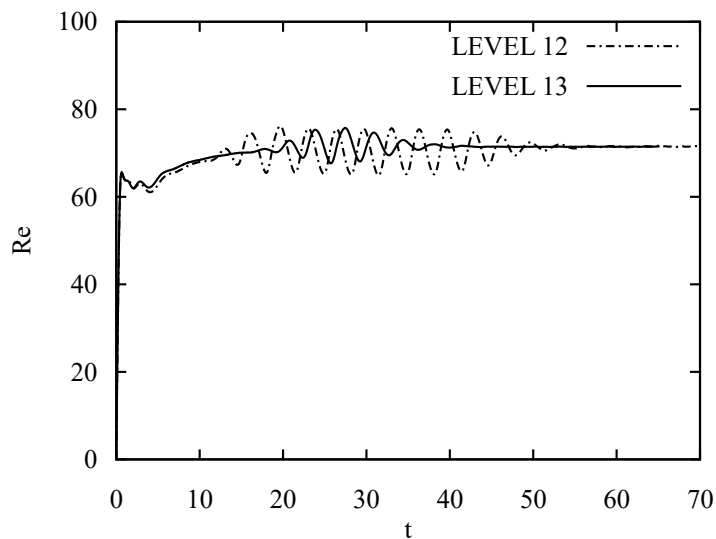


Figure 3.11: Time histories of Reynolds number for two different refinement level. It further shows that coarser grid induces instability earlier and persists longer than finer grid though the terminal Reynolds number converges to a certain magnitude.

So, maximum level of refinement *level 13* is deemed as the grid-convergent and used throughout our study.

### 3.6.2 Unbounded Condition

#### 3.6.2.1 Comparison with Experimental Results

Terminal Reynolds number ( $Re_{numerical}$ ) and bubble shape obtained from our simulation was compared against the experimental Reynolds number ( $Re_{exp}$ ) and bubble shapes obtained by Bhaga and Weber [8] for various cases. The results show good agreement with each other.

Table 3.2: Cases validated

Case No.	$Eo$	$Mo$	$Re_{exp}$	$Re_{numerical}$
1	116	5.51	13.3	13.46
2	339	43.1	18.3	18.7
3	116	0.103	42.2	42.4
4	115	$4.63 \times 10^{-3}$	94.0	101.35

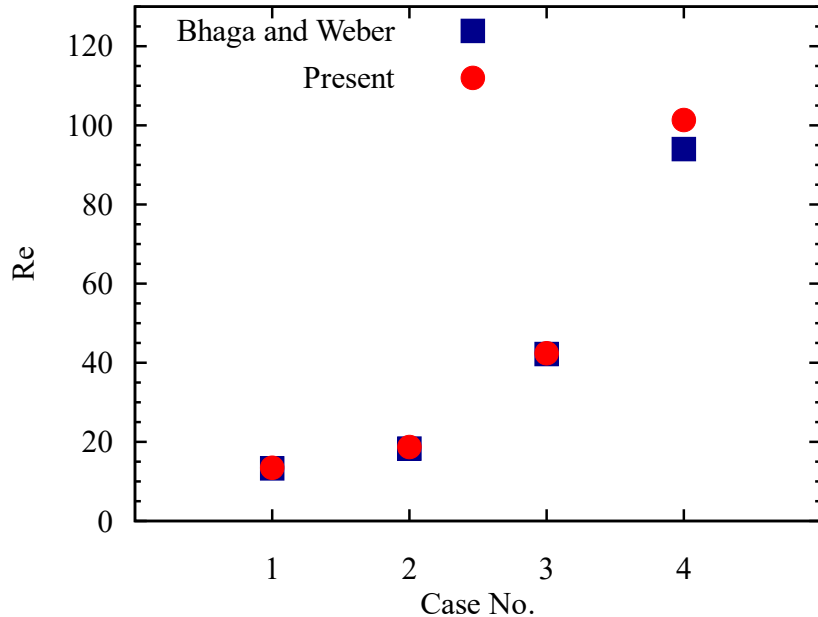


Figure 3.12: Comparison between terminal Reynolds number obtained from Bhaga and Weber [8] and present simulation.

As can be seen, the terminal Reynolds numbers are well in agreement with that of Bhaga and Weber [8]. For case no. 4 only, there seems to be slight deviation from as found by Bhaga and Weber [8] which is reasonable given the two different methods of research.

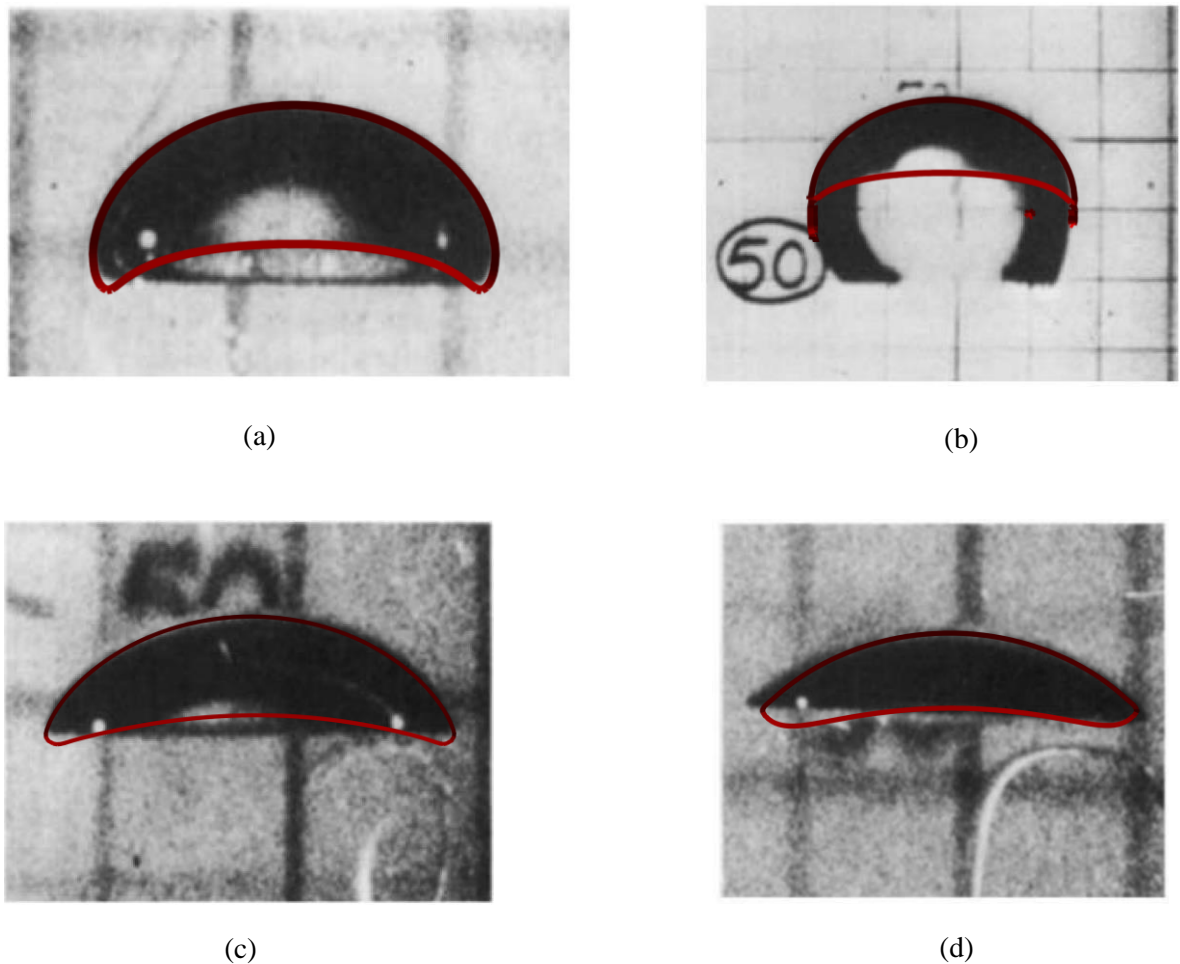


Figure 3.13: Comparison of terminal bubble shape from present simulation to Bhaga and Weber [8] (a)  $Eo = 116, Mo = 5.51$  (b)  $Eo = 339, Mo = 43.1$  (c)  $Eo = 116, Mo = 0.103$  (d)  $Eo = 115, Mo = 4.63 \times 10^{-3}$ . Red solid lines correspond to bubble shapes from present simulation.

Figure 3.13a and 3.13c takes up the terminal shape of oblate ellipsoidal cap while Figure 3.22b and 3.13d take the skirted shape and spherical cap shape respectively [8]. We can see that the terminal shapes from present simulation don't perfectly agree with the shapes obtained by Bhaga and Weber [8] as can be seen the side edges don't coincide with each other. But the defined shapes are observed to be the same. Red solid lines from Figure 3.13a and 3.13c indeed take up the oblate ellipsoidal cap shape. Skirt as found from second case (red line of Figure 3.13b) doesn't extend much while Bhaga and Weber [8] found the skirt to be relatively long. Figure 3.13d shows the deviation of present shape from as found by Bhaga and Weber towards left edge as they perfectly don't coincide with one another. But the terminal shapes for both do resemble the spherical cap type.

### 3.6.2.2 Comparison with Numerical Simulation

The simulation results of Zhang et al. [24] were reproduced in order to validate our code based on code by Popinet [52]. The computational domain as well as the parameters is taken as the same as them. The results are reproduced for two cases- *unbounded* and *with a vertical wall* for the same parameters. The maximum level of refinement used for both cases is 13 ( $\Delta x = \Delta y = 0.0122$  for smallest grid). Here, the validation for unbounded condition is shown.

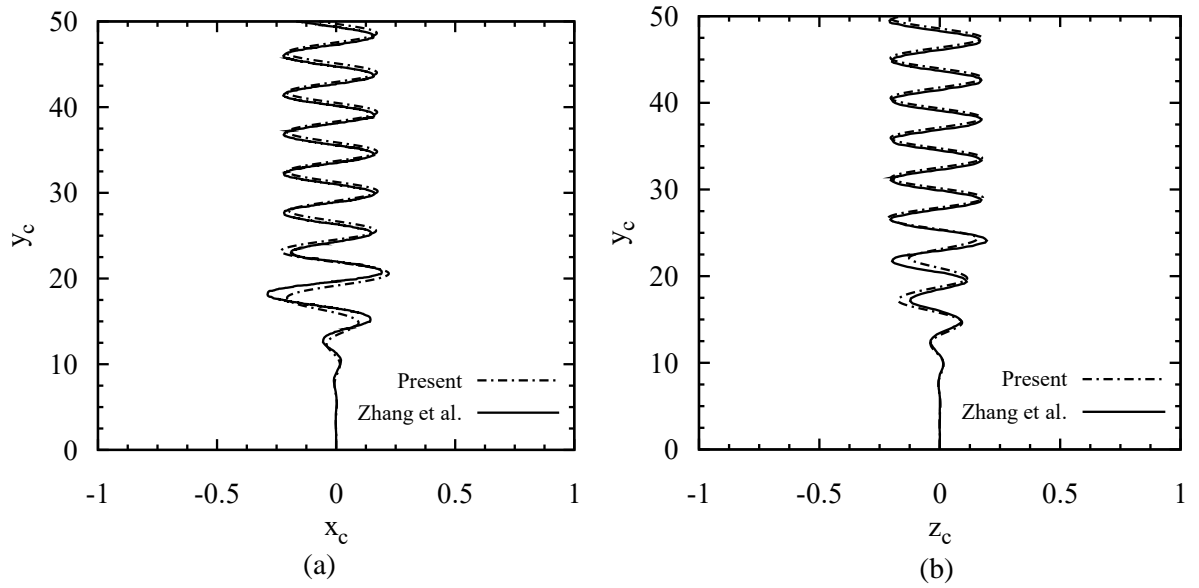


Figure 3.14: (a) Variation of  $x_c$  along vertical path  $y_c$  (front view of bubble trajectory) (b) Variation of  $z_c$  along vertical path  $y_c$  (right side view of bubble trajectory).

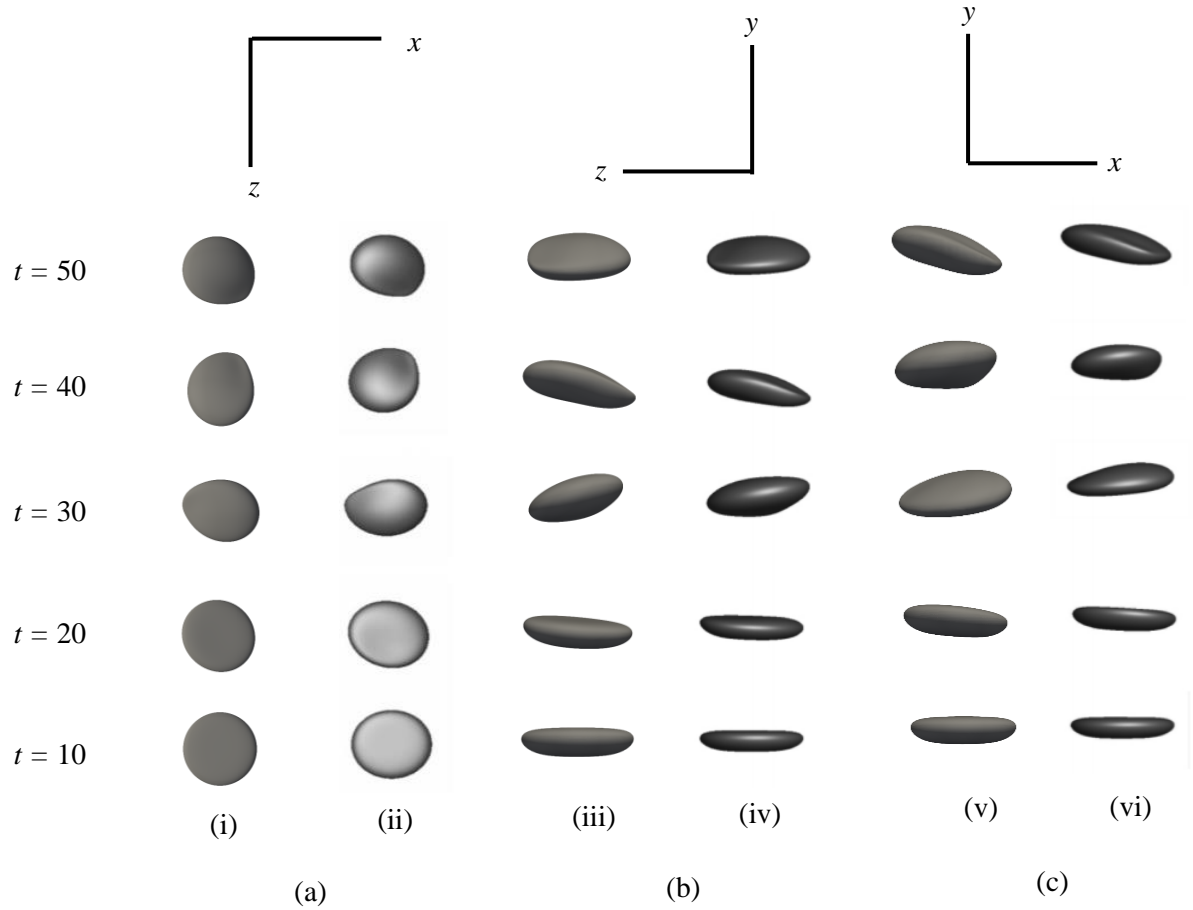


Figure 3.15: Spatio-temporal variation of bubble shapes (a) top view (b) right side view (c) front view at  $t = 10, 20, 30, 40, 50$ . (i), (iii) and (v) correspond to present results and (ii), (iv) and (vi) correspond to results from Zhang et al. [24].

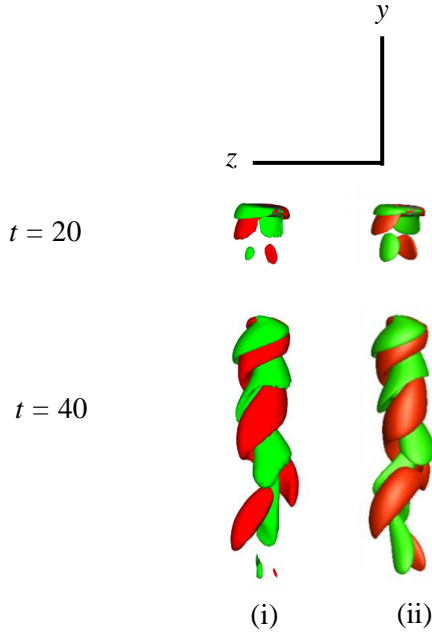


Figure 3.16: Iso-contours of the streamwise vorticity  $\omega_y = \pm 0.15$  at  $t = 20, 40$  from (i) present simulation (ii) Zhang et al. [24].

### 3.6.3 With Vertical Wall

The validation for bubble near a vertical wall is shown below.

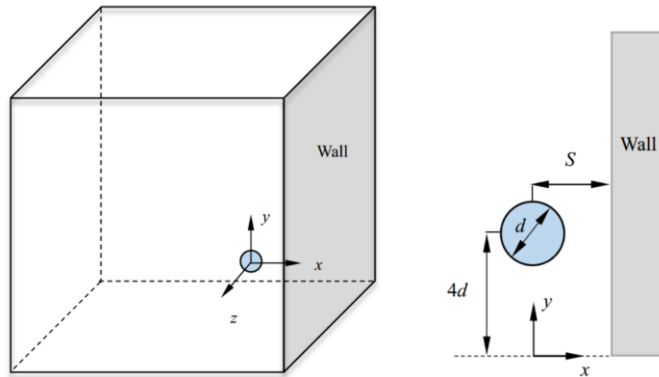


Figure 3.17: Schematic of the computational domain as illustrated in Zhang et al. [24], where domain is  $100d \times 100d \times 100d$ , distance from wall in x- direction  $S = 0.75d$ , distance from bottom wall in y- direction is  $4d$ , and the parameters are taken as  $Ga = 90.51$ ,  $Eo = 16$ ,  $\rho_r = 1000$ ,  $\mu_r = 100$  for both unbounded and wall conditions.

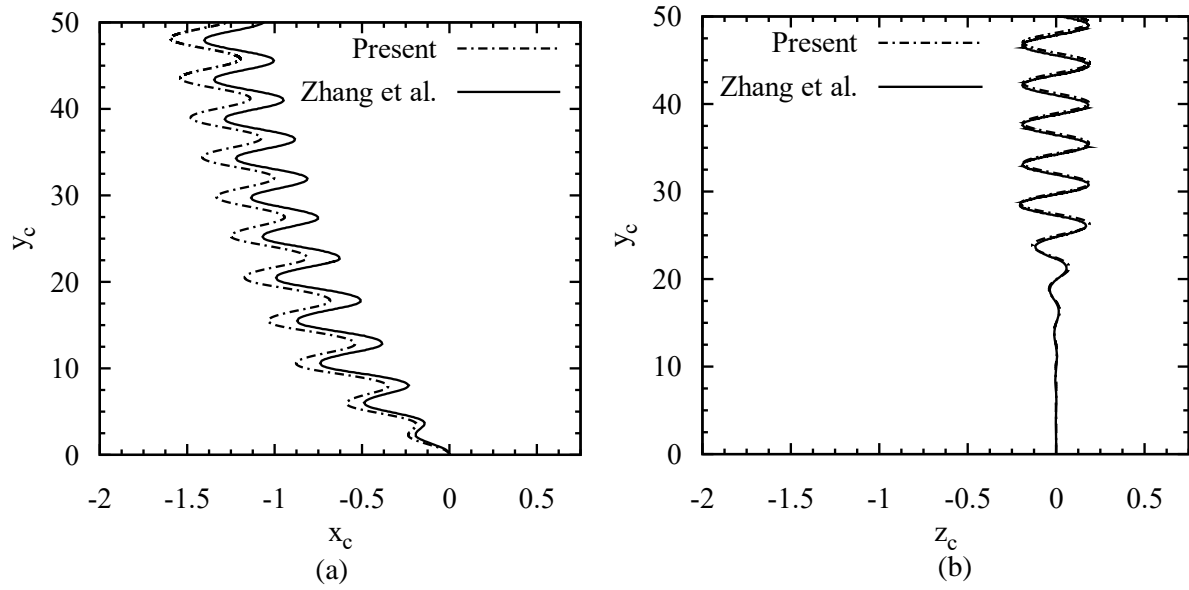
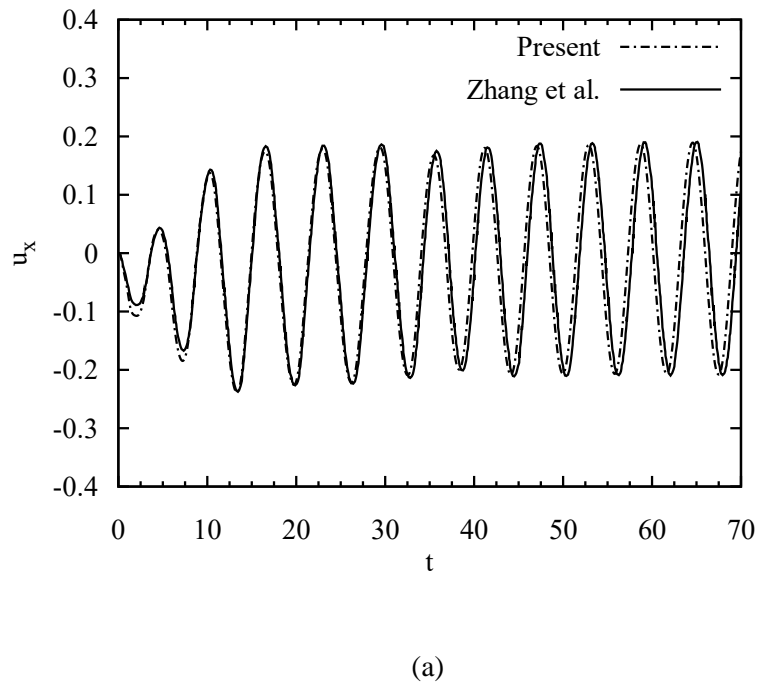


Figure 3.18: (a) Variation of  $x_c$  along vertical path  $y_c$  (front view of bubble trajectory) (b) Variation of  $z_c$  along vertical path  $y_c$  (right side view of bubble trajectory).



(a)

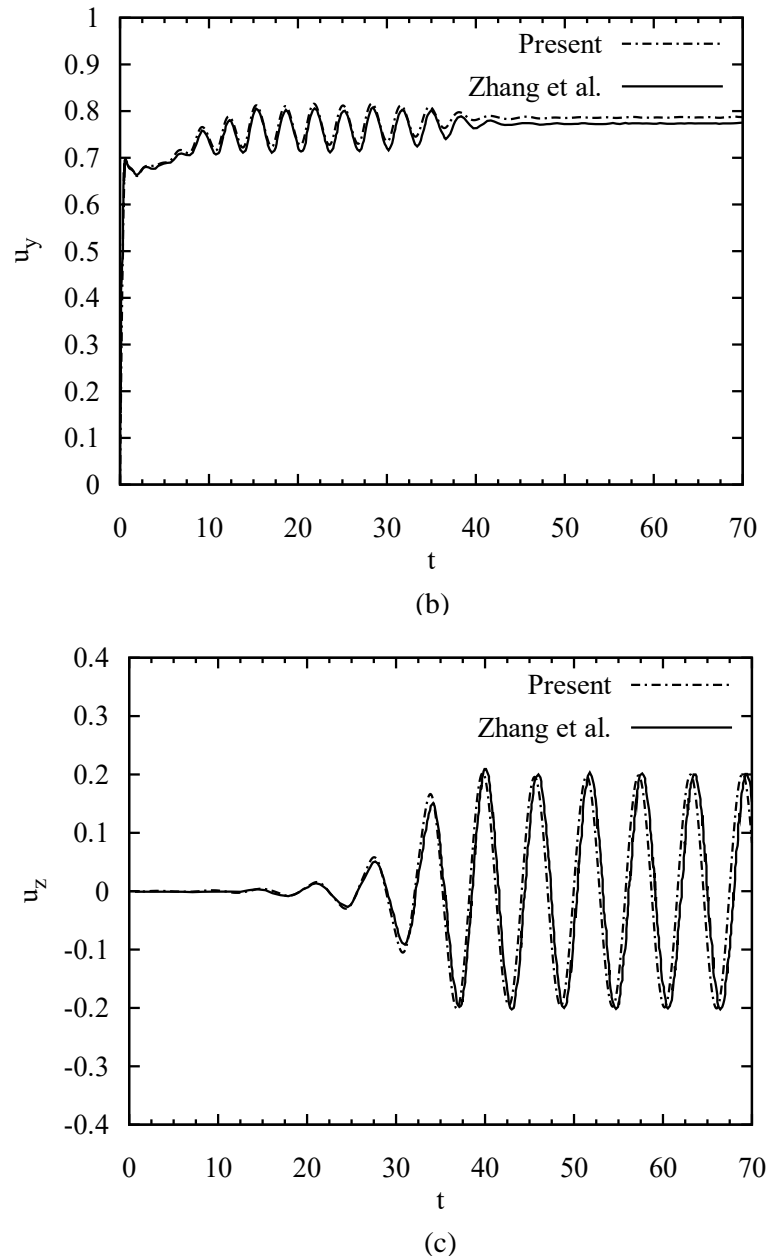


Figure 3.19: Time histories of (a) x- velocity component (b) y- velocity component (c) z- velocity component.

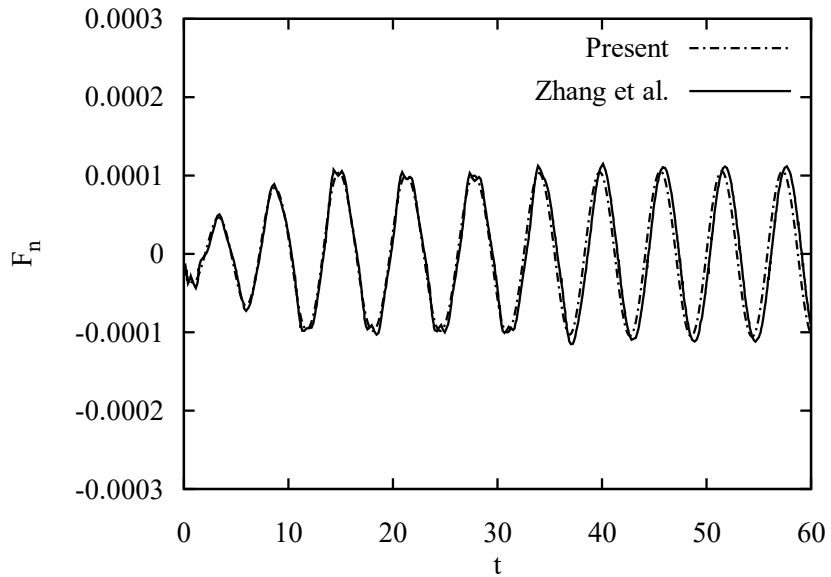


Figure 3.20: Time histories of non-dimensional force in the wall-normal direction on bubble.

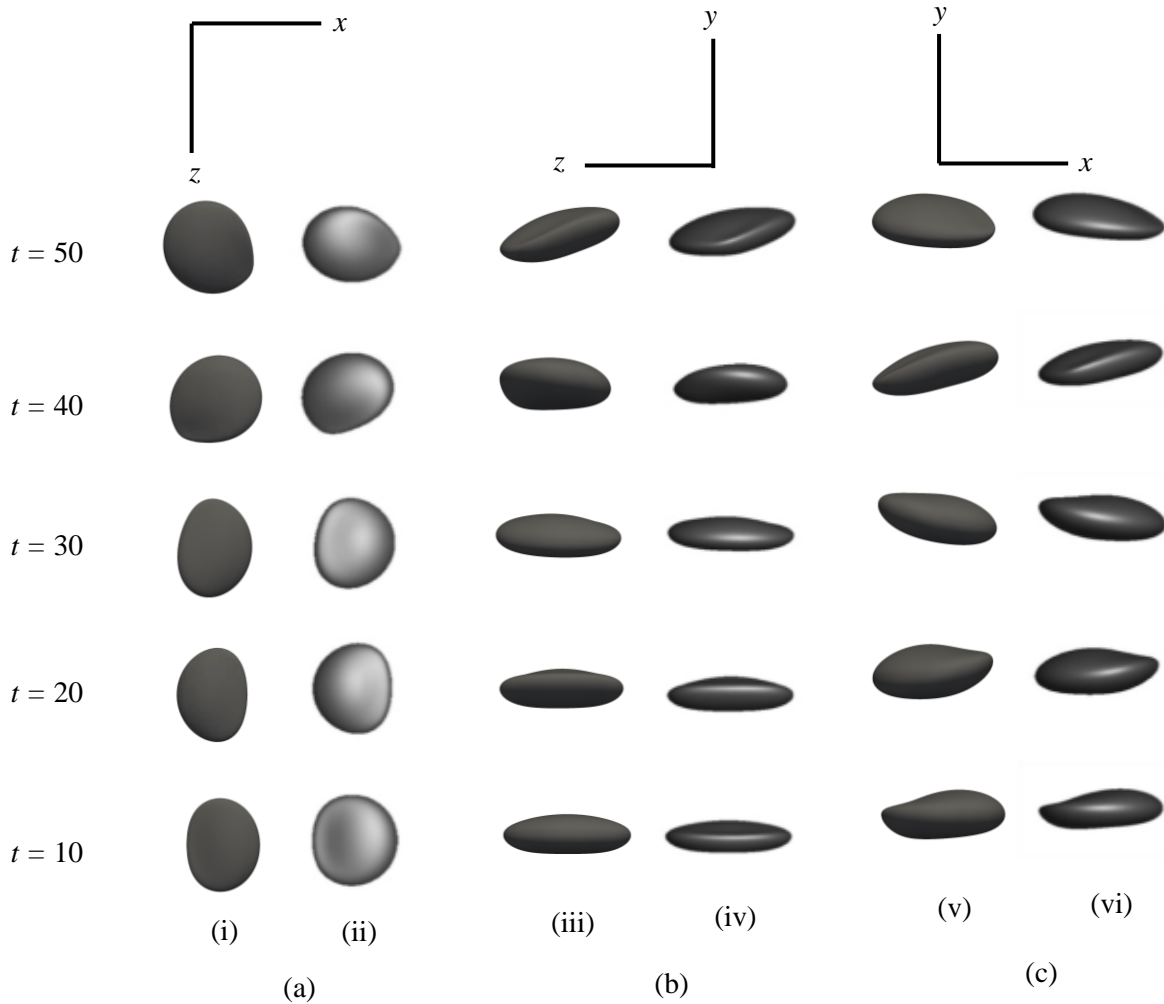


Figure 3.21: Spatio-temporal variation of bubble shapes (a) top view (b) right side view (c) front view at  $t = 10, 20, 30, 40, 50$ . (i), (iii) and (v) correspond to present results and (ii), (iv) and (vi) correspond to results from Zhang et al. [24].

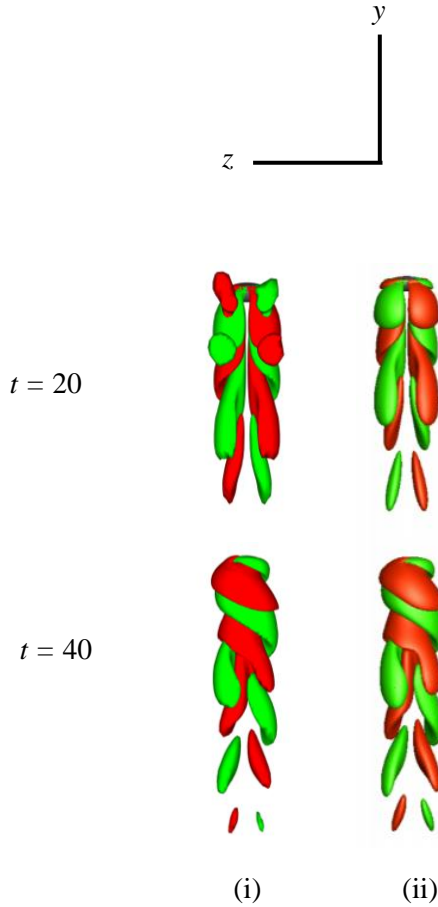


Figure 3.22: Iso-contours of the streamwise vorticity  $\omega_y = \pm 0.15$  at  $t = 20, 40$  from (i) present simulation (ii) Zhang et al. [24].

It can be seen that the trajectory and time histories plot results obtained from our code agree very well with those of Zhang et al. [24]. Only in Figure 3.18a there is slight shift of trajectory but the phases of path oscillation remain exactly the same. Time histories of velocity components and non-dimensional force show very close agreement to the original work. The spatio-temporal evolution of bubble shapes and vorticity generated behind the bubble also show great similarity to the results produced by Zhang et al. [24].

# CHAPTER 4

## RESULTS AND DISCUSSION

A total of *nine* cases were simulated to have a clear understanding of two-wall effect on path instability, bubble deformation, velocity components and vorticity generated behind bubble. The primary motive is to distinctively separate the regimes for bubble motion (viz. rectilinear, zigzag, spiral) and the effect two walls have on the transition from one regime to another. Conditional parameters of the cases simulated are tabulated below:

Table 4.1: Total cases studied

Case No.	$\rho_r$	$\mu_r$	$Eo$	$Ga$
1				40
2				55
3				57
4				60
5	1000	100	16	61
6				62
7				63.36
8				70
9				90.51

Three conditional parameters are held constant while Galilei number is varied for each case. It is to be noted that since the Galilei number is varied, Morton number will also vary as Eötvös number is constant for each case. Varying Morton number signifies that nine different liquid-air systems have to be adopted for nine different cases because Morton number is a constant for a given particular liquid-air system at a particular temperature [16, 19].

We will present the bubble trajectory as it rises under the influence of buoyancy, time histories of three velocity component along with terminal Reynolds number, evolution shape of deforming bubble and streamwise vorticity. Additionally, a comparative analysis among the cases simulated will be presented based on the behavior of the bubble that can be understood from these results.

## 4.1 Case-1 ( $Ga = 40$ )

**Trajectory:**

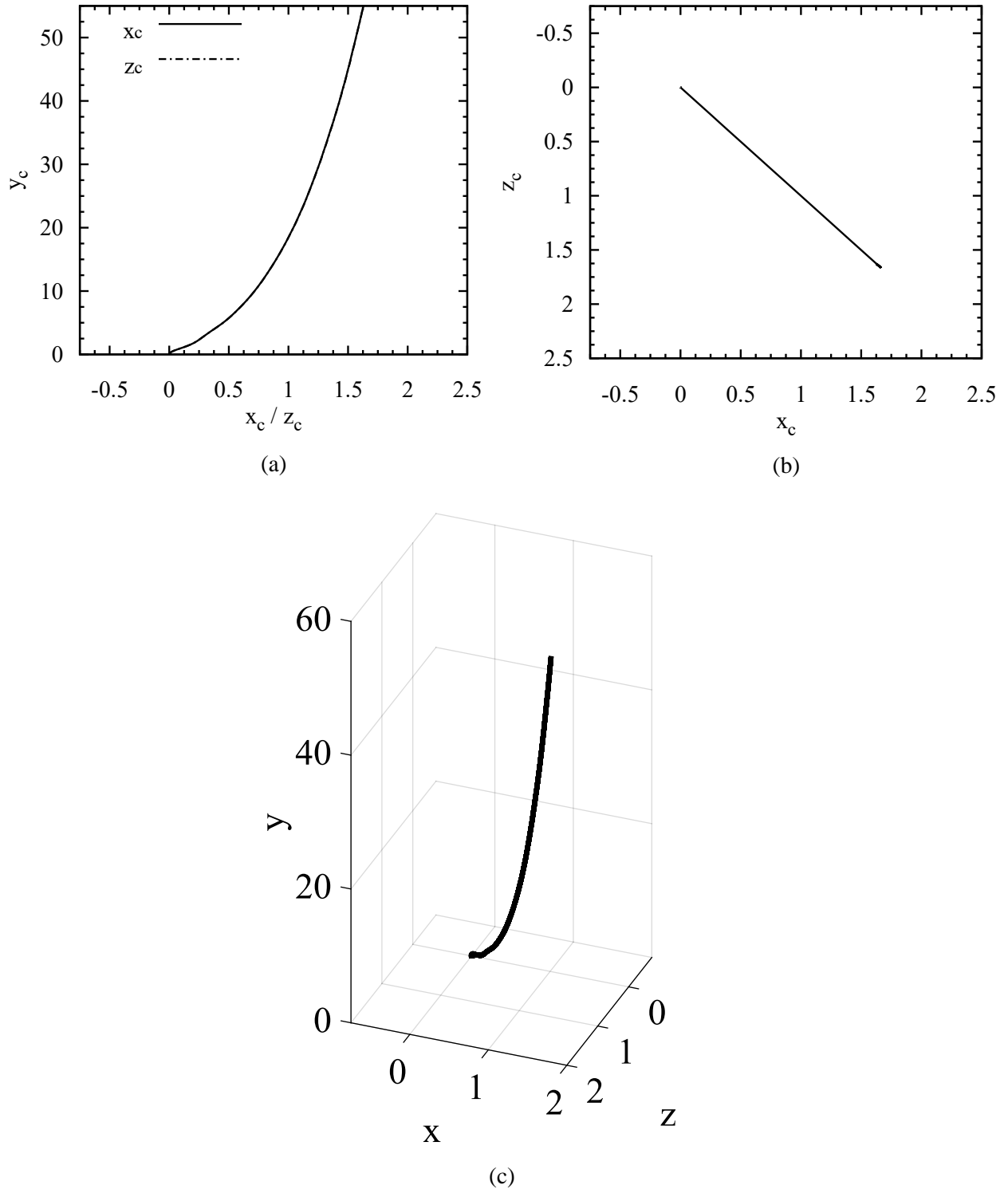


Figure 4.1: (a) Variation of  $x_c$  (front view of bubble trajectory) and  $z_c$  (side view of bubble trajectory) along  $y_c$  (b) Top view of bubble trajectory (c) Three-dimensional bubble trajectory.

**Time Histories:**

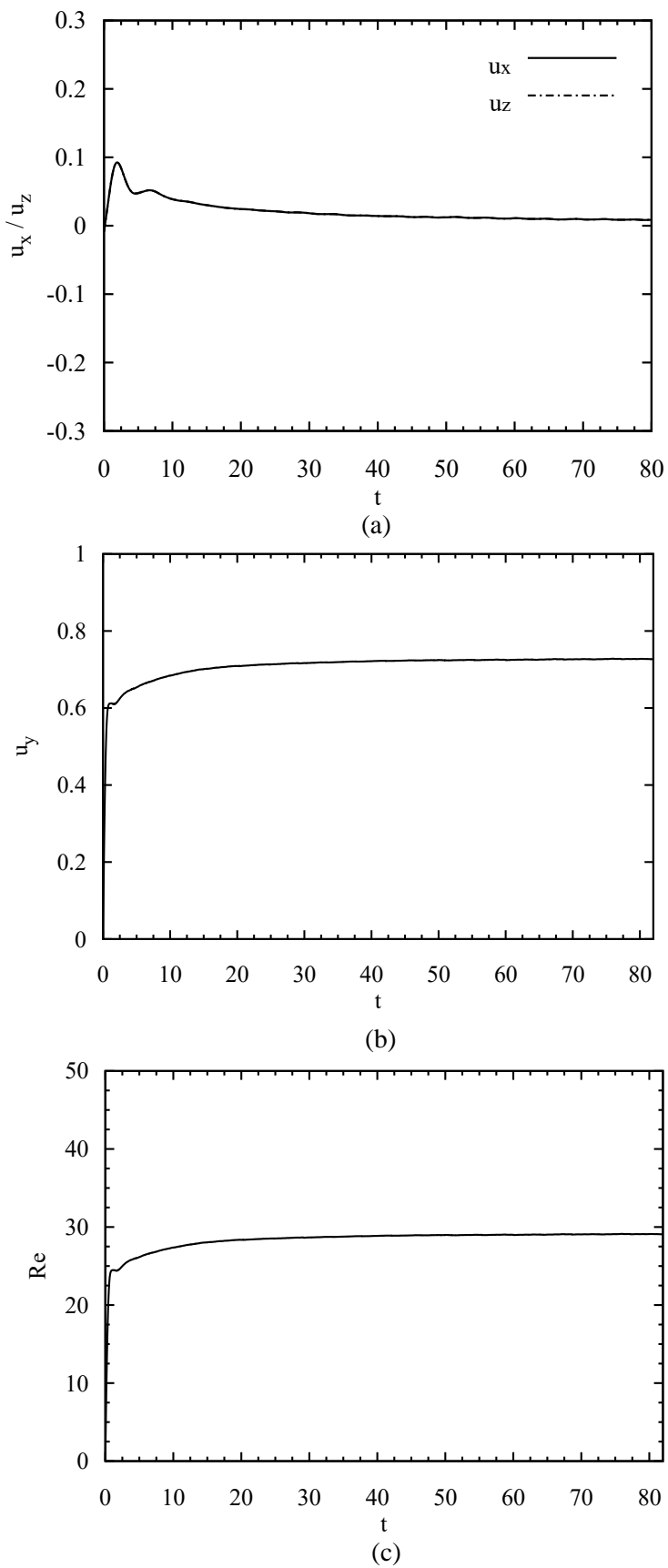
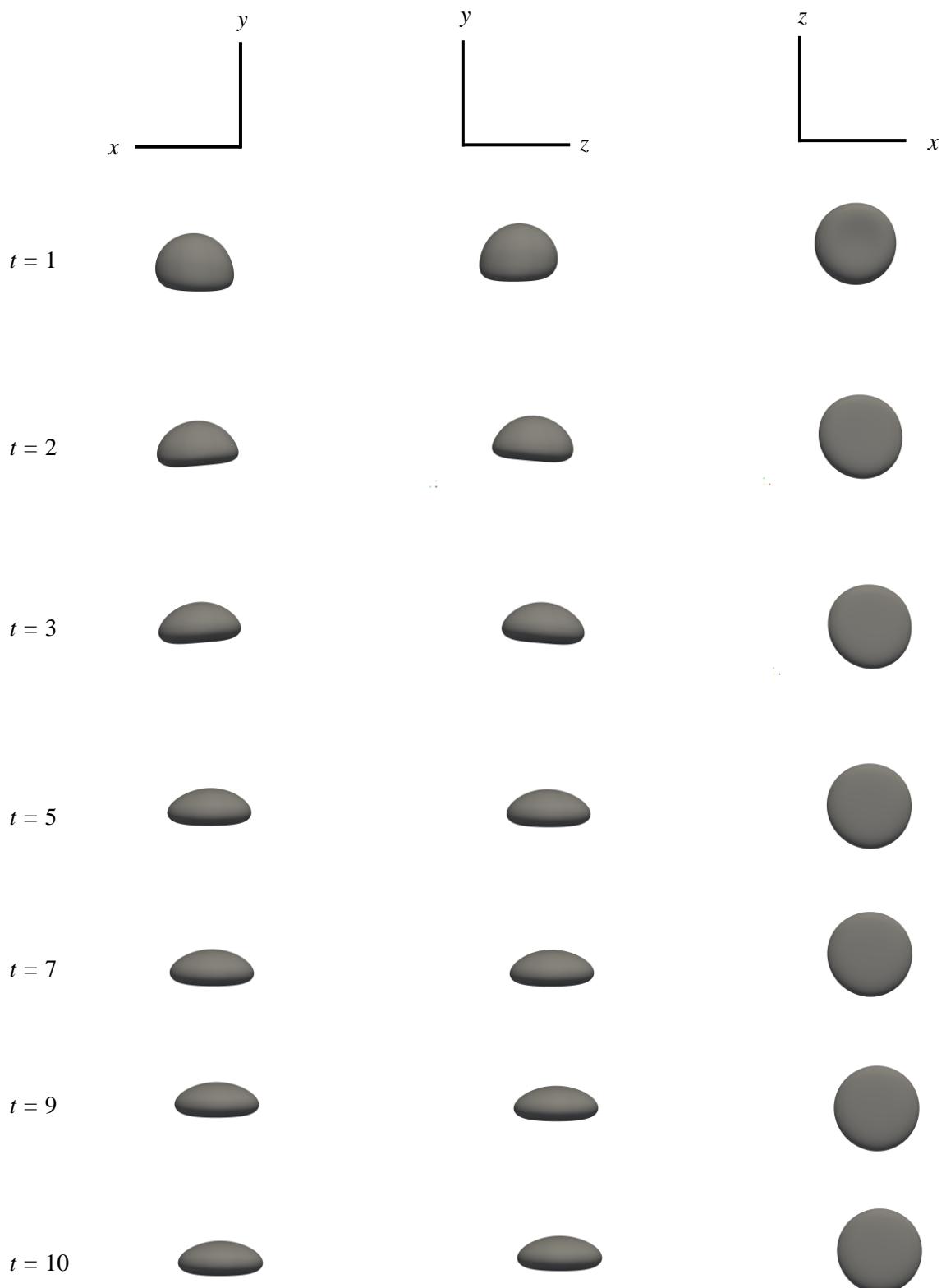


Figure 4.2: Time histories of (a) x- component and z- component of velocity (b) y- component of velocity (c) Reynolds number.

**Bubble Shapes:**



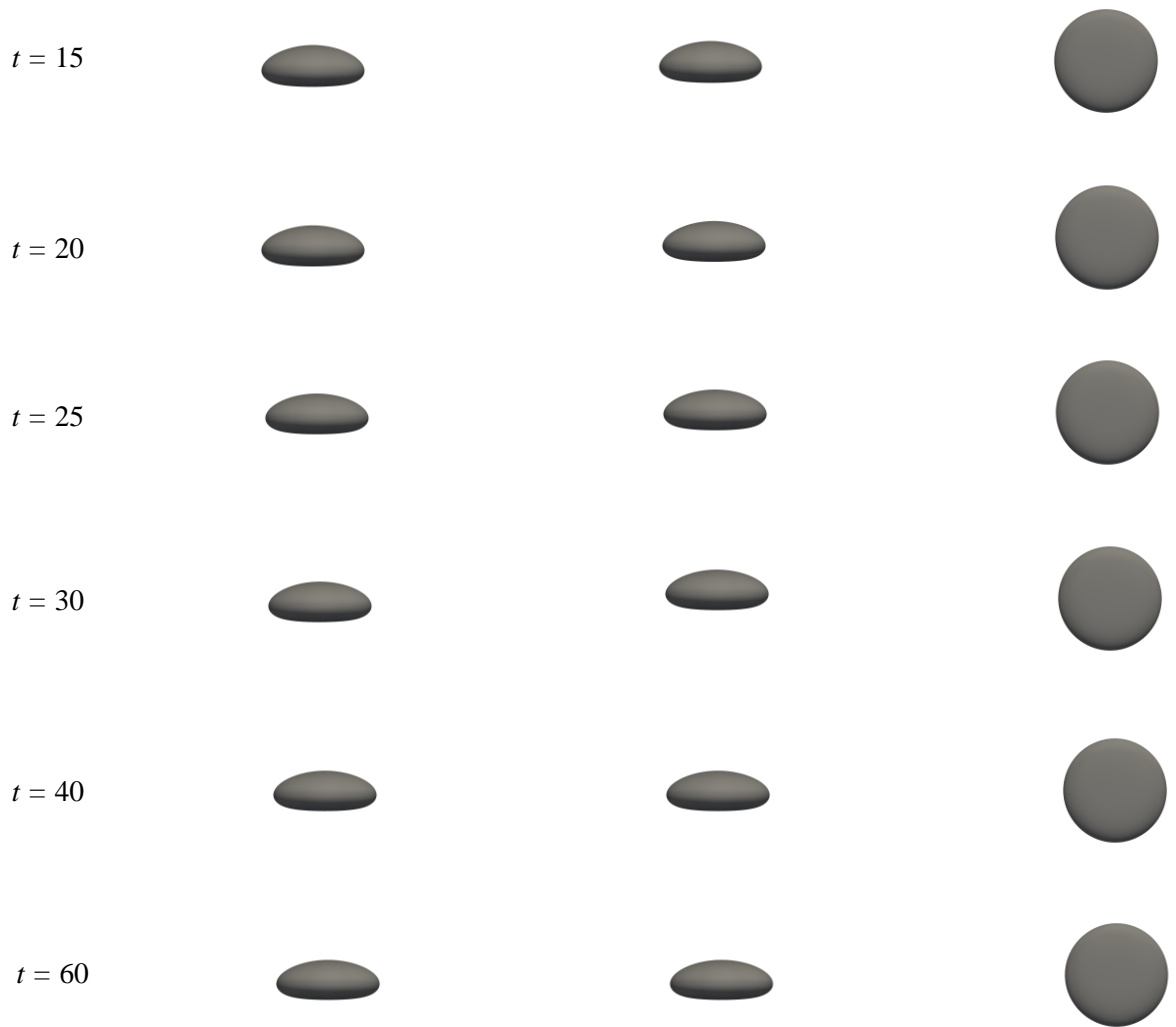
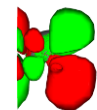
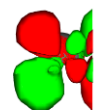


Figure 4.3: Spatio-temporal variation of bubble shape in rear, left-side and bottom view (from left to right) at  $t = 1, 2, 3, 5, 7, 9, 10, 15, 20, 25, 30, 40, 60$ .

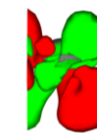
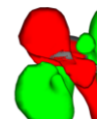
**Vorticity:**



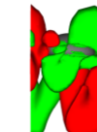
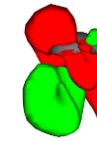
$t = 1$



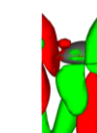
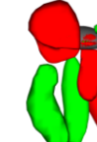
$t = 2$



$t = 3$



$t = 5$



$t = 7$



$t = 9$



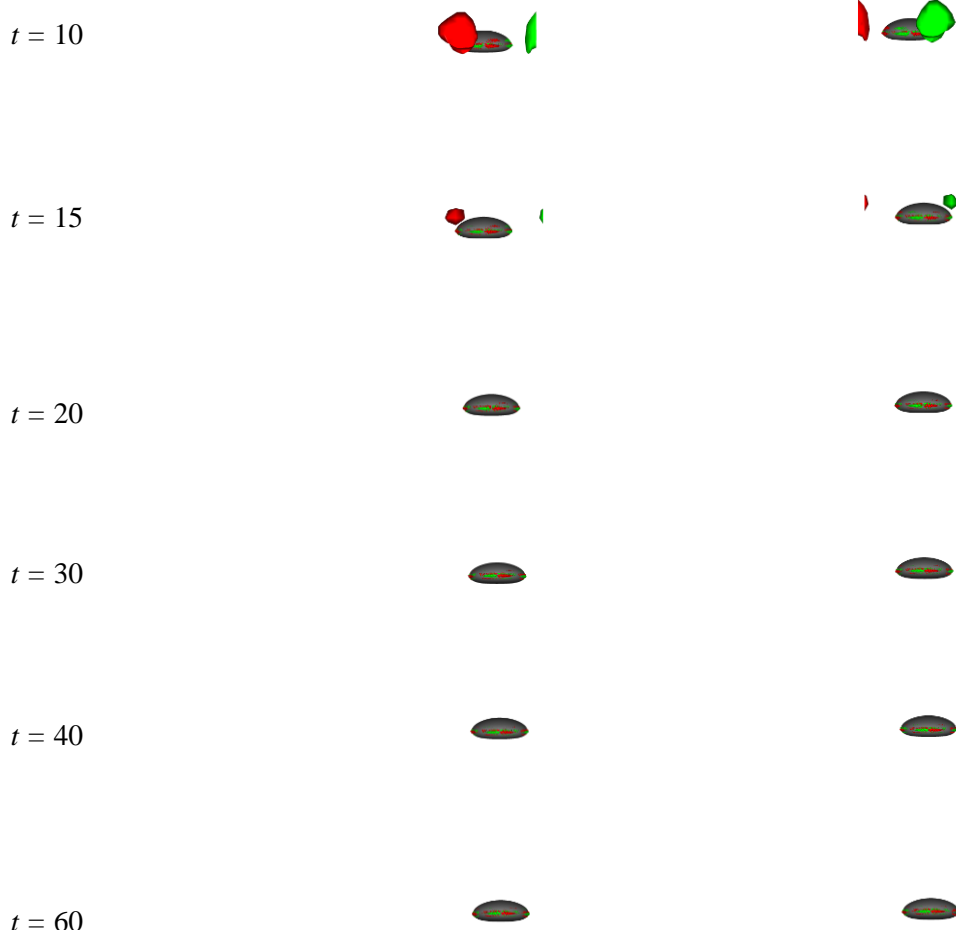


Figure 4.4: Rear (left) and left-side (right) view of iso-contours of spatio-temporal variation of streamwise vorticity  $\omega_y = \pm 0.15$  ( $\omega_y = +0.15$  for green and  $\omega_y = -0.15$  for red) at  $t = 1, 2, 3, 5, 7, 9, 10, 15, 20, 25, 30, 40, 60$ .

As can be observed from Figure 4.1, bubble starts to migrate immediately from both the rear and left-side wall as repulsive forces act on it because of the bubble-walls interaction. This happens due to generated streamwise vorticity between the bubble and walls (Figure 4.4). The initial migration, marked by a slight instability that doesn't persist for long, happens very intensively than the migration at later stages. As can be seen from Figure 4.3, bubble shapes deform heavily during the initial phases, only to conform to a stable shape after  $t = 15$ . It is to be noted that, the rising velocity as illustrated in Figure 4.2b starts reaching its terminal state after  $t = 15$  which indicate that there might be a cause-and-effect relation between the vorticity generation and terminal rising velocity of bubble.

Since, the vertical walls are both having their effects on bubble, bubble migrates diagonally in a curvilinear path in the three-dimensional space illustrated in Figure 4.1b and 4.1c which is different from bubble with one vertical wall [24]. After an initial transitional phase (too small temporally), the trajectory shows a curvilinear motion that persists for rest of the rising time. It is also to be noted that the bubble position in Figure 4.1a and velocity in Figure 4.2a in x-y and z-y plane is similar for this particular case indicating both walls having same effect on the dynamics of bubble.

Since the oscillating nature of x- and z- velocity component is very low and the initial transient too short, the regime is identified as *Steady*.

## 4.2 Case-2 (Ga = 55)

**Trajectory:**

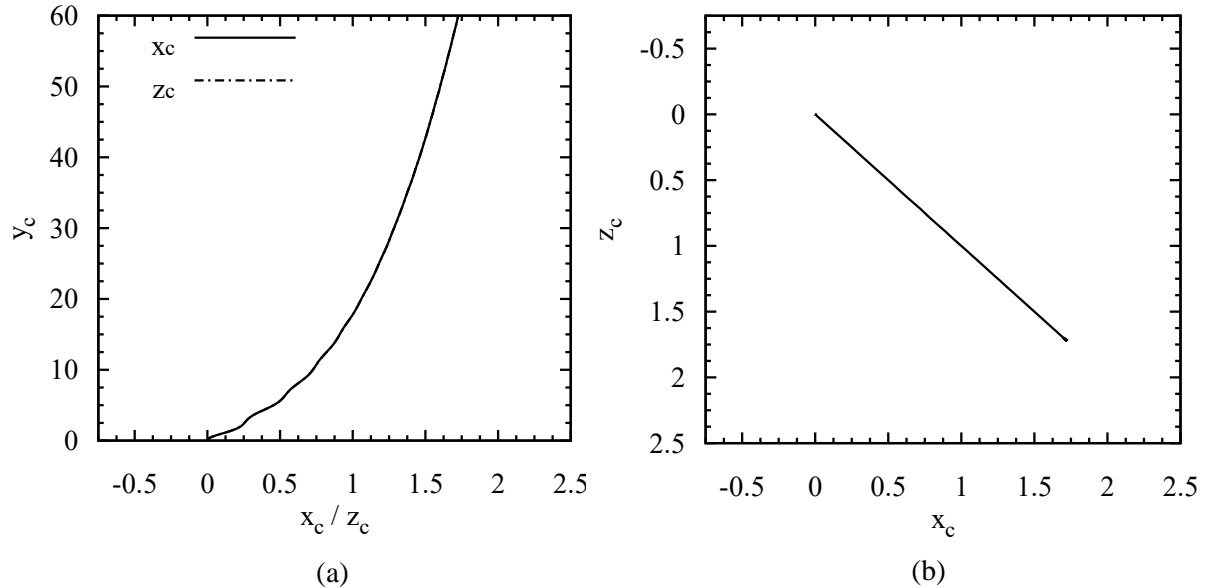


Figure 4.5: (a) Variation of  $x_c$  (front view of bubble trajectory) and  $z_c$  (side view of bubble trajectory) along  $y_c$  (b) Top view of bubble trajectory (c) Three-dimensional bubble trajectory.

**Time Histories:**

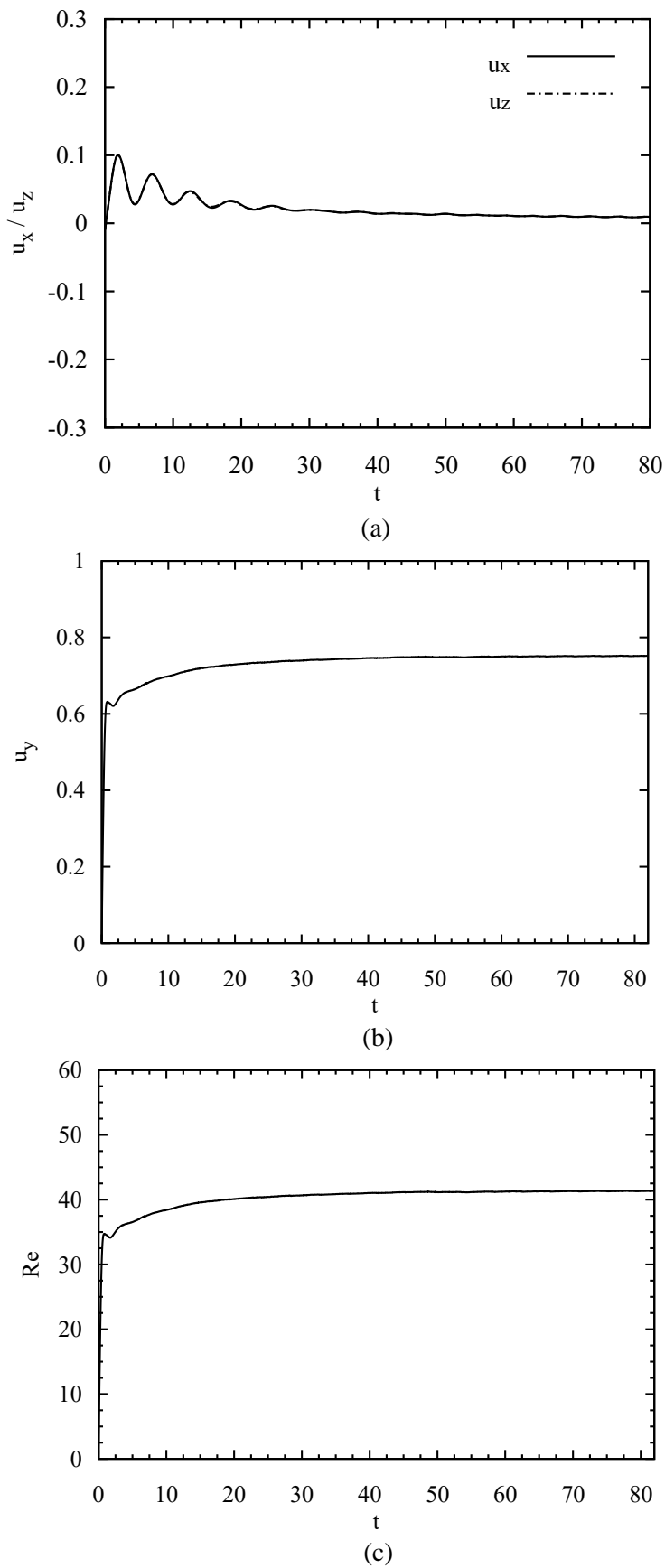
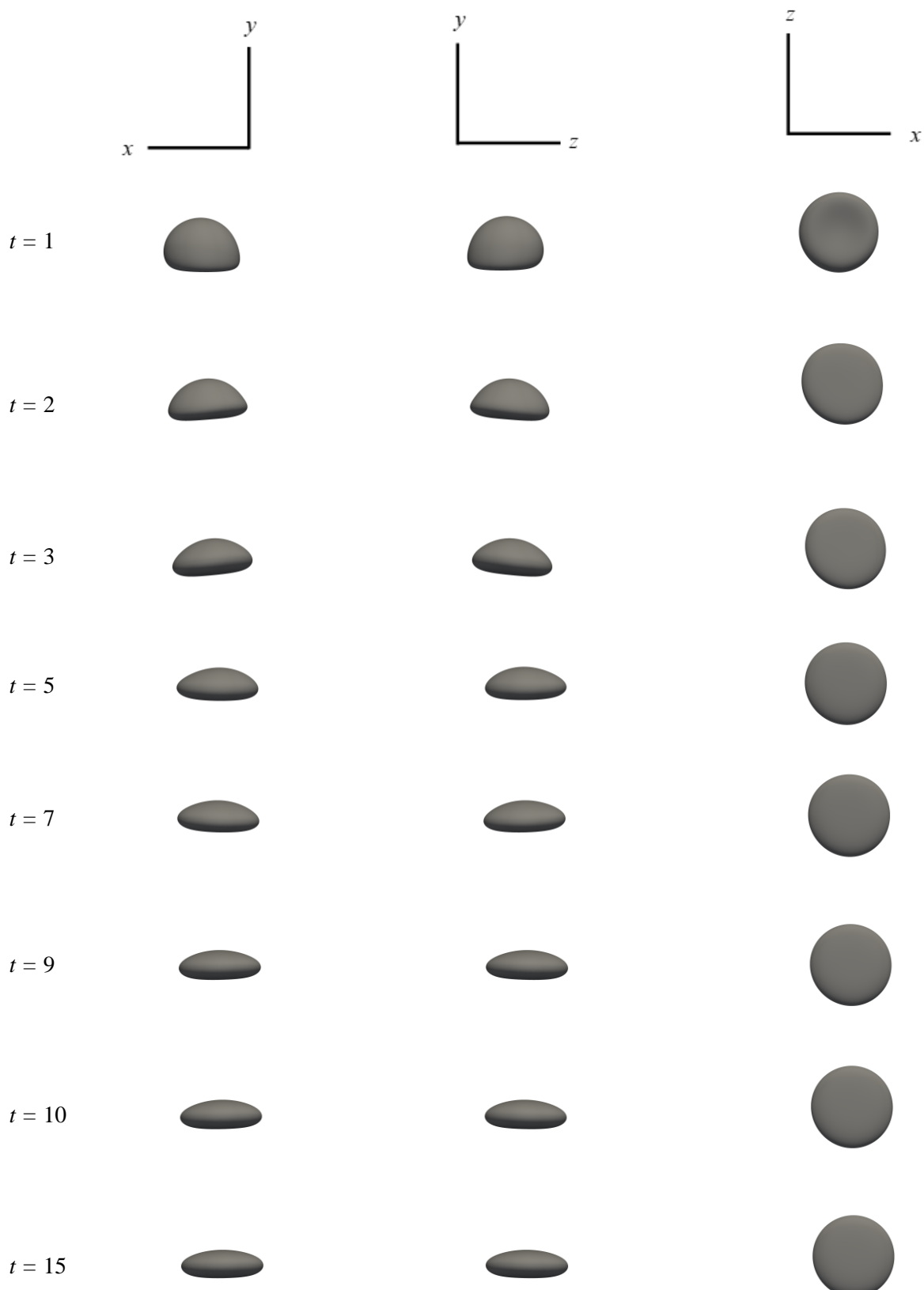


Figure 4.6: Time histories of (a) x- component and z- component of velocity (b) y- component of velocity (c) Reynolds number.

**Bubble Shapes:**



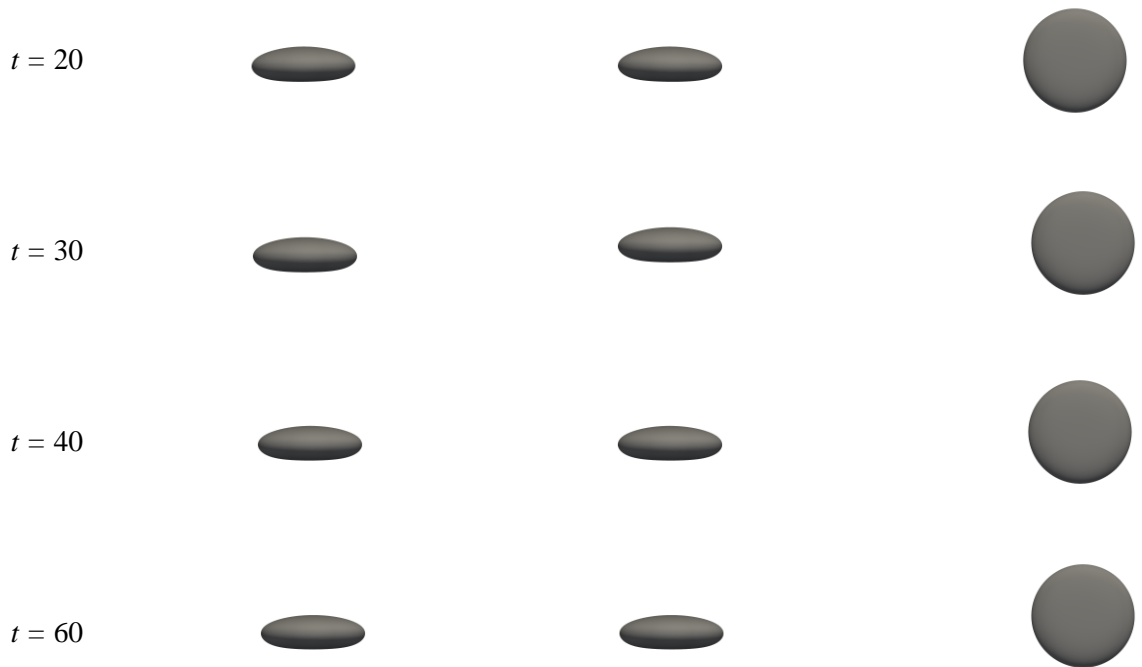
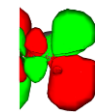
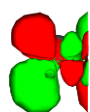


Figure 4.7: Spatio-temporal variation of bubble shape in rear, left-side and bottom view (from left to right) at  $t = 1, 2, 3, 5, 7, 9, 10, 15, 20, 30, 40, 60$ .

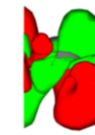
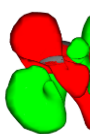
**Vorticity:**



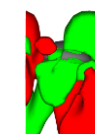
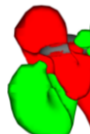
$t = 1$



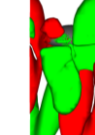
$t = 2$



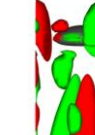
$t = 3$



$t = 5$



$t = 7$



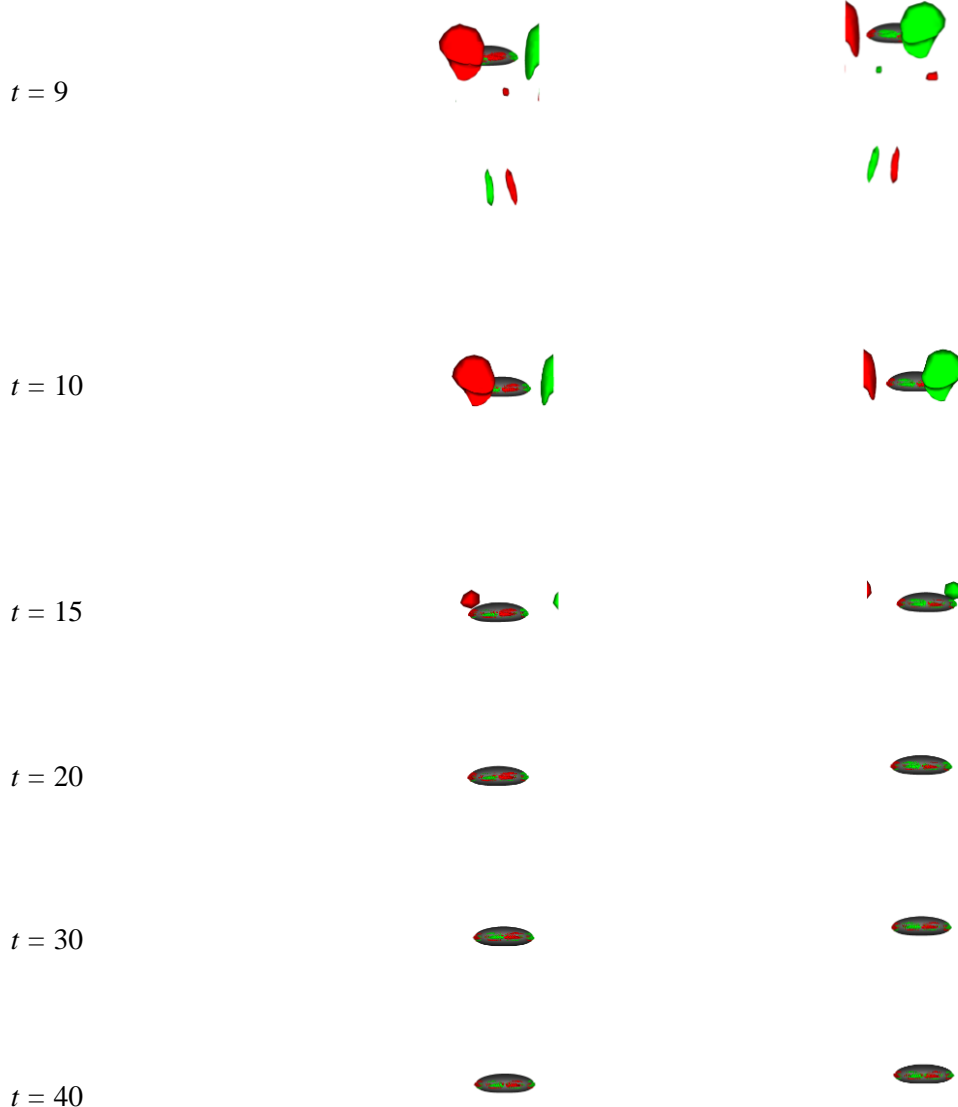


Figure 4.8: Rear (left) and left-side (right) view of iso-contours of spatio-temporal variation of streamwise vorticity  $\omega_y = \pm 0.15$  ( $\omega_y = +0.15$  for green and  $\omega_y = -0.15$  for red) at  $t = 1, 2, 3, 5, 7, 9, 10, 15, 20, 30, 40$ .

As can be observed from Figure 4.5 and Figure 4.6, the initial transient caused by bubble-walls interaction because of vorticity generated between them persists longer than case-1. So, certain path instability occurs till  $t = 25$ . The reason why the instability persistence is longer, might be because value of vortices accumulated over bubble surface (mainly on its edge) for that period is greater than a critical value that would retain the path instability. The accumulation of vortices of certain amount on surface that would cause path instability might simply last shorter for case-1, hence the short span of initial instability. Again, the interconnectedness between streamwise vorticity and bubble deformation is noticed. As, the vortex structure behind the bubble diminishes, bubbles stop deforming and takes an oblate ellipsoidal shape like case-1 as can be seen from Figure 4.8 and 4.7 respectively.

After the initial transient, the oscillating nature dies out both in path and velocity and bubble follows a curvilinear path like case-1. So, it is to be understood that, the accumulation of vorticity over bubble decreases over time and as remarked by other researchers [12, 53], with vorticity less than a critical

value over bubble, path instability doesn't occur. As a result, bubble transitions from somewhat longer transient to steady curvilinear path. That's why this bubble is identified in the *Transition* regime.

### 4.3 Case-3 (Ga = 57)

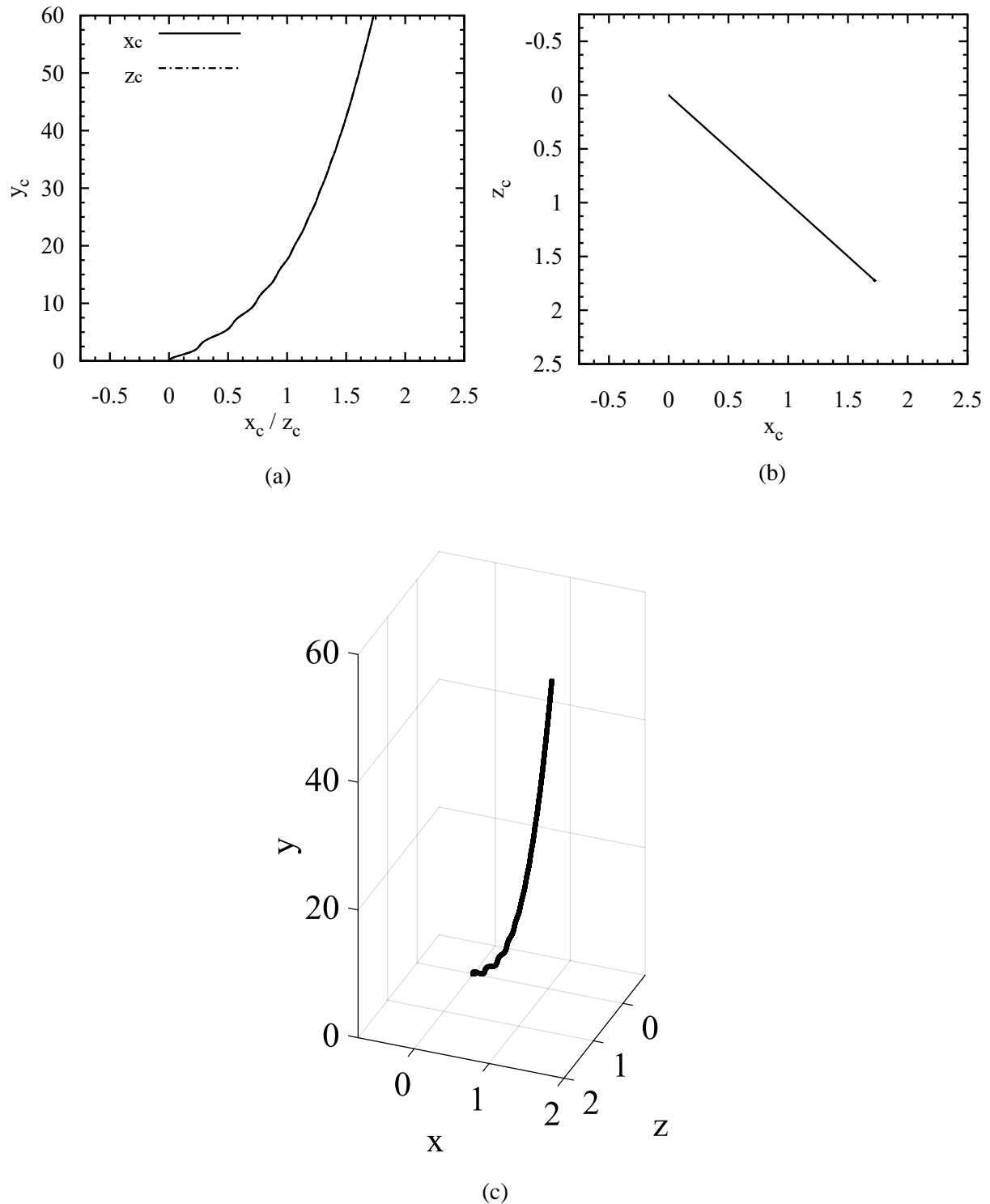


Figure 4.9: (a) Variation of  $x_c$  (front view of bubble trajectory) and  $z_c$  (side view of bubble trajectory) along  $y_c$  (b) Top view of bubble trajectory (c) Three-dimensional bubble trajectory.

**Time Histories:**

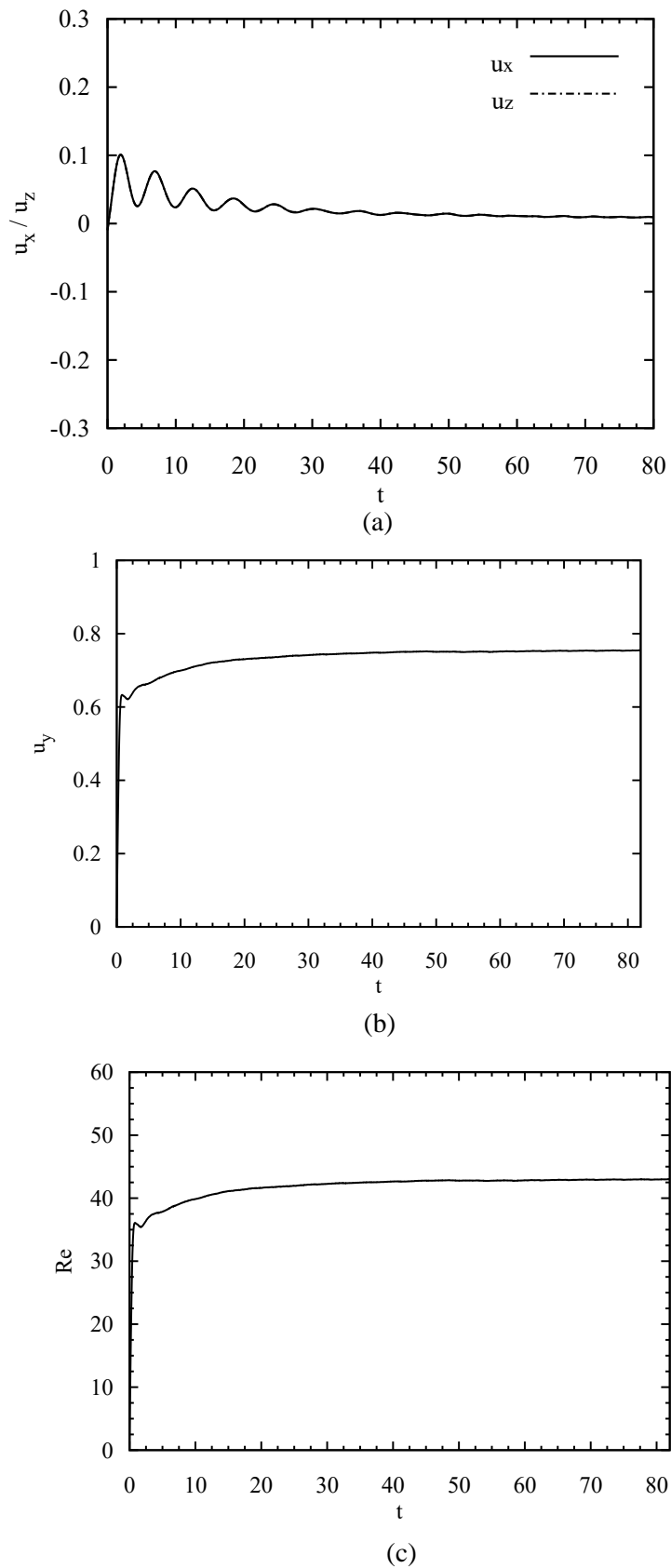
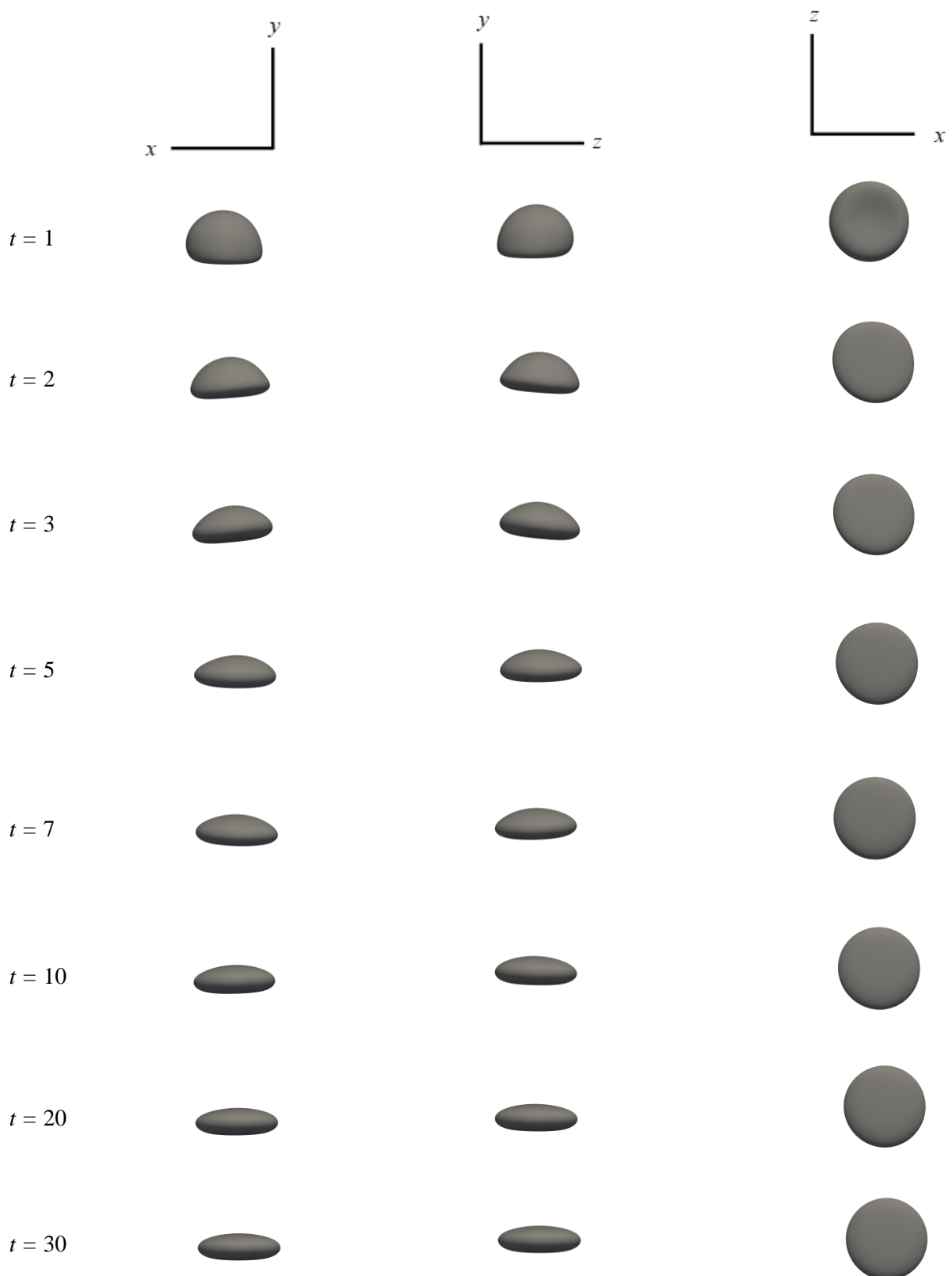


Figure 4.10: Time histories of (a) x- component and z- component of velocity (b) y- component of velocity (c) Reynolds number.

**Bubble Shapes:**



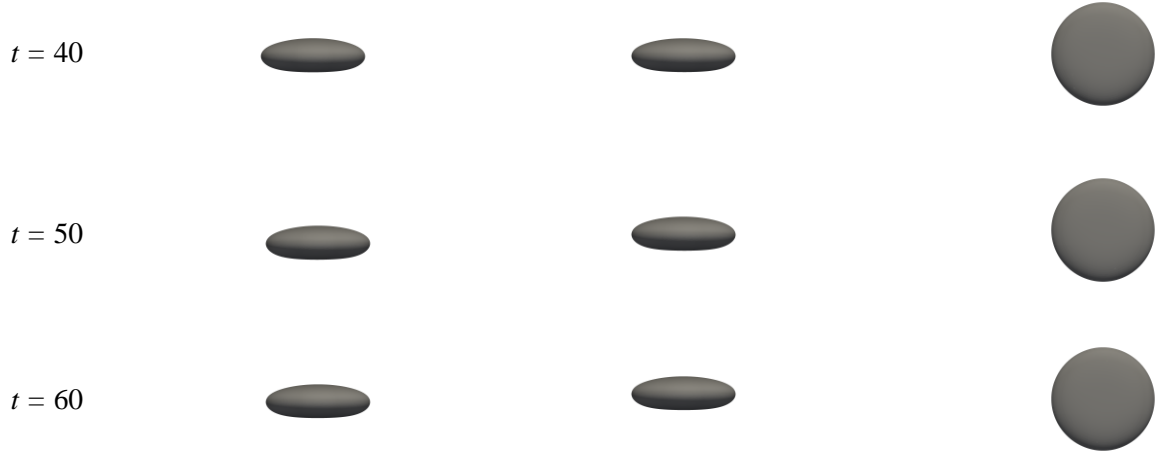
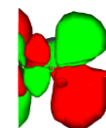
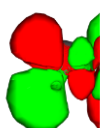


Figure 4.11: Spatio-temporal variation of bubble shape in rear, left-side and bottom view (from left to right) at  $t = 1, 2, 3, 5, 7, 10, 20, 30, 40, 50, 60$ .

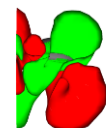
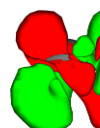
**Vorticity:**



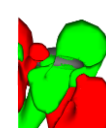
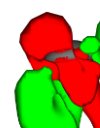
$t = 1$



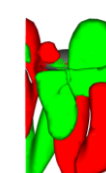
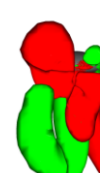
$t = 2$



$t = 3$



$t = 5$



$t = 7$



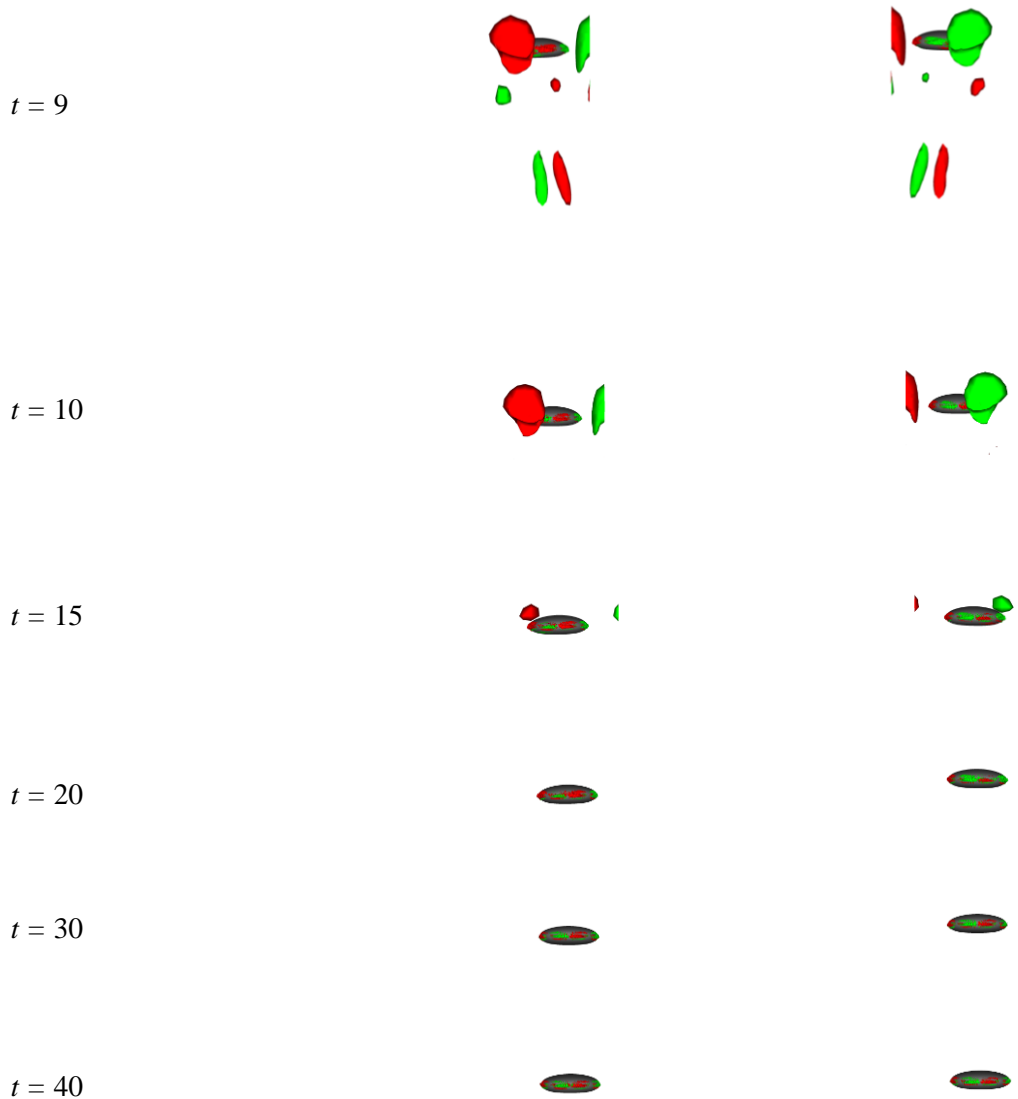


Figure 4.12: Rear (left) and left-side (right) view of iso-contours of spatio-temporal variation of streamwise vorticity  $\omega_y = \pm 0.15$  ( $\omega_y = +0.15$  for green and  $\omega_y = -0.15$  for red) at  $t = 1, 2, 3, 5, 7, 9, 10, 15, 20, 30, 40$ .

For this case, the oscillating nature both in trajectory and velocity as can be seen from Figure 4.9a, 4.9c and 4.10a respectively persists a little longer and the bubble takes more time to reach its terminal rising velocity as can be seen from Figure 4.10b. It reaches the terminal state around  $t = 40$  which is longer than both the previous cases. Again, after the initial induced path instability because of bubble-walls interaction, bubble takes up the curvilinear path like case-1 and case-2.

An important trend to note here is that, the bubble-walls interaction induces more or less similar amount of wakes in initial phases for cases simulated so far. It's the wake accumulated on the surface that differs as the bubble progressively moves away from both the walls (Figure 4.12). The greater the period for which the value of vortices remains above a certain critical value, the longer the path instability persists.

The bubble again takes up the oblate ellipsoidal shape as its terminal shape as can be seen from Figure 4.11. As the path instability isn't yet fully developed and the bubble takes the eventual curvilinear path, the regime is still identified as *Transition*.

## 4.4 Case-4 (Ga = 60)

**Trajectory:**

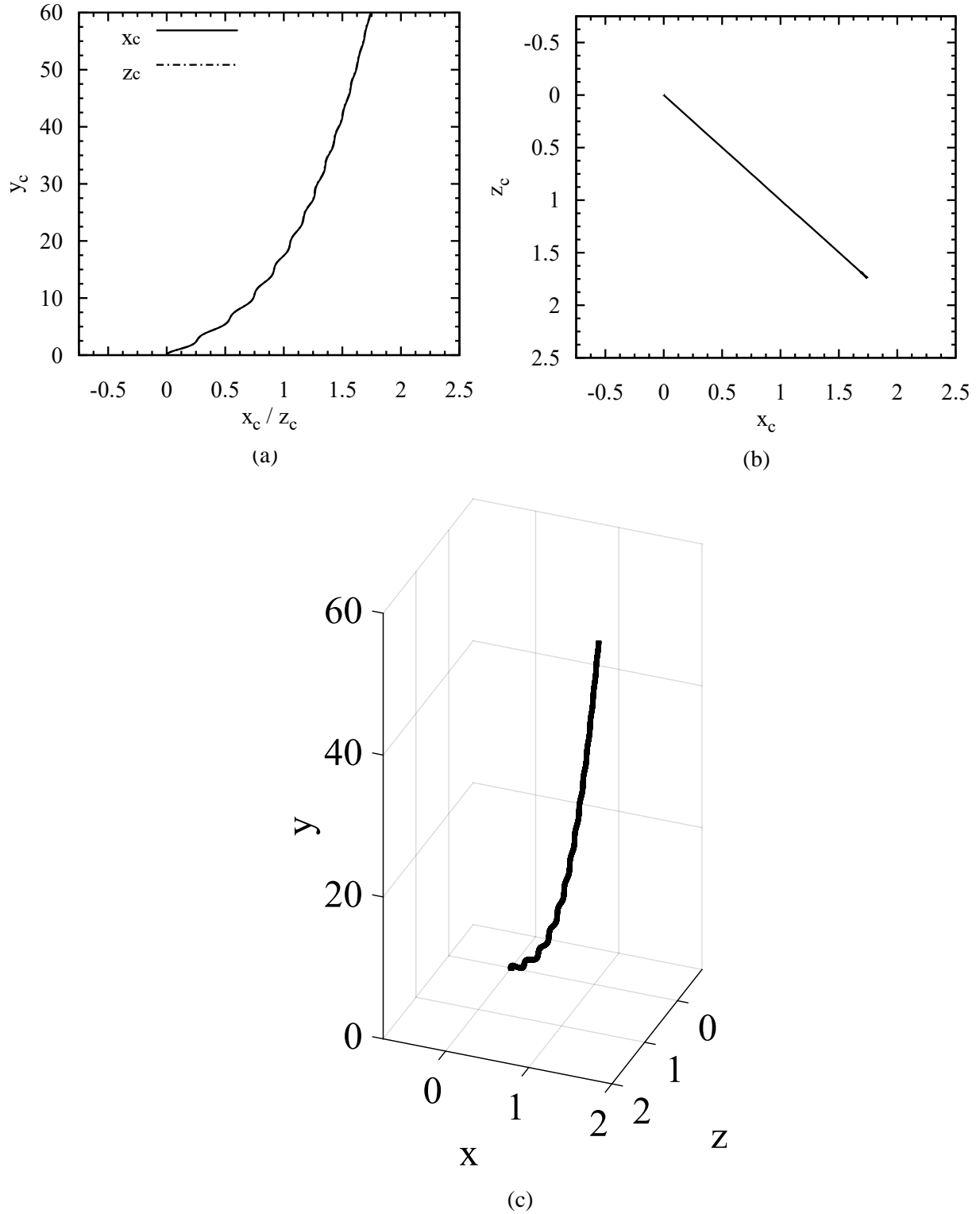


Figure 4.13: (a) Variation of  $x_c$  (front view of bubble trajectory) and  $z_c$  (side view of bubble trajectory) along  $y_c$  (b) Top view of bubble trajectory (c) Three-dimensional bubble trajectory.

**Time histories:**

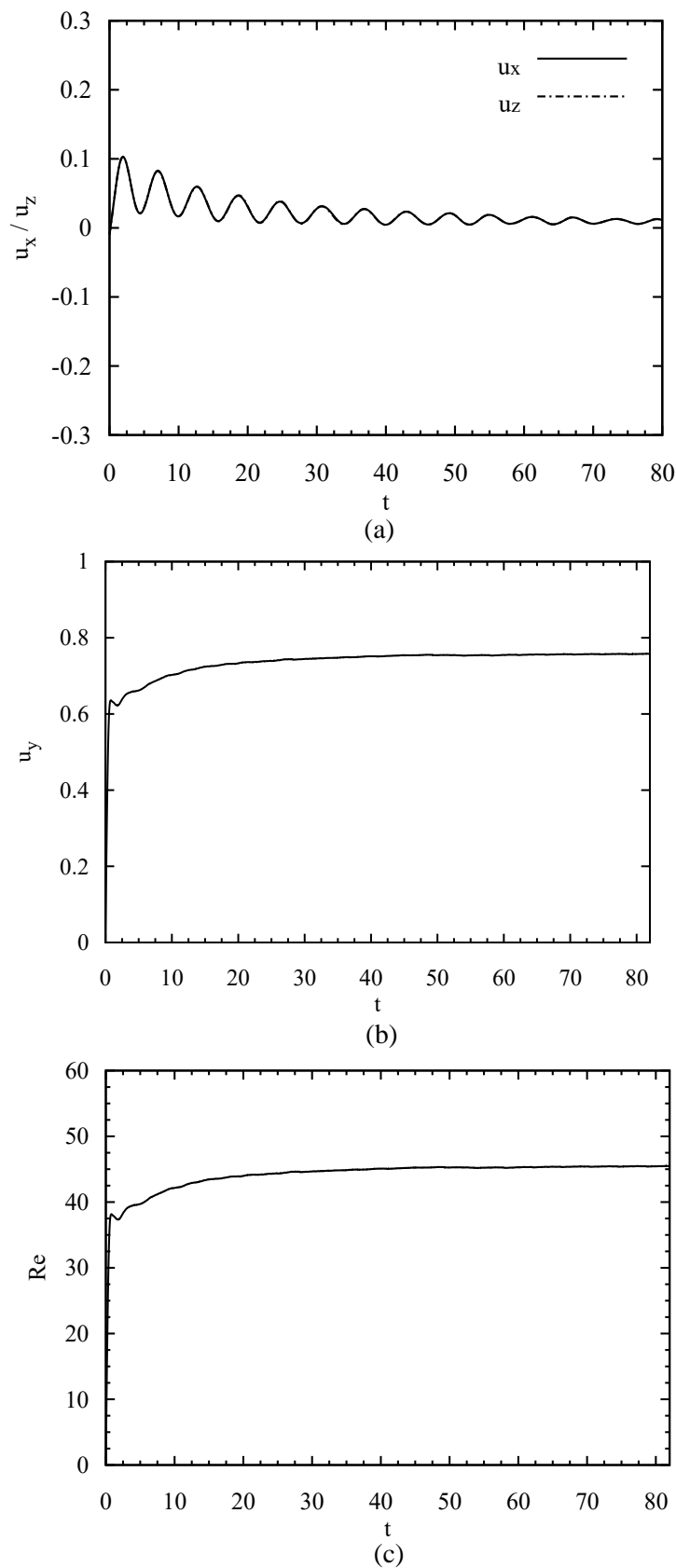
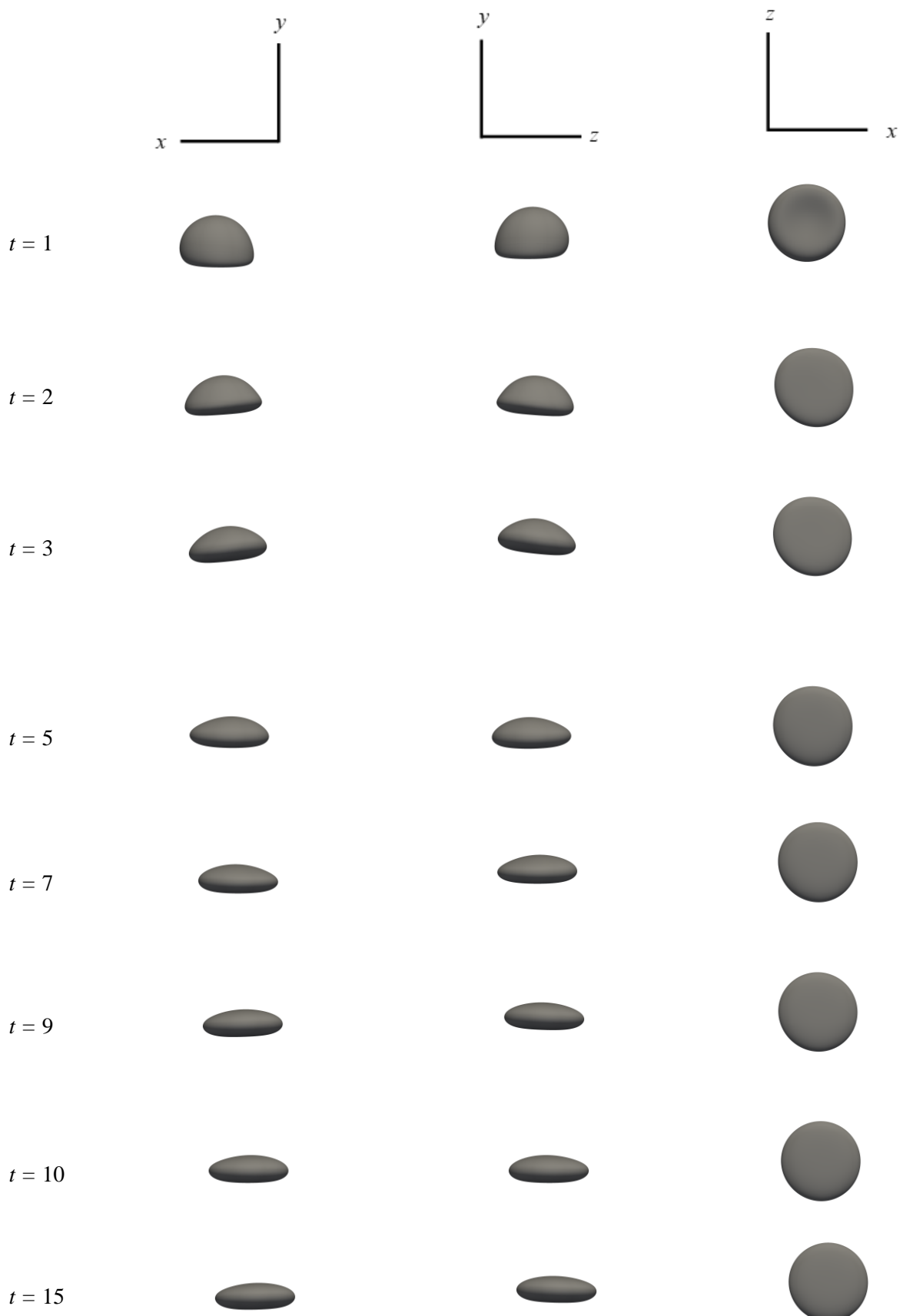


Figure 4.14: Time histories of (a) x- component and z- component of velocity (b) y- component of velocity (c) Reynolds number.

**Bubble Shapes:**



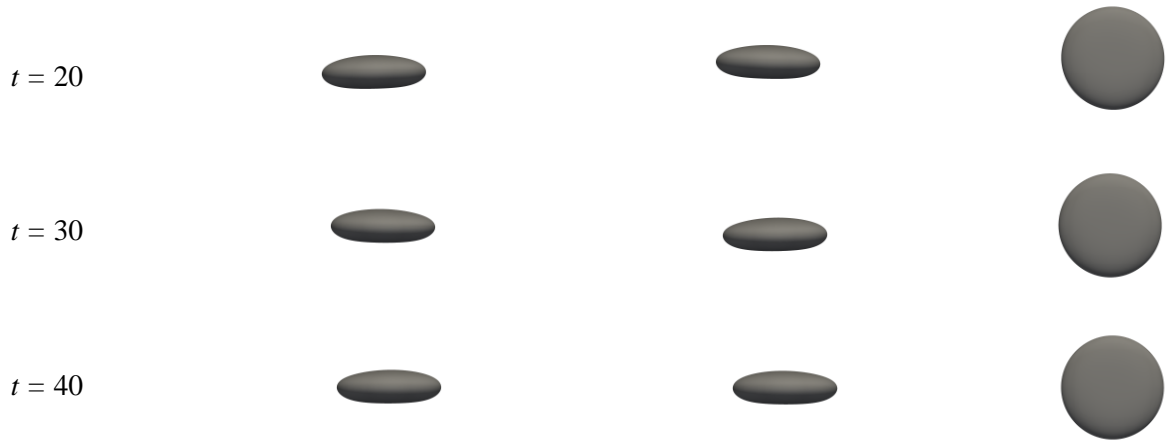
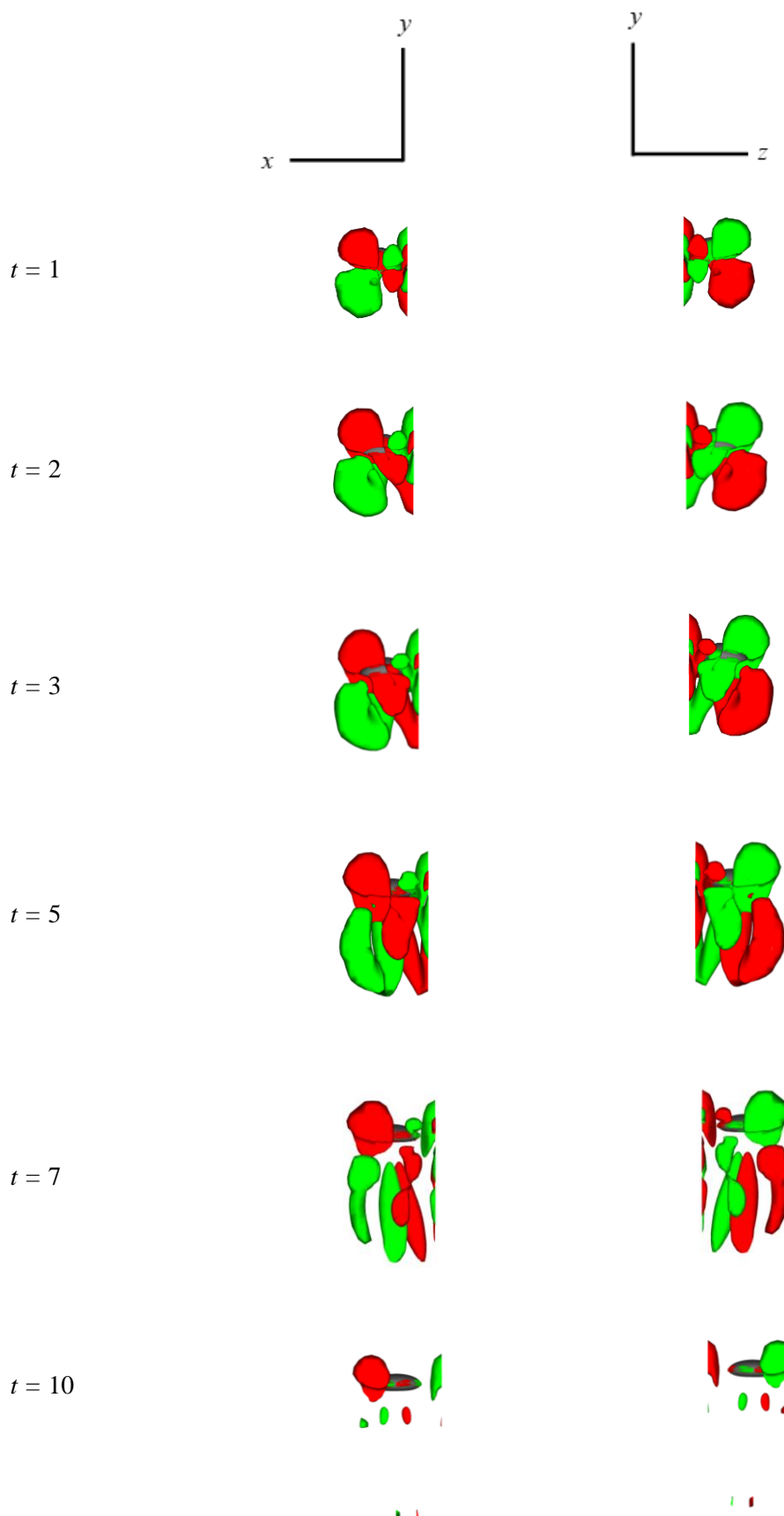


Figure 4.15: Spatio-temporal variation of bubble shape in rear, left-side and bottom view (from left to right) at  $t = 1, 2, 3, 5, 7, 9, 10, 15, 20, 30, 40$ .

**Vorticity:**



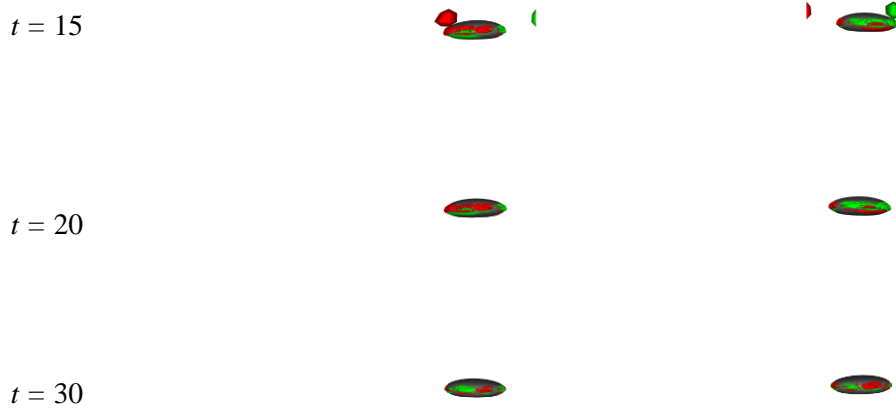


Figure 4.16: Rear (left) and left-side (right) view of iso-contours of spatio-temporal variation of streamwise vorticity  $\omega_y = \pm 0.15$  ( $\omega_y = +0.15$  for green and  $\omega_y = -0.15$  for red) at  $t = 1, 2, 3, 5, 7, 10, 15, 20, 30$ .

From Figure 4.13a, 4.13c and 4.14a, it is clear that the bubble exhibits trajectory that oscillates for a longer period of time while rising case-1, case-2 and case-3. Figure 4.13b suggests the confinement of bubble trajectory in a diagonal plane of around  $45^\circ$  like previous cases. Velocity components in wall normal direction increases and decreases periodically suggesting that the bubble moves changes direction while moving (acceleration and deceleration). This is the sign of showing path instability in its developed form. But as time passes by, the oscillation seems to diminish to smaller amplitude progressively, though the frequency remains the same. This behavior can be attributed to *Transition* regime as the path instability is not fully developed yet. The initial bubble-walls interaction persists as bubble migrate away from the walls. The bubble inertia set by the walls makes itself migrate away diagonally even if bubble is sufficiently distant from walls to not have their further influence on it.

Vortices accumulated on the edge of bubble surface is greater here than previous three cases when the bubble is distant from both the walls (Figure 4.16). This further approves the point made earlier that the greater amount of vortices for longer period attributes to the path instability of bubble for longer period. But again, it's not enough to induce fully developed path instability as the path conforms to the curvilinear trajectory as observed for earlier cases.

Bubble deformation takes place for longer period because of bubble inertia induced from bubble-walls interaction (Figure 4.15) and the greater amount of vortices on bubble surface. The cause-and-effect point made earlier still holds up as the behavioral phenomena seem to interdepend upon each other. It's tough to point out the exact cause here among the four behavioral phenomena we are investigating as Cano-Lozano et al. [17] believed wake instability isn't always the cause for path instability and other behavioral phenomena. But the difference here between the study of Cano-Lozano et al. [17] and here is that the comments made by Cano-Lozano et al. [17] was based on bubble in unconfined condition while two walls are acting as destabilizing factor in our case and affecting the bubble inertia at later stages of its motion. So, the inertial influence from the walls coupled with the wake instability due to its accumulation on the bubble surface can be a contributing factor to its persistent yet not-fully-developed path instability.

## 4.5 Case-5 ( $Ga = 61$ )

**Trajectory:**

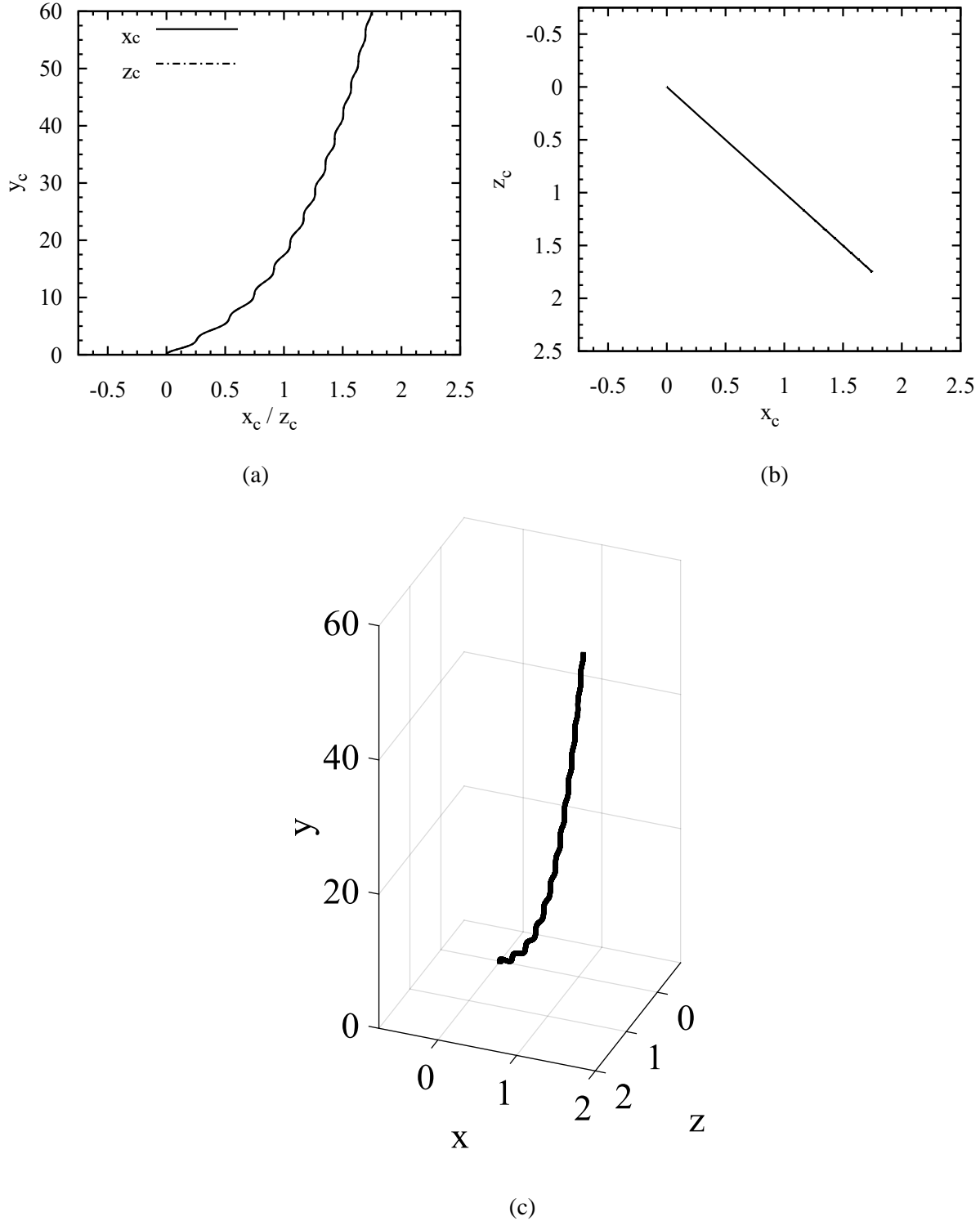


Figure 4.17: (a) Variation of  $x_c$  (front view of bubble trajectory) and  $z_c$  (side view of bubble trajectory) along  $y_c$  (b) Top view of bubble trajectory (c) Three-dimensional bubble trajectory.

**Time Histories:**

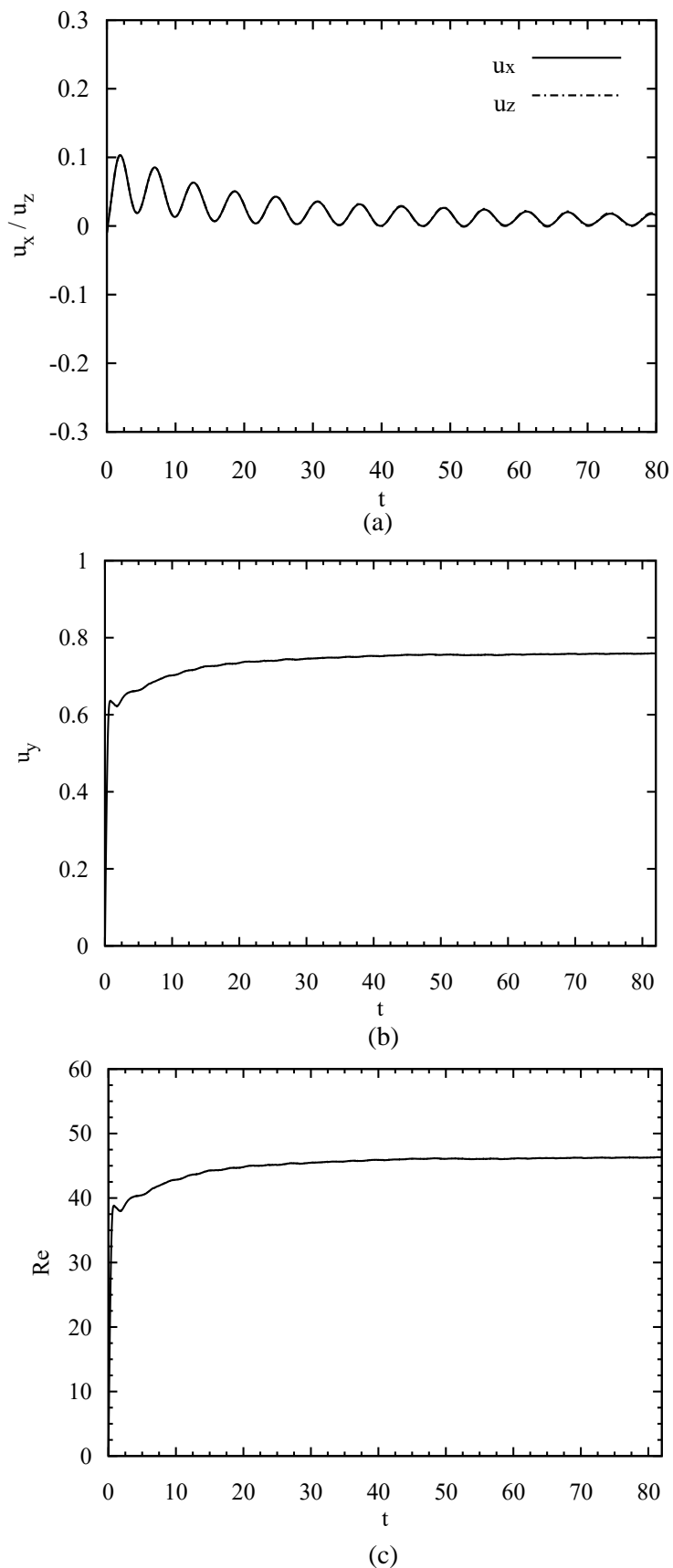
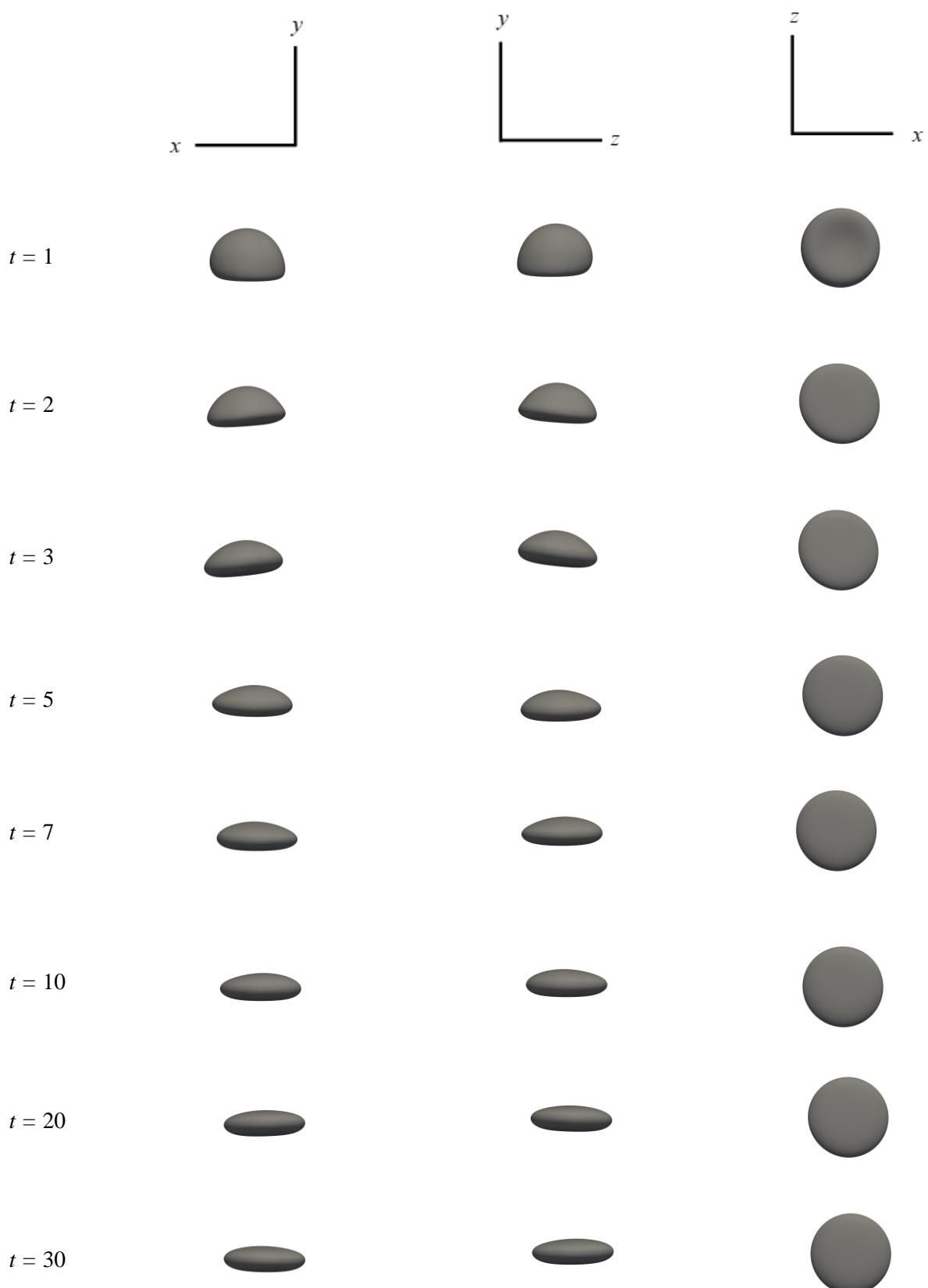


Figure 4.18: Time histories of (a) x- component and z- component of velocity (b) y- component of velocity (c) Reynolds number.

**Bubble Shapes:**



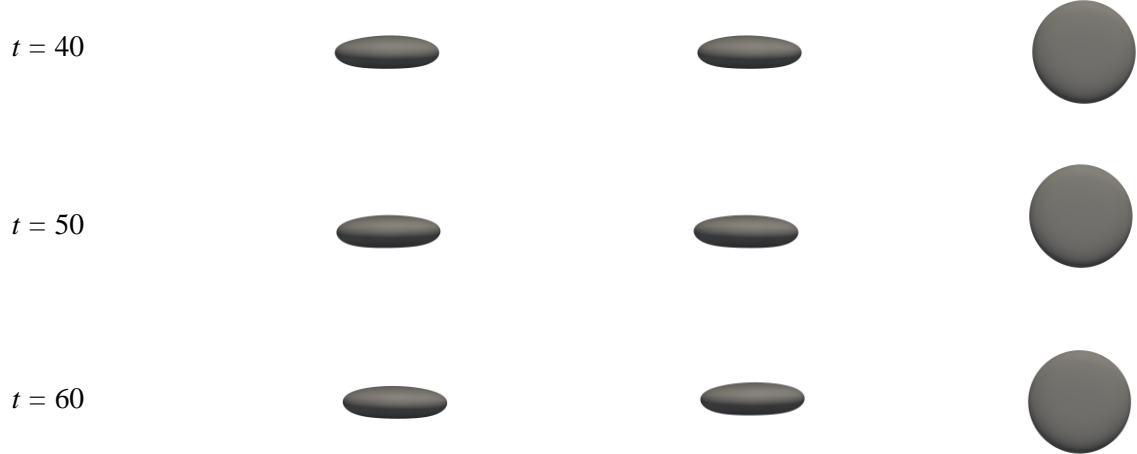
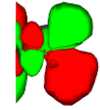
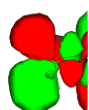


Figure 4.19: Spatio-temporal variation of bubble shape in rear, left-side and bottom view (from left to right) at  $t = 1, 2, 3, 5, 7, 10, 20, 30, 40, 50, 60$ .

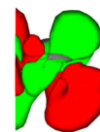
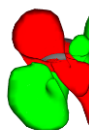
**Vorticity:**



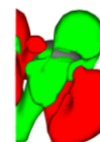
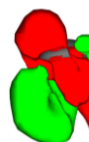
$t = 1$



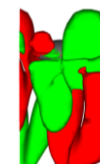
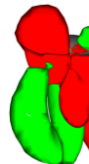
$t = 2$



$t = 3$



$t = 5$



$t = 7$



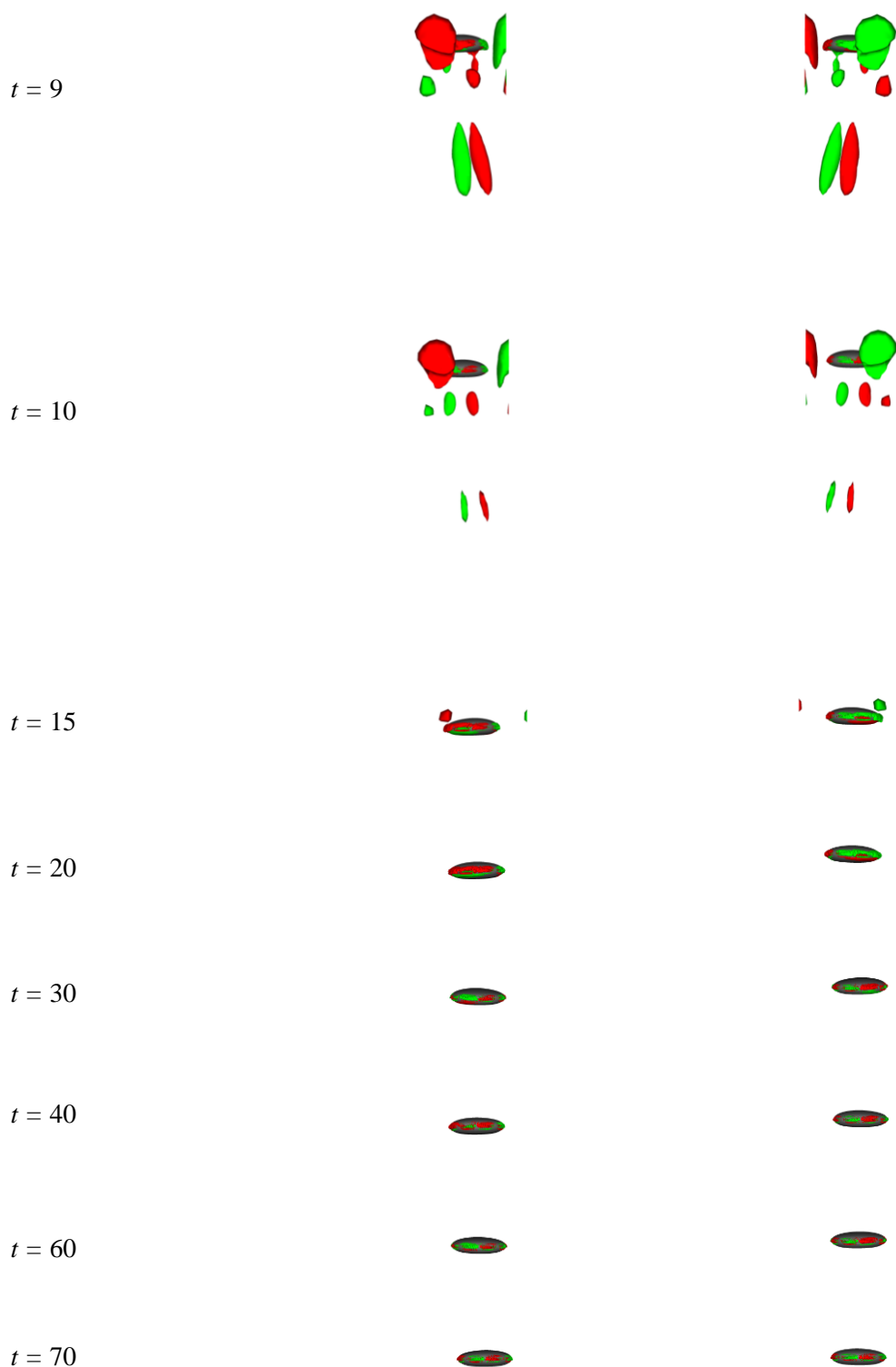


Figure 4.20: Rear (left) and left-side (right) view of iso-contours of spatio-temporal variation of streamwise vorticity  $\omega_y = \pm 0.15$  ( $\omega_y = +0.15$  for green and  $\omega_y = -0.15$  for red) at  $t = 1, 2, 3, 5, 7, 9, 10, 15, 20, 30, 40, 60, 70$ .

Again, from Figure 4.17 and Figure 4.18, it is understood that path instability hasn't yet fully developed because x- and z- component of velocities periodicity don't conform to a constant amplitude and as a result, the zigzagging motion is almost diminished after a certain point. As the amplitude of wall normal velocity components is maintaining a decreasing trend, it can be foreseen that it would die out as the computing time would be increased. As a result, the trajectory would conform to a curvilinear motion eventually. This is the most close-to-fully-developed case for path instability.

While the terminal bubble remains somewhat the same as the previous cases, the longer period of deformation is something to notice here (Figure 4.19). The vortices accumulated on mostly at the edge of bubble surface, that isn't enough to induce fully developed path instability (Figure 4.20). For the path instability to persist permanently, it is assumed that the vortices need to accumulate at the bottom surface of bubble as it would render the rising motion of bubble unstable as rear end wake does. But this sort of vortices is yet to form for the cases simulated so far.

## 4.6 Case-6 (Ga = 62)

**Trajectory:**

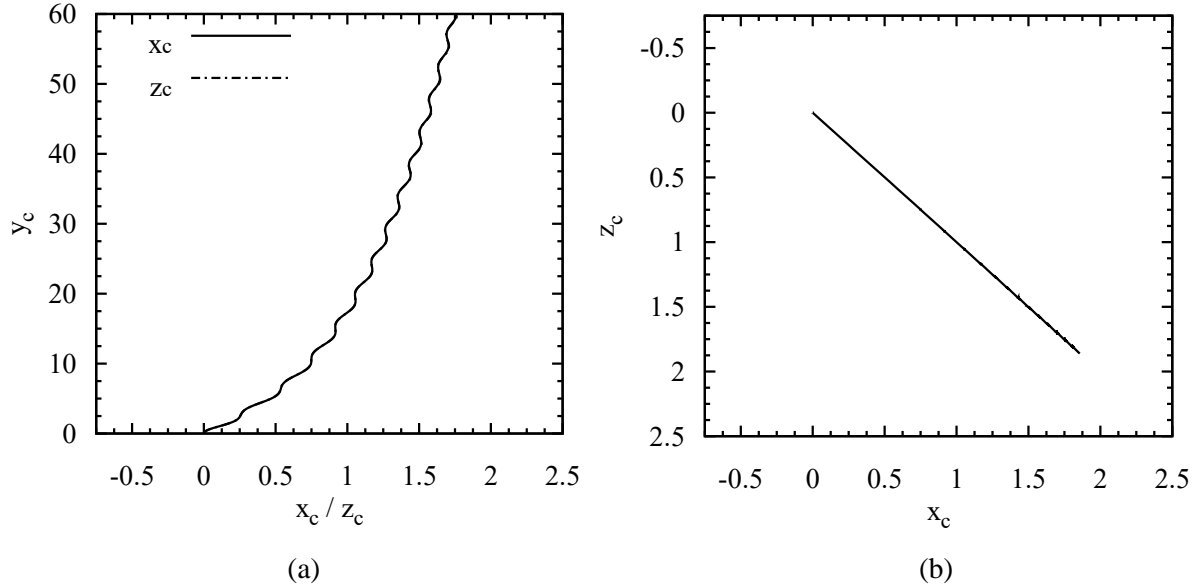


Figure 4.21: (a) Variation of  $x_c$  (front view of bubble trajectory) and  $z_c$  (side view of bubble trajectory) along  $y_c$  (b) Top view of bubble trajectory (c) Three-dimensional bubble trajectory.

**Time Histories:**

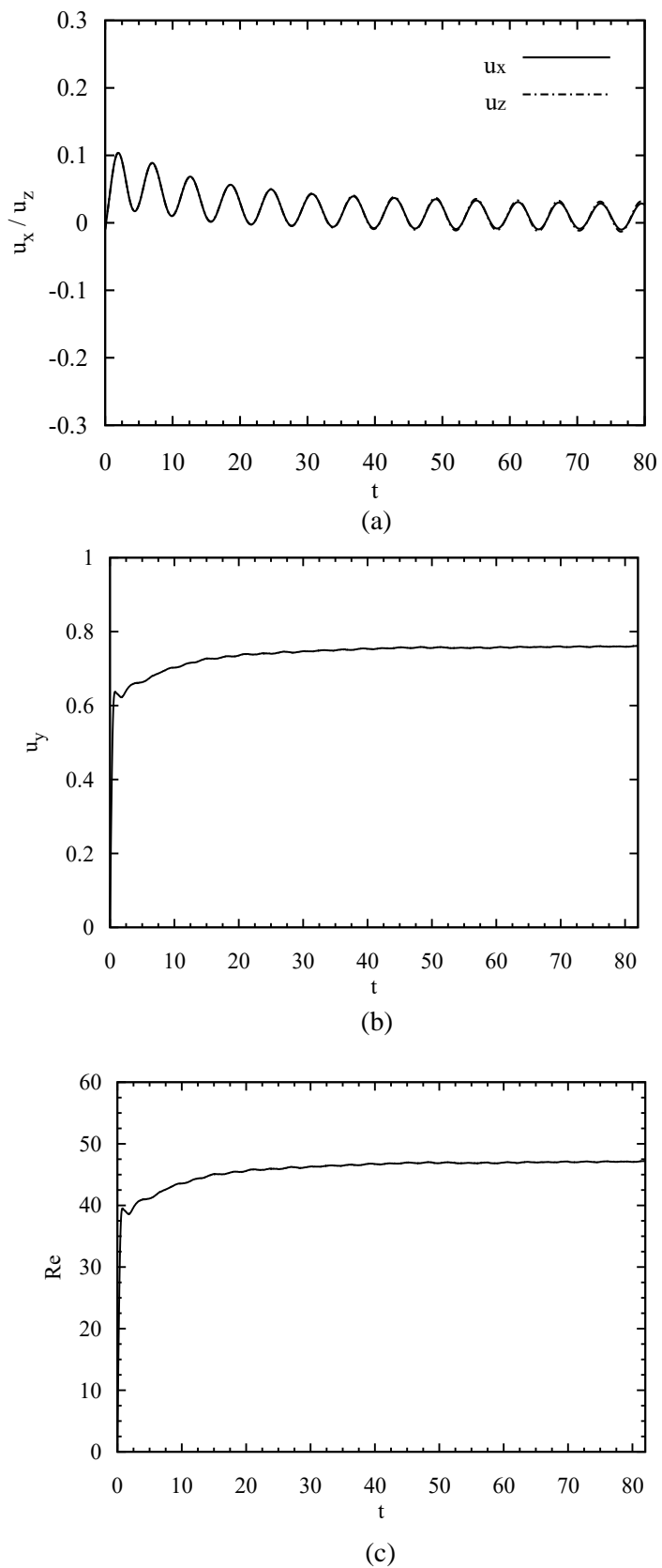
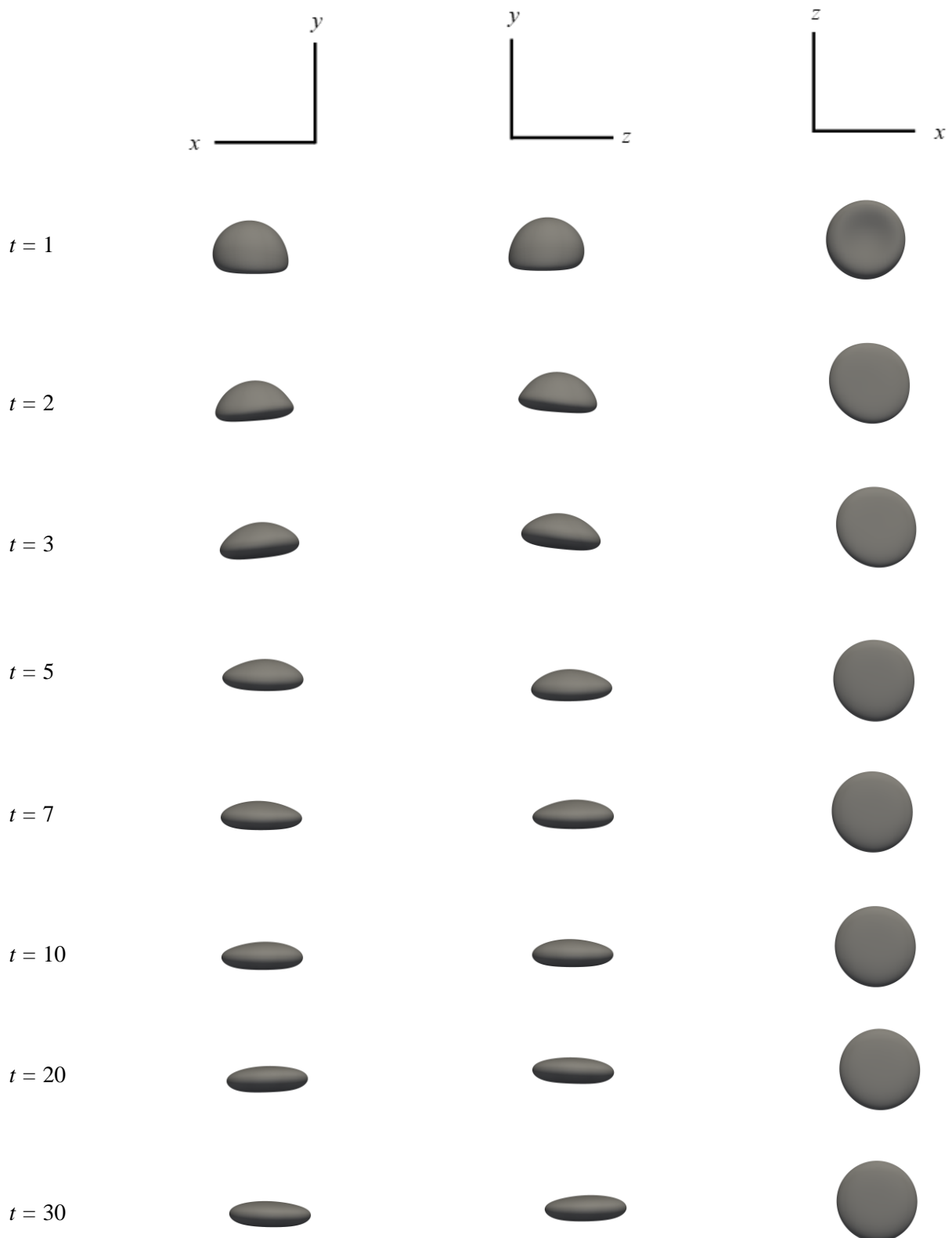


Figure 4.22: Time histories of (a) x- component and z- component of velocity (b) y- component of velocity (c) Reynolds number.

**Bubble Shapes:**



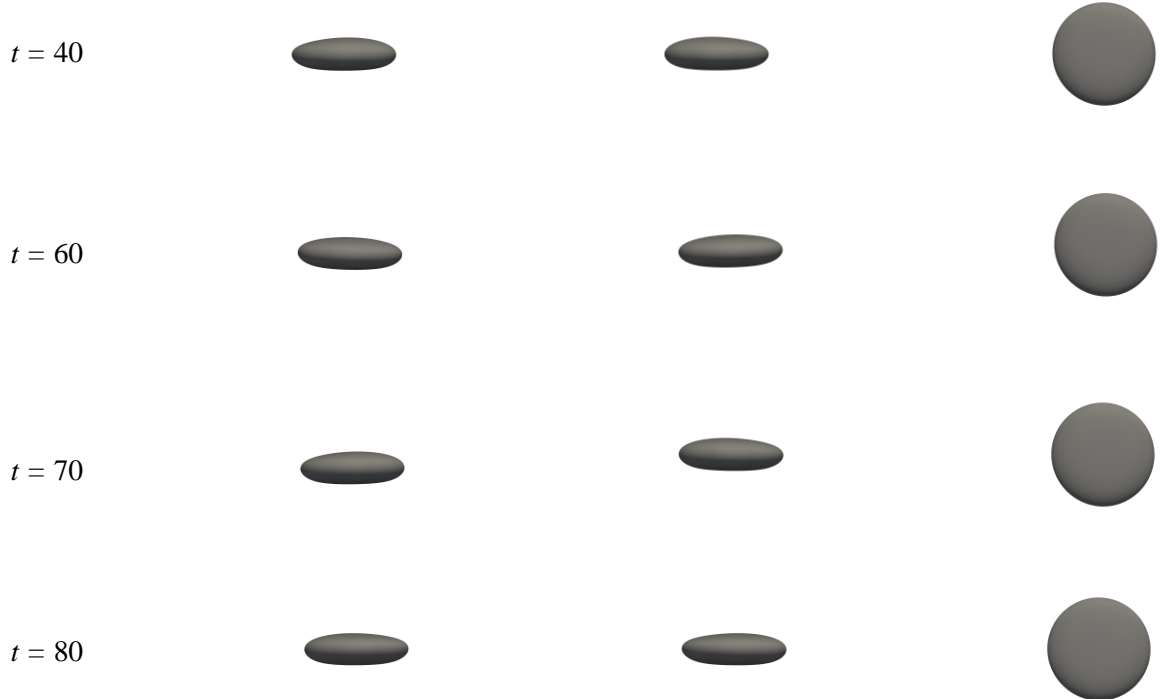


Figure 4.23: Spatio-temporal variation of bubble shape in rear, left-side and bottom view (from left to right) at  $t = 1, 2, 3, 5, 7, 10, 20, 30, 40, 60, 70, 80$ .

**Vorticity:**

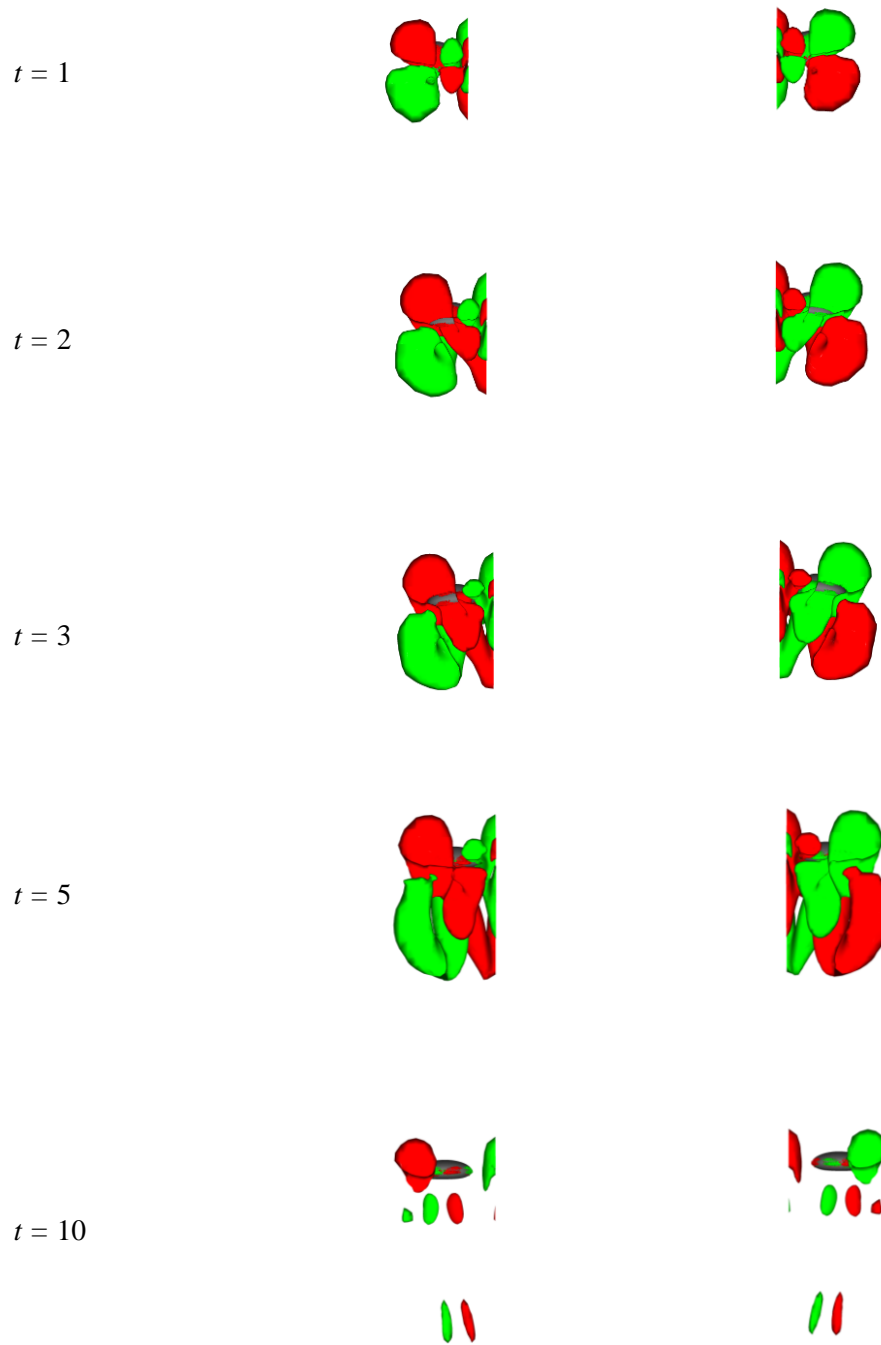




Figure 4.24: Rear (left) and left-side (right) view of iso-contours of spatio-temporal variation of streamwise vorticity  $\omega_y = \pm 0.15$  ( $\omega_y = +0.15$  for green and  $\omega_y = -0.15$  for red) at  $t = 1, 2, 3, 5, 10, 20, 30, 40, 60, 70$ .

In this case, the persistence of bubble path instability is exhibited for enough time to note that the bubble has shifted to fully developed oscillating regime. The bubble trajectory is planar zigzag in Figure 4.21a, 4.21b that is confined into a plane at  $45^\circ$  with the x-y plane. But there seems to be slight deviation from the confinement to a plane as can be seen towards the last portion of Figure 4.21b. This just might be a sign of induction of soon to be found spiraling motion for upcoming cases. As the bubble fully develops path instability in this case, corresponding Galilei number is identified as the *critical Ga* i.e. the value for Galilei number at which full transition from steady curvilinear regime to oscillating (zigzag) regime happens. Zhang et al. found the *critical Ga* to be around 60 for single vertical wall [24].

As the bubble shows zigzag trajectory, in other word, path instability, it is important to note that though the vorticity gets reduced on bubble progressively with increasing time in Figure 4.24, the accumulated wake over the bubble must exceed a critical value to induce permanent path instability to the bubble. At  $t = 60, 70$ , it's very noticeable that vortices accumulate at the bottom surface of bubble that was non-existent at the same timeline of case-5. So, as predicted earlier, the vortices at the bottom surface indeed acts as a major contributing factor at inducing fully developed path instability.

Further evidence of fully developed path instability can be understood from the conformation of constant amplitude in x- and z- component of velocity in Figure 4.22a. Rising velocity and Reynolds number also conform to a specific value after the establishment of path instability but before that there is short bumps that can be noticed in Figure 4.22b and 4.22c.

The terminal bubble shape remains the same as the previous ones that is the oblate ellipsoidal shape (Figure 4.23). This is to say, without sufficient wake developing at the rear side of the bubble, the terminal bubble shape doesn't seem to change.

The regime due to fully developed path instability is identified as *Oscillating* and the corresponding motion to be *zigzag*.

## 4.7 Case-7 (Ga = 63.36)

**Trajectory:**

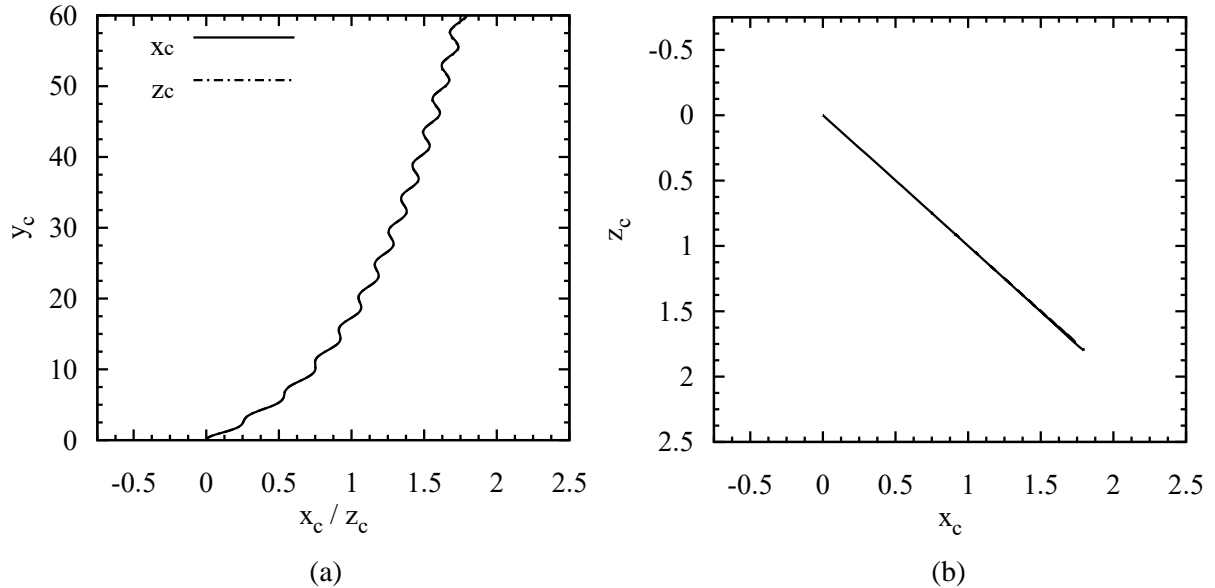


Figure 4.25: (a) Variation of  $x_c$  (front view of bubble trajectory) and  $z_c$  (side view of bubble trajectory) along  $y_c$  (b) Top view of bubble trajectory (c) Three-dimensional bubble trajectory.

**Time Histories:**

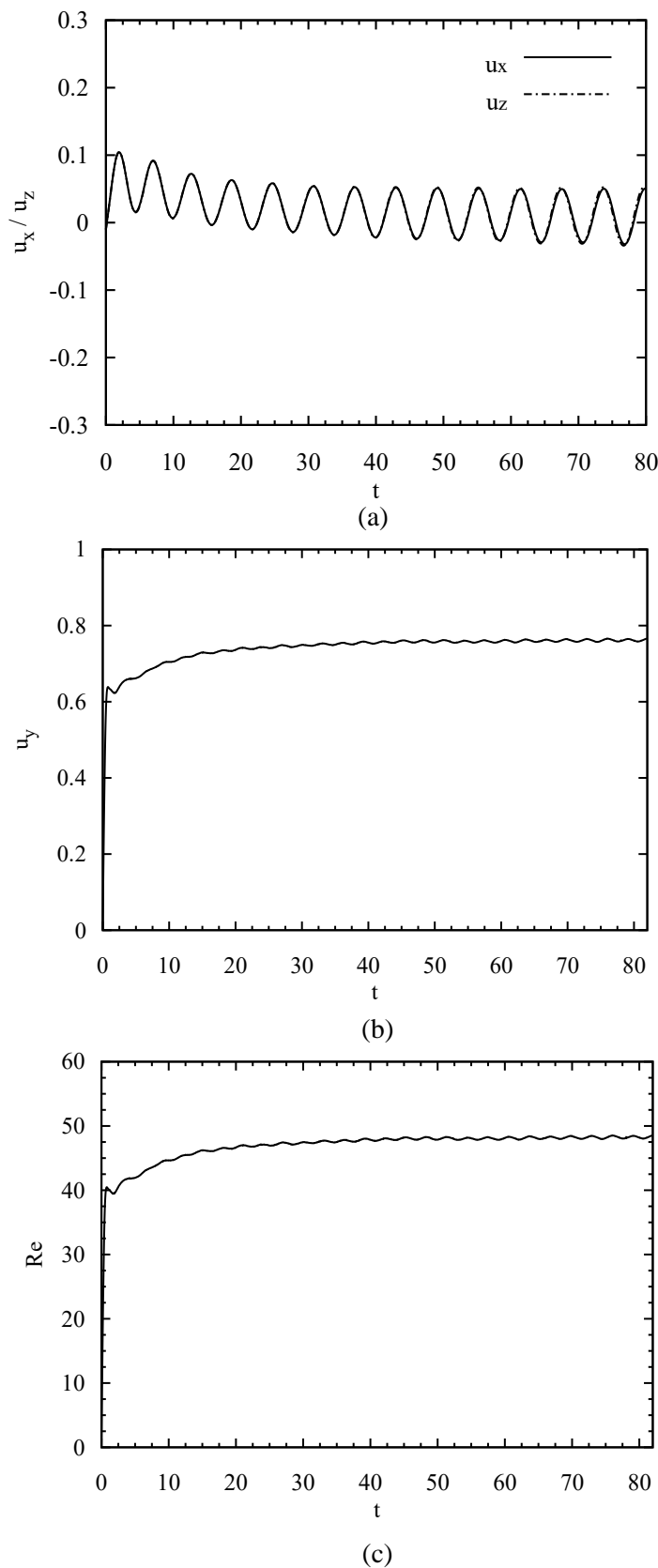
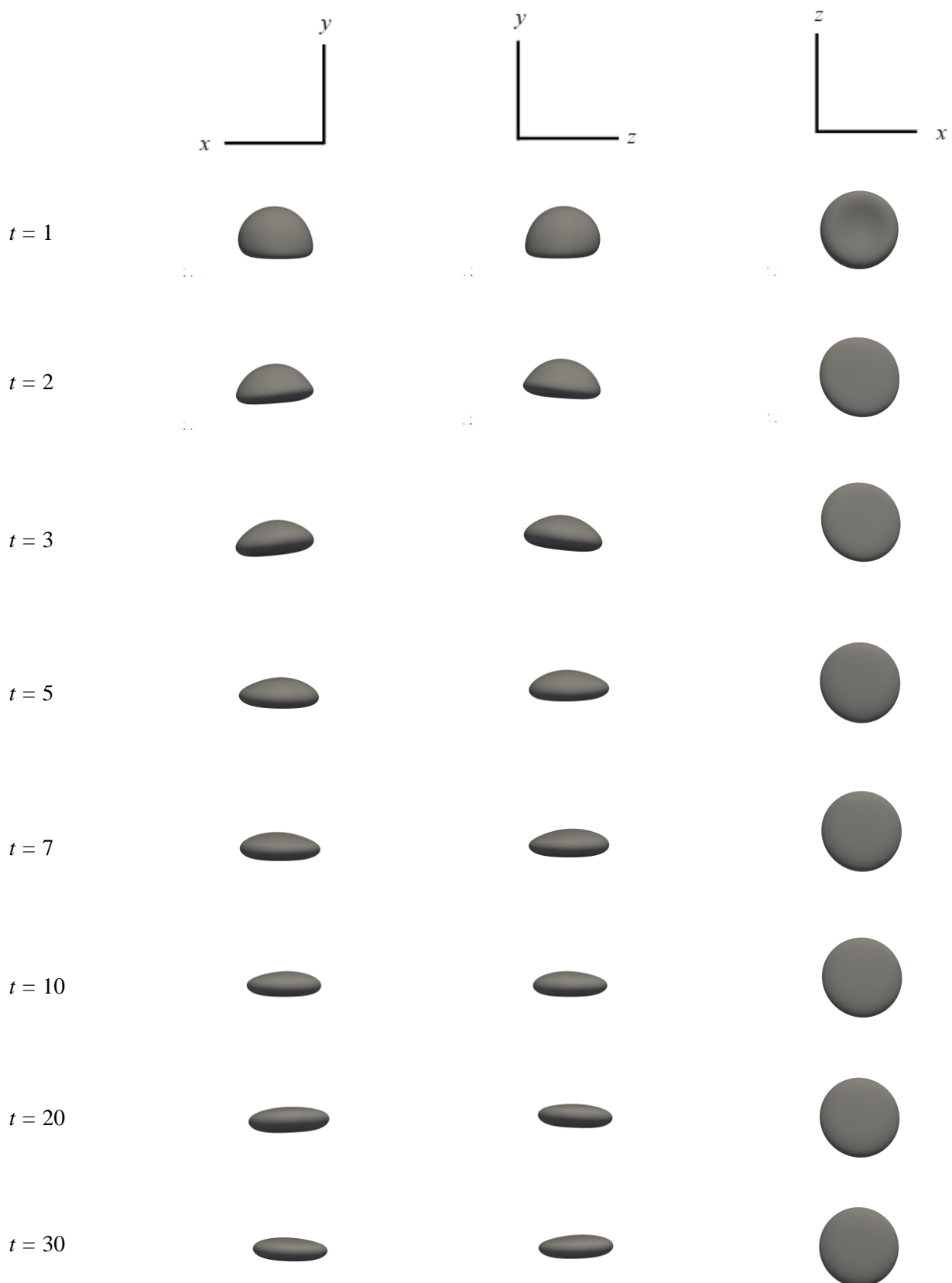


Figure 4.26: Time histories of (a) x- component and z- component of velocity (b) y- component of velocity (c) Reynolds number.

**Bubble Shapes:**



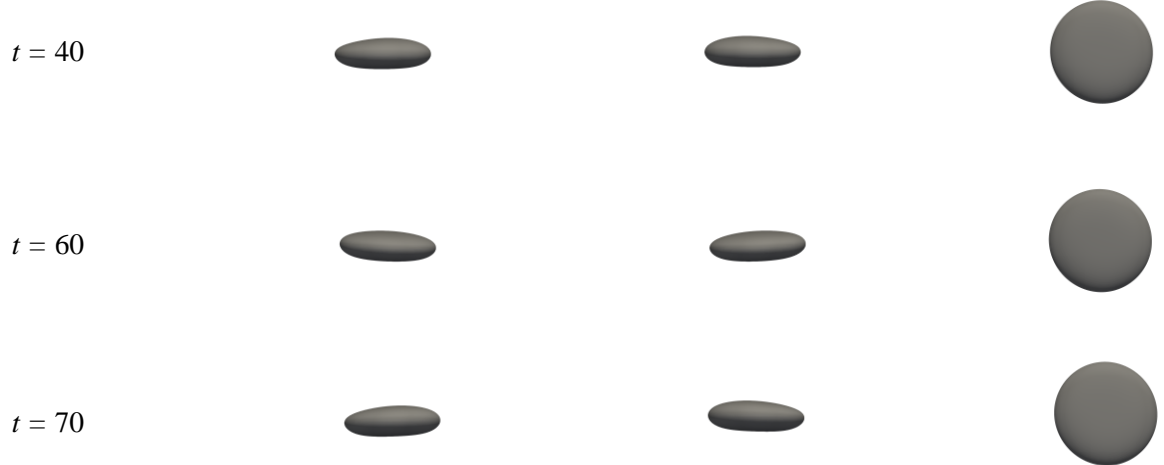
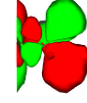
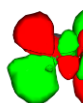


Figure 4.27: Spatio-temporal variation of bubble shape in rear, left-side and bottom view (from left to right) at  $t = 1, 2, 3, 5, 7, 10, 20, 30, 40, 60, 70$ .

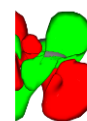
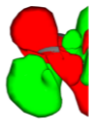
**Vorticity:**



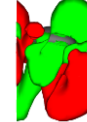
$t = 1$



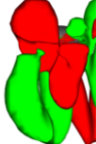
$t = 2$



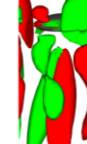
$t = 3$



$t = 5$



$t = 7$



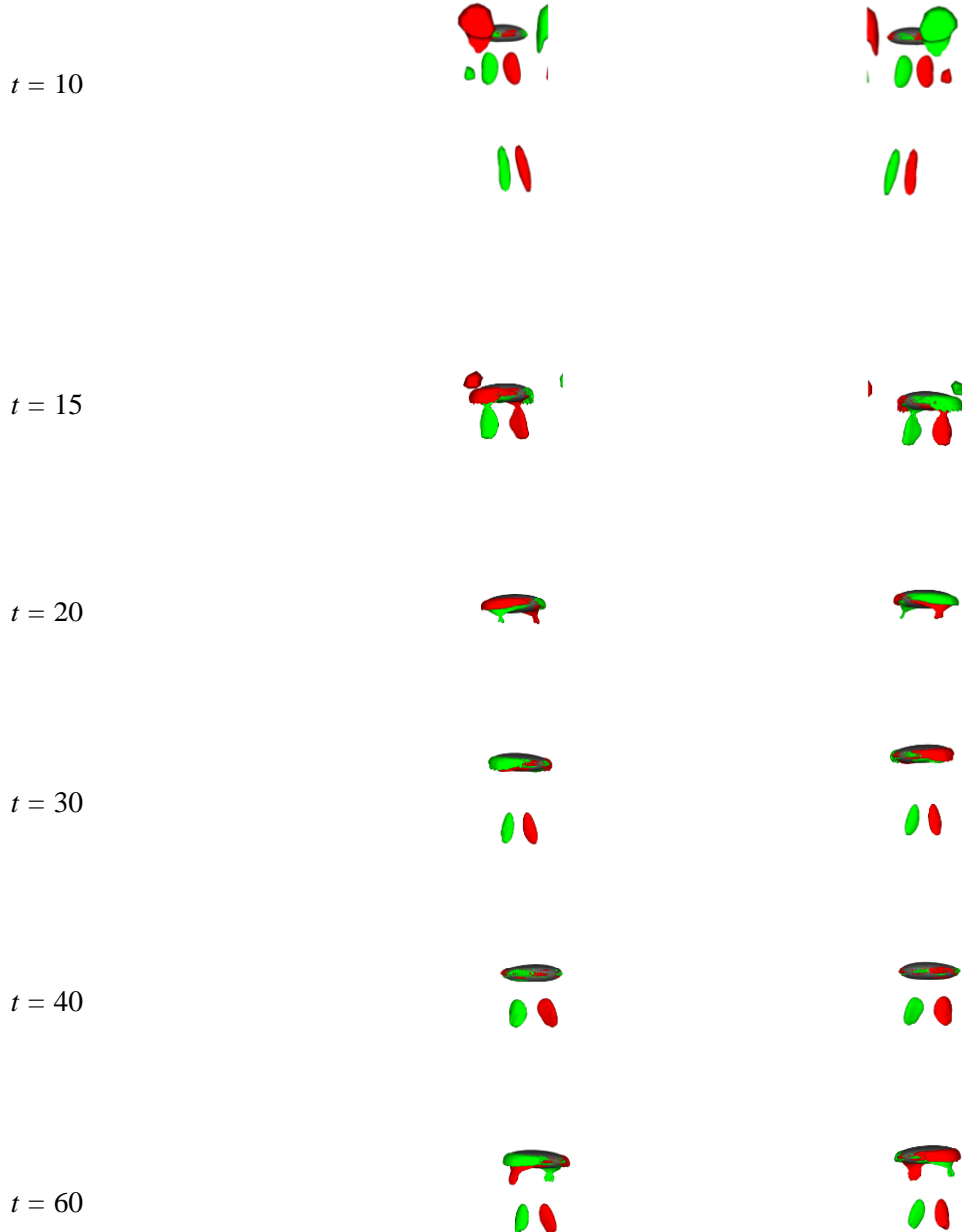


Figure 4.28: Rear (left) and left-side (right) view of iso-contours of spatio-temporal variation of streamwise vorticity  $\omega_y = \pm 0.15$  ( $\omega_y = +0.15$  for green and  $\omega_y = -0.15$  for red) at  $t = 1, 2, 3, 5, 7, 10, 15, 20, 30, 40, 60$ .

As can be seen from Figure 4.25, path instability is fully developed after an initial transient that affect bubble inertia in a permanent manner. It is to be noticed that around  $t = 70$  or so, bubble starts to develop a spiral motion with the spirals being quite small. As the spiral is in development stage rising velocity take up an oscillating trend (Figure 4.26b and 4.26c). It is assumed that with fully developed spiral motion, the rising velocity tends to conform to a specific value. The amplitude increases from previous case but shows a stabilized trend (Figure 4.26a).

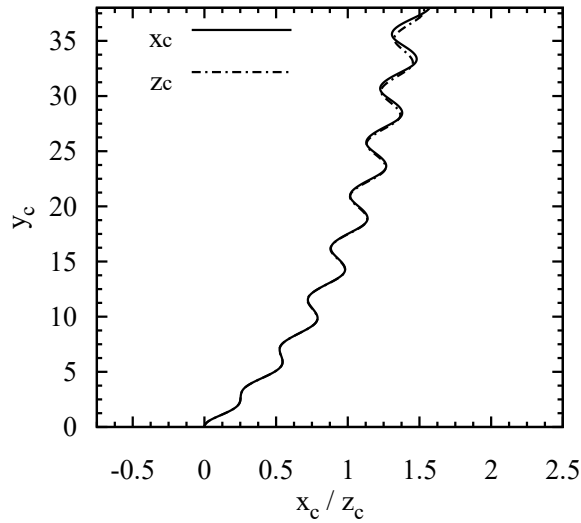
Though the terminal bubble shape still resembles that of oblate ellipsoidal, the deformation takes place for far too longer than other cases (Figure 4.27). The wake structure in Figure 4.28 starts to form at rear

side of bubble as it rises and it presumably plays a key role at developing spiraling motion of bubble from planar zigzag motion. It is to be noted that the wake structure that is developing doesn't retain symmetry. As a result, this could impart imbalanced repulsive force initially from the two walls.

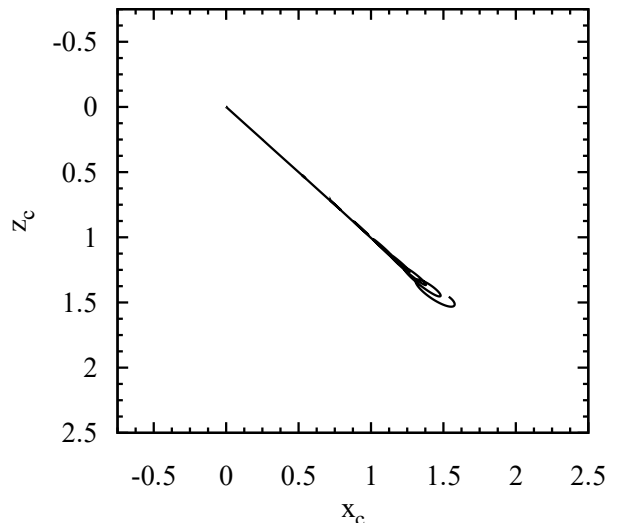
Though the trajectory is partly zigzag, partly developing-spiral, the regime is easily identified as *Oscillating*. However, the motion is transitional where zigzagging shifts to spiraling.

## 4.8 Case-8 (Ga = 70)

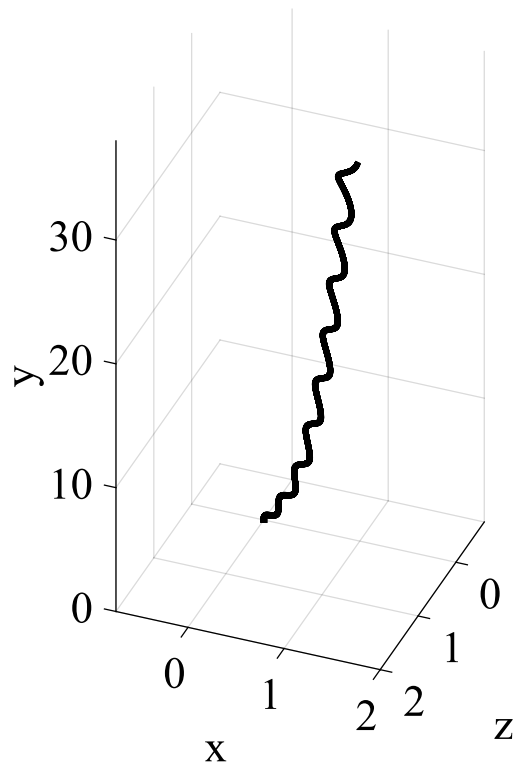
**Trajectory:**



(a)



(b)



(c)

Figure 4.29: (a) Variation of  $x_c$  (front view of bubble trajectory) and  $z_c$  (side view of bubble trajectory) along  $y_c$  (b) Top view of bubble trajectory (c) Three-dimensional bubble trajectory.

**Time Histories:**

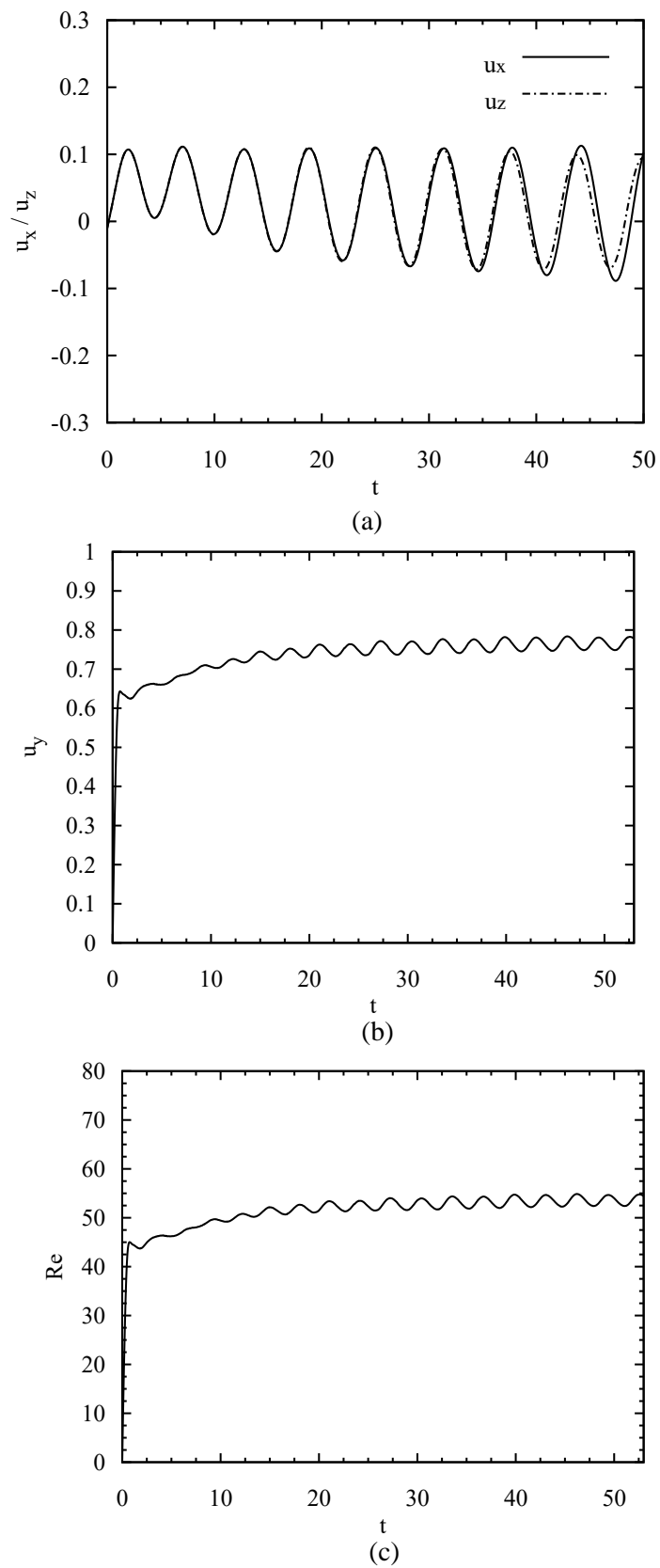
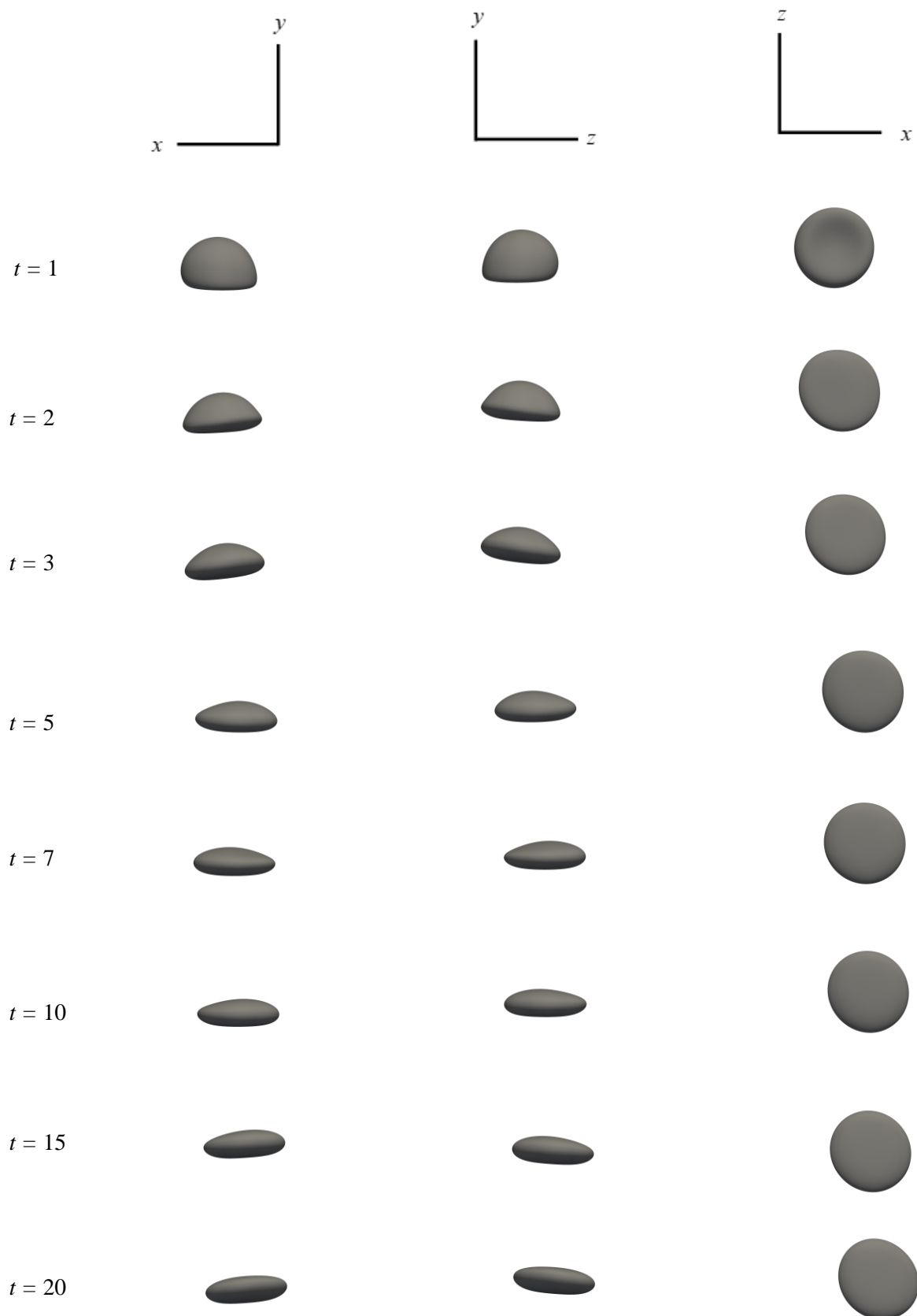


Figure 4.30: Time histories of (a) x- component and z- component of velocity (b) y- component of velocity (c) Reynolds number.

**Bubble Shapes:**



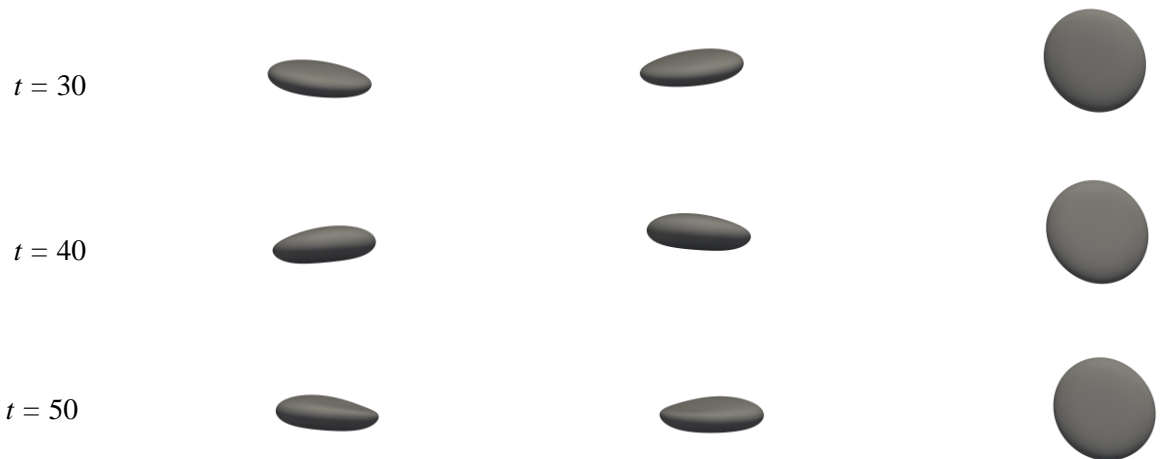
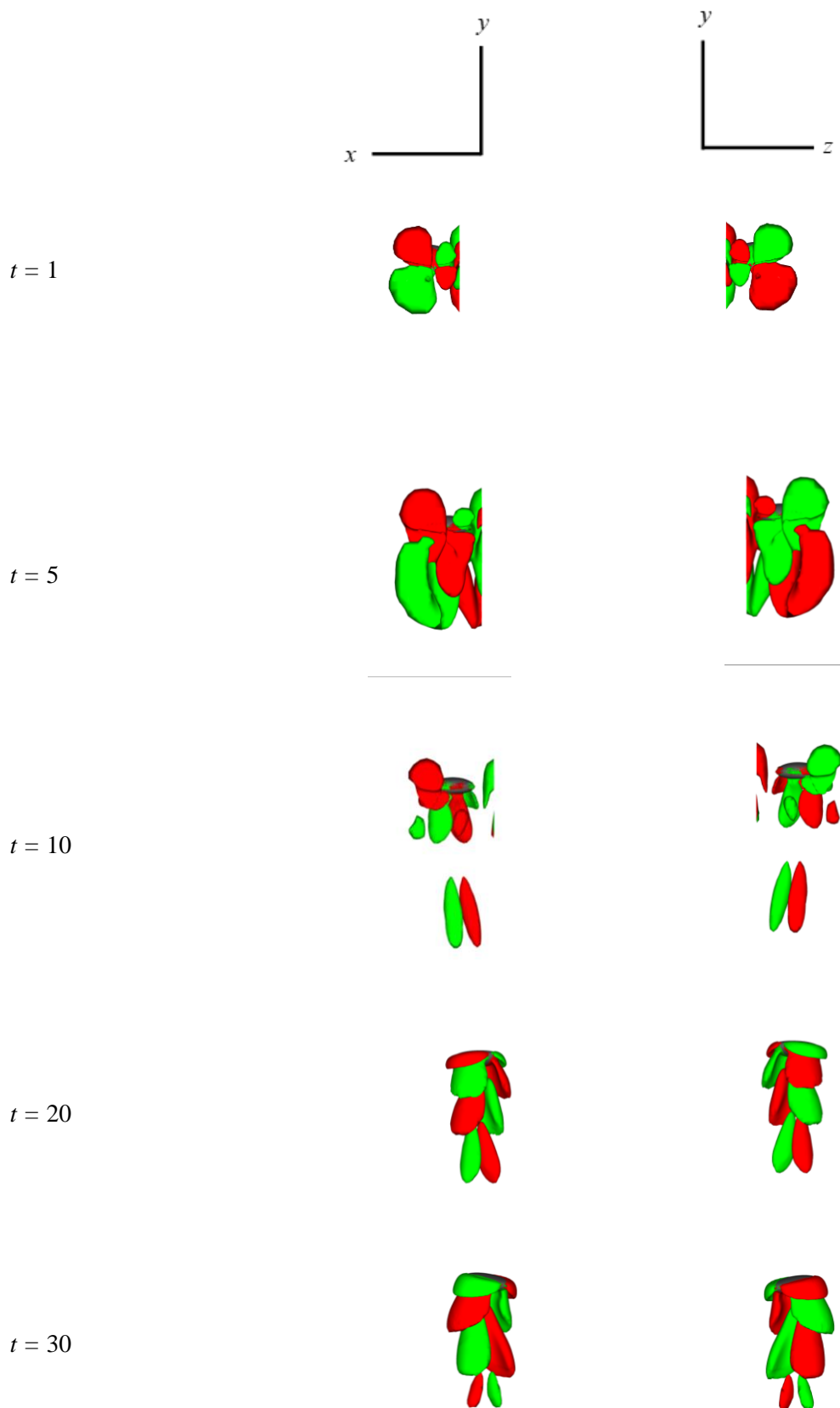


Figure 4.31: Spatio-temporal variation of bubble shape in rear, left-side and bottom view (from left to right) at  $t = 1, 2, 3, 5, 10, 15, 20, 30, 40, 50$ .

**Vorticity:**



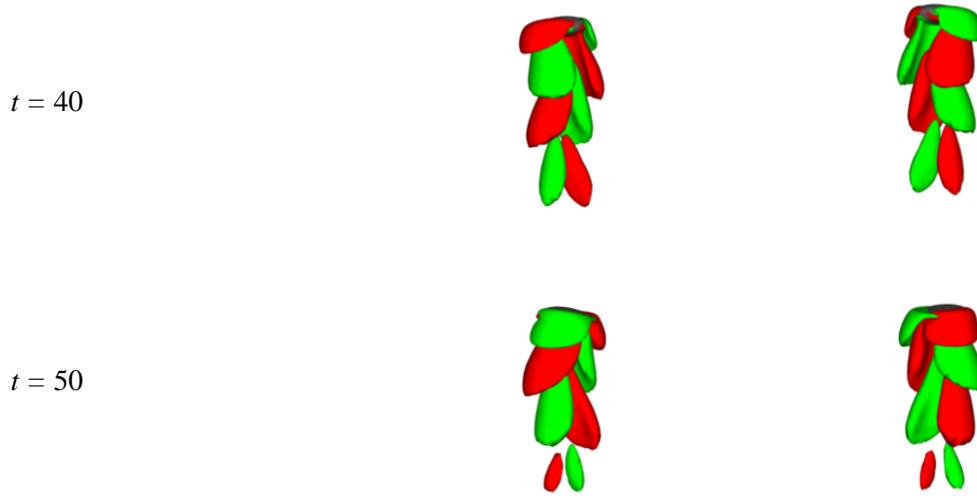


Figure 4.32: Rear (left) and left-side (right) view of iso-contours of spatio-temporal variation of streamwise vorticity  $\omega_y = \pm 0.15$  ( $\omega_y = +0.15$  for green and  $\omega_y = -0.15$  for red) at  $t = 1, 5, 10, 20, 30, 40, 50$ .

Bubble starts to shift to fully developed spiral sub-regime as the Galilei number is increased to 70. Bubble doesn't confine itself into a particular plane rather starts giving spiraling motion (Figure 4.29) from around  $t = 25$ . Once established, this phenomenon is going to persist as long as the simulation will be run. The key here is, however, how much time it takes till the establishment of fully developed spiraling motion. Hence, this Galilei number can be labelled as a point for the transition from the planar zigzag to spiraling trajectory. Though it is not with certainty that we can tell that this is the critical value of Galilei number for bubble to transition from zigzag to spiraling motion, but we suspect that the value is very close to 70 but albeit not greater than it because the wake structure is fully developed at the rear end of bubble as can be seen from Figure 4.32.

It can be seen from Fig 4.30a that the wall normal velocity components rise with greater amplitude as the spiraling sub-regime is gradually established. One thing to note here that, the value of both wall normal velocity components as well as phases start to differ with the introduction of spiral showing greater effect of left-side wall than rear wall. It is also noticed in Fig 4.29a where the front view and side view of bubble trajectory start to differ. This situation might rise from the structure of the wake developed behind the bubble which looks like two counter-rotating vortices (Figure 4.32) that doesn't exhibit a symmetry plane from either of front or side view. Because of the asymmetrical construction of the oppositely signed vortices, the bubble wall-normal velocity components might be affected showing an asymmetrical behavior themselves that was absent in previous cases both for curvilinear and zigzag motion. It is suspected that the asymmetry of vortices generated is influenced by the two walls as the bubble moves in a diagonal manner in three-dimensional space, hence the path instability starts operating at spiraling sub-regime after a point of time.

The bubble shapes show asymmetric deformation from the point spiraling is introduced as can be understood by asymmetric bottom view shown in Fig. 4.31. The rear and left-side view also bear the testimony of it. For previous cases, the deformation of bubble was somewhat symmetrical. But here, though the initial deformation looks a lot like the previous cases, the later temporal behavior shows that it deviates from its symmetric deforming shape to unsteady asymmetric one.

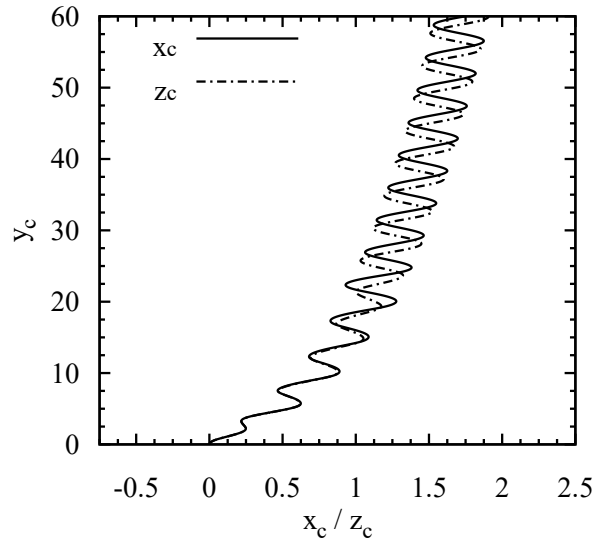
The bubble terminal velocity is not achieved during the span of simulation time. However, it is believed that after the spiral sub-regime is fully established at higher times, the bubble will conform to a specific terminal velocity. But if the spiral of spiraling keeps getting bigger at higher time, it is unlikely that the

bubble will conform to a specific terminal velocity. So, the constant radius of spiral is key to establish terminal velocity as that would suggest the full development of spiraling motion.

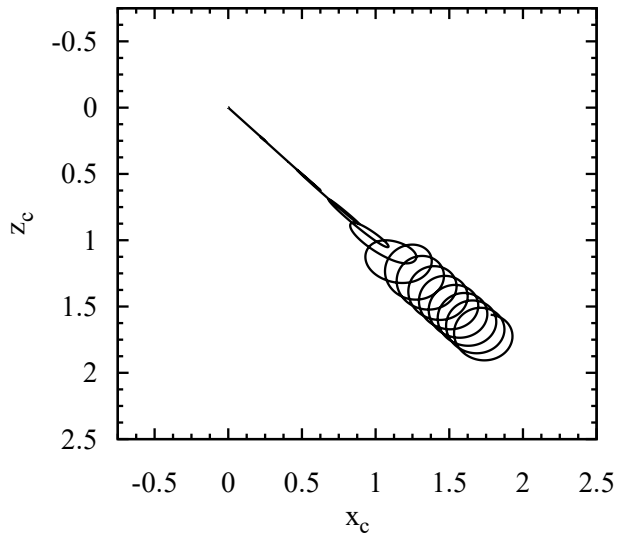
Despite all these transitional behaviors shown by the bubble, the regime for this case is, of course, identified as *Oscillating*.

## 4.9 Case-9 ( $Ga = 90.51$ )

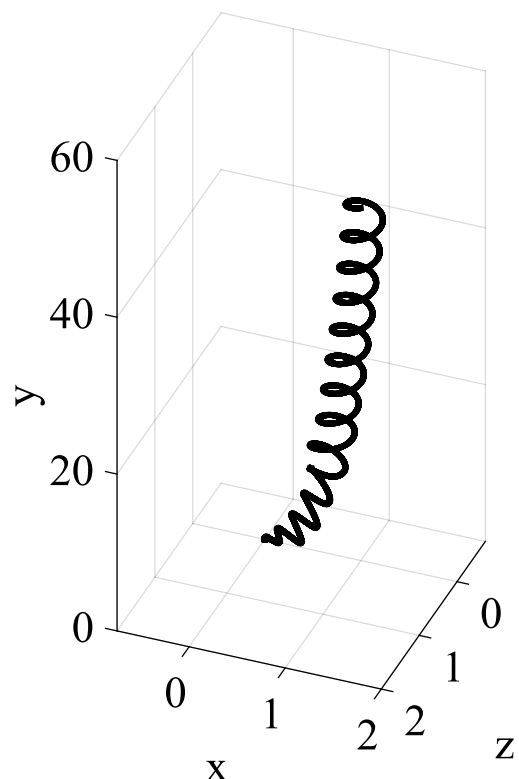
**Trajectory:**



(a)



(b)



(c)

Figure 4.33: (a) Variation of  $x_c$  (front view of bubble trajectory) and  $z_c$  (side view of bubble trajectory) along  $y_c$  (b) Top view of bubble trajectory (c) Three-dimensional bubble trajectory.

**Time Histories:**

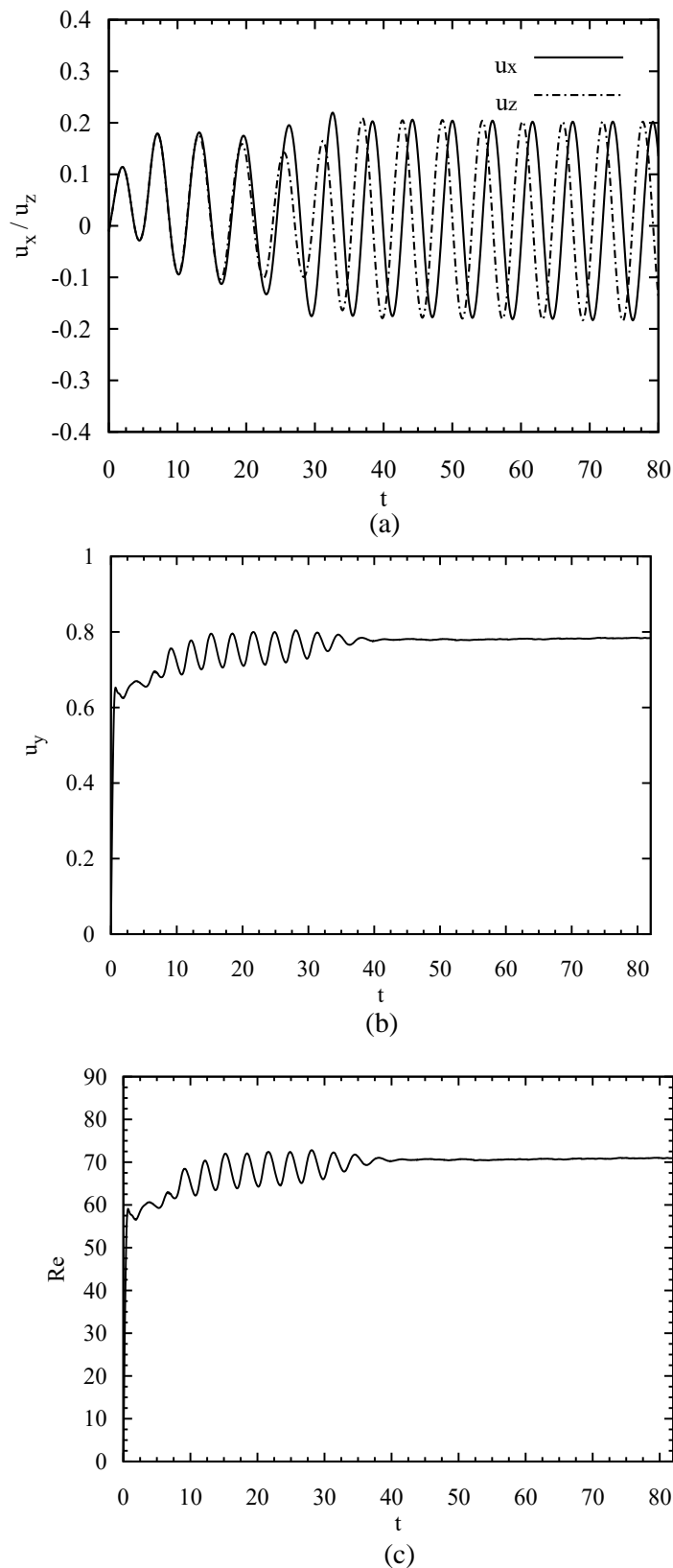


Figure 4.34: Time histories of (a) x- component and z- component of velocity (b) y- component of velocity (c) Reynolds number.

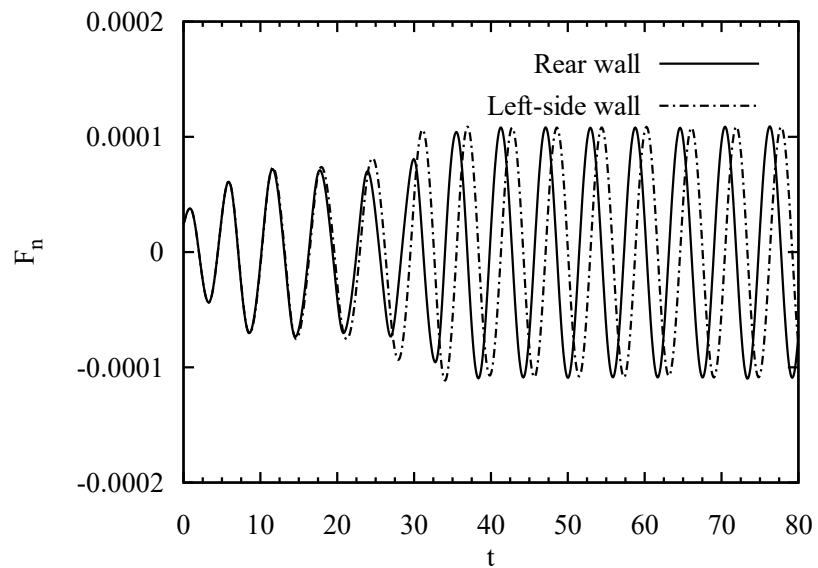
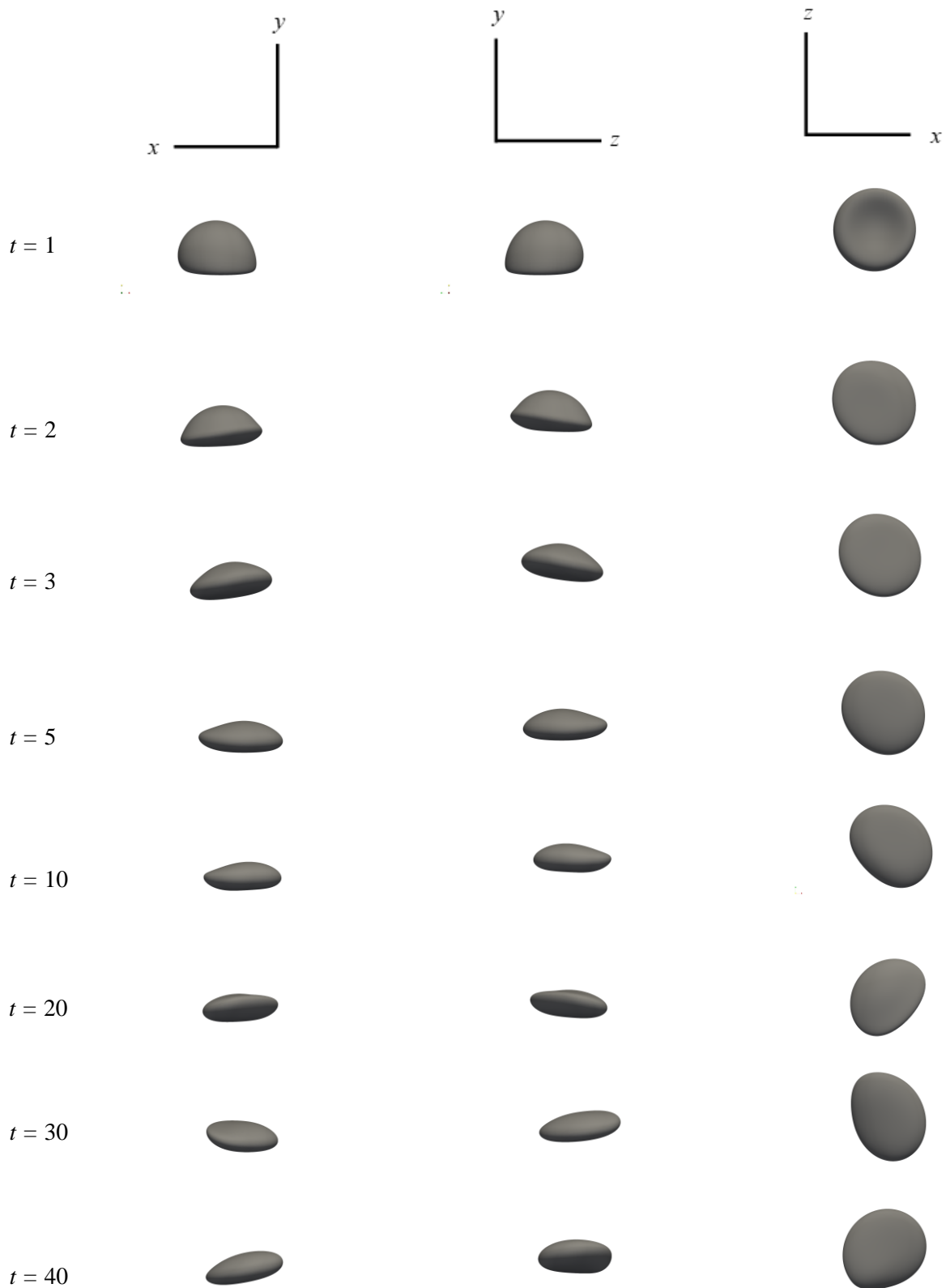


Figure 4.35: Time histories of the dimensionless force in the wall-normal direction

**Bubble Shapes:**



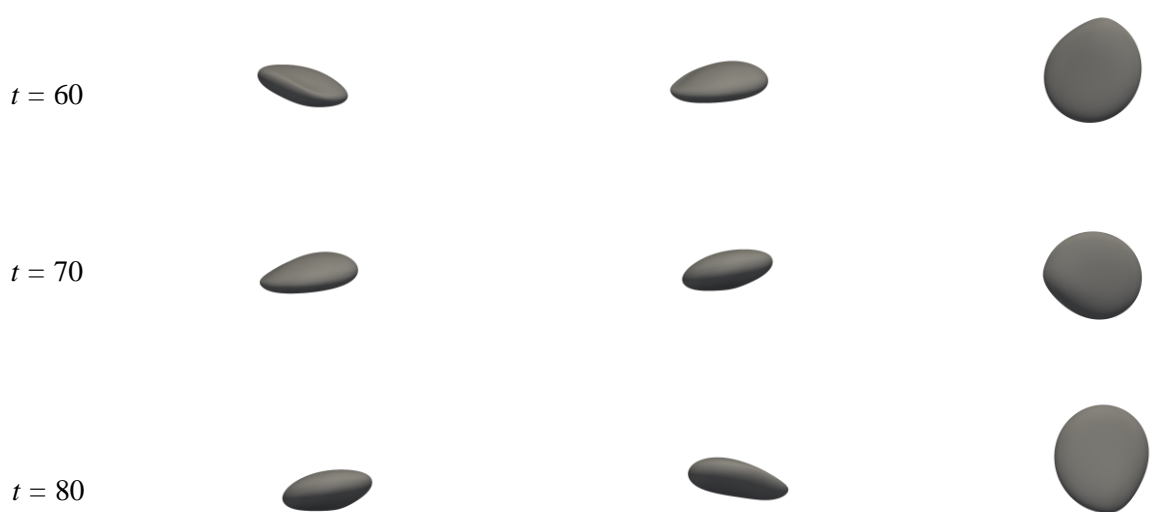
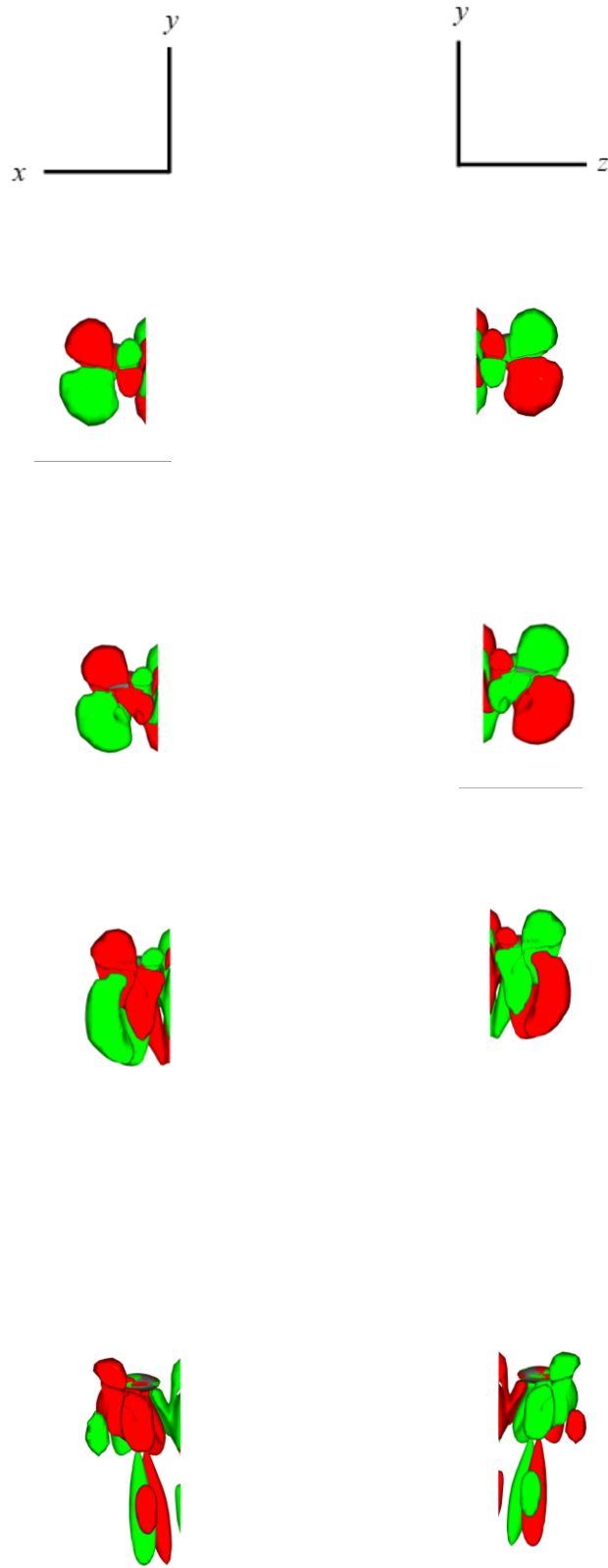


Figure 4.36: Spatio-temporal variation of bubble shape in rear, left-side and bottom view (from left to right) at  $t = 1, 2, 3, 5, 10, 20, 30, 40, 60, 70, 80$ .

**Vorticity:**



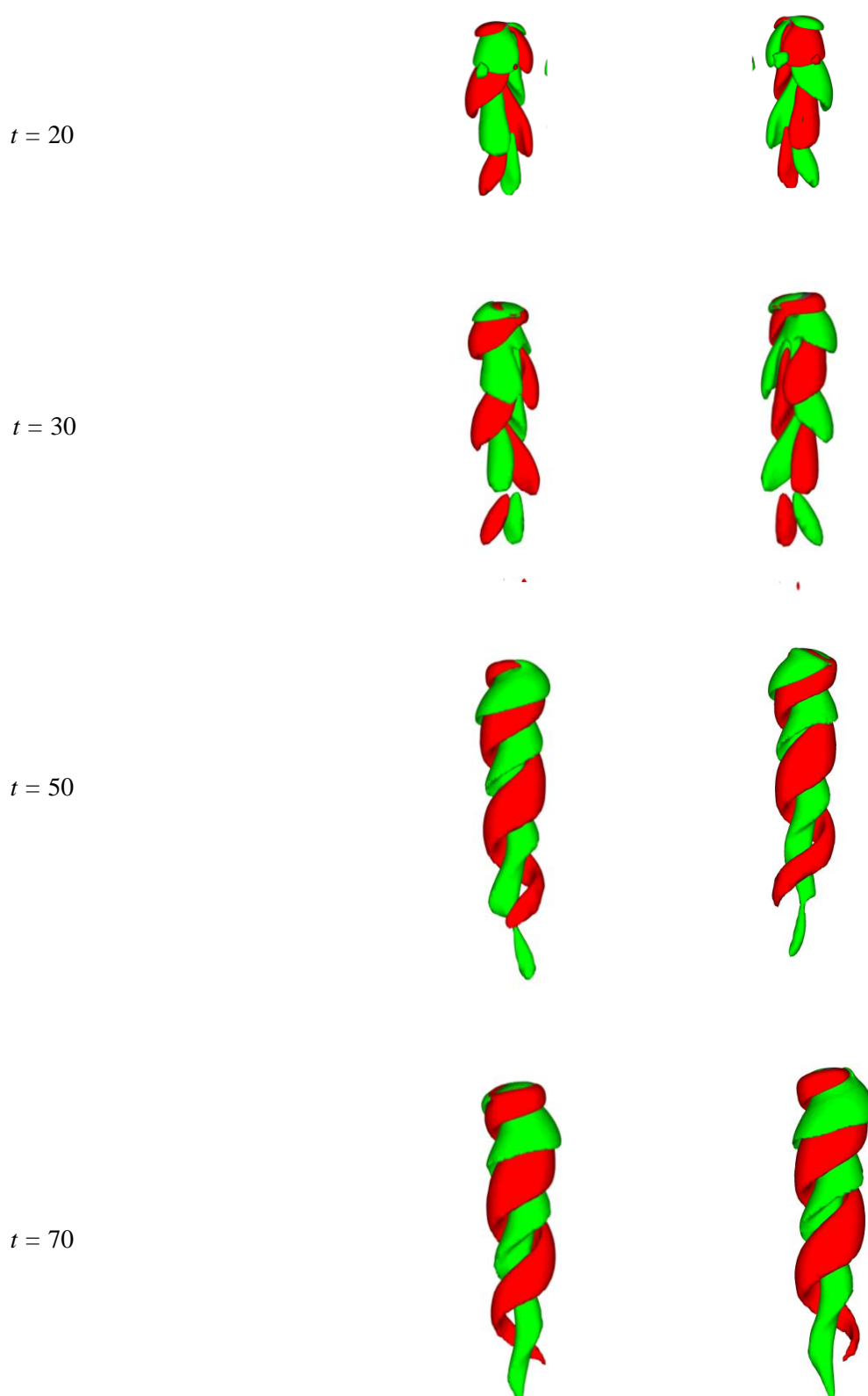


Figure 4.37: Rear (left) and left-side (right) view of iso-contours of spatio-temporal variation of streamwise vorticity  $\omega_y = \pm 0.15$  ( $\omega_y = +0.15$  for green and  $\omega_y = -0.15$  for red) at  $t = 1, 2, 5, 10, 20, 30, 50, 70$ .

This case corresponds to the spiraling sub-regime of oscillating regime. The behaviors shown by the bubble here is an extension of the behaviors shown at case-8. It is found that terminal velocity and Reynolds number in Figure 4.34b and 4.34c respectively indeed conform to a particular value when the spiral becomes consistently repetitive of same radius as suspected in case-8. The vortices produced, though counter-rotating, they are interwind with each other (Figure 4.37) as the steadiness of spiral motion is achieved (Figure 4.33). But initially it exhibits similar pattern like found in case-8 as the spiraling motion was still in-development stage.

Figure 4.35 shows the wall-normal dimensionless force which is significant for this case to have different phase and magnitude for rear and left-side wall in earlier stages when the wall effect is supposed to be maximum because of the minimum distance between bubble and walls. This is, again, can be attributed to asymmetrical vorticity generated because of two-wall interaction. In later stages, when the bubble inertia is predominant and wall-bubble distance is larger, the forces of both walls become equal in magnitude but phase differences persist permanently.

Bubble deformation exhibits the characteristics of the deformation found out for case-8 that is unsteady, asymmetric deformation. However, it is to be noted that the degree of deformation is greater in this case as the formation of spiraling motion is achieved quite early than previous case. Also, the constant deformation of bubble shape as observed in Figure 4.36 attributes to the fact that there isn't really a terminal shape for fully developed spiraling motion despite achieving a terminal rising velocity. The regime, however, is very easy to identify as *Oscillating* and the bubble motion is established as *spiraling*.

From Figure 4.38, it can be seen that terminal frequencies in both wall-normal direction doesn't vary with increasing Galilei number once oscillating regime is established while terminal amplitudes at both wall-normal direction varies even after the oscillating regime is established. But it is to be noted that the terminal frequencies and amplitudes don't show up before the establishment of oscillating regime.

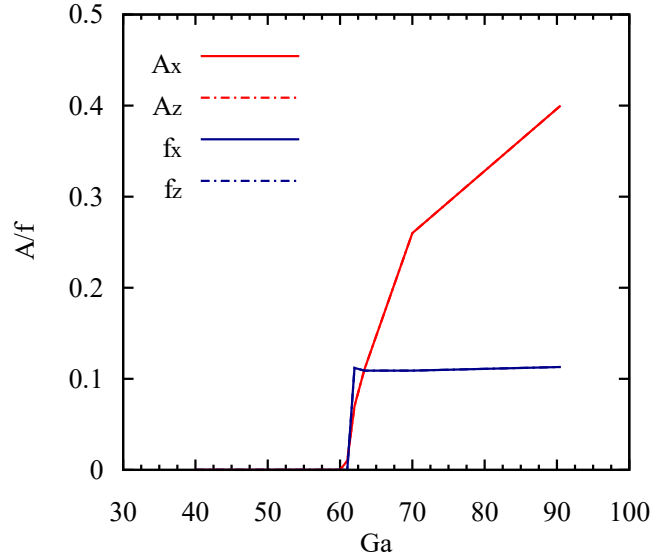


Figure 4.38: The effect of Galilei number on amplitude and frequency of the lateral (wall-normal direction) oscillation with presence of two walls.

The simulated cases are divided in different regimes against varying Galilei number. Only case-1 ( $Ga = 40$ ) turns out to be in *Steady* regime while case-2 ( $Ga = 55$ ), case-3 ( $Ga = 57$ ), case-4 ( $Ga = 60$ ) and case-5 ( $Ga = 61$ ) are in *Transition* regime. Other cases viz. case-6 ( $Ga = 62$ ), case-7 ( $Ga = 63.36$ ), case-8 ( $Ga = 70$ ) and case-9 ( $Ga = 90.51$ ) fall into *Oscillating* regime.

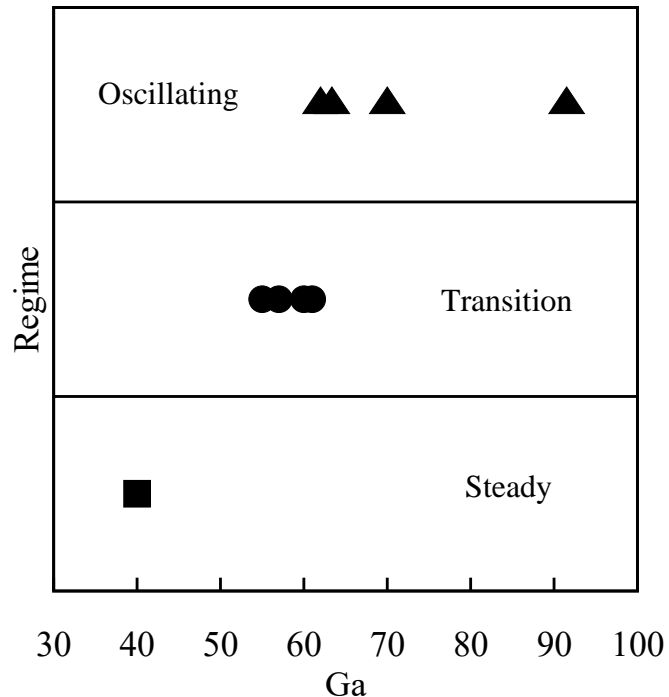


Figure 4.39: Distinct regimes obtained from present study

So, identified bubble regimes and the corresponding trajectories are shown below:

Table 4.2: Identified regimes and corresponding trajectories

Case No.	Regime	Trajectory
1	Steady	Curvilinear
2	Transition	Curvilinear to Zigzag
3	Transition	Curvilinear to Zigzag
4	Transition	Curvilinear to Zigzag
5	Transition	Curvilinear to Zigzag
6	Oscillating	Zigzag
7	Oscillating	Zigzag to Spiral
8	Oscillating	Spiral
9	Oscillating	Spiral

# CHAPTER 5

## CONCLUSIONS

Three dimensional dynamics of a single bubble rising near two vertical walls has been studied using fully three-dimensional numerical simulation. The regimes of bubble path have been presented for a range of Galilei number keeping other three conditional parameters constant. It is found that there are three distinct regimes (viz. Steady, Transition, Oscillating). The steady regime is distinct by the non-oscillatory trajectory of bubble and the steadiness of the velocity components. Also, it is noted that apart from initial phases, there is no vorticity generated as the bubble rises progressively. The vorticity generation happened during the initial phases was because of bubble-walls interaction. As the Galilei number was increased, bubble started having oscillatory trajectory but the oscillation doesn't persist and dies out eventually. This regime is defined as transition as bubble started shifting towards underdeveloped path instability. At  $Ga = 62$ , bubble shows fully developed oscillatory trajectory as the initial instability because of the conditional parameters coupled with the bubble-walls interaction persists. It is noted that the critical Galilei number (i.e. the point when fully developed path instability occurs) is less than that of unbounded condition ( $Ga = 70$ ) as pointed out by Zhang et al. [24]. As the Galilei number is further increased bubble trajectory shifts from zigzag to spiral motion. It is believed the fully developed motion occurs around  $Ga = 70$  though the transition from zigzag to spiral trajectory starts around  $Ga = 63$ . We observed that the amplitude of oscillation increased with increasing Galilei number as bubble transforms from zigzag to spiral sub-regime.

Spatio-temporal variation of bubble shapes and vorticity was studied too where it was noticed that there is a connection between vortices generated and other three bubble behavioral phenomena. Initial vorticity because of bubble-walls interaction rendered the bubble to migrate diagonally away from both the walls but when it moved substantially away from walls, the vorticity doesn't appear behind bubble as it rises for steady and transition regimes. However, wake accumulated on bubble has an influence on the so-called path instability. If the accumulated wake is greater than some critical value for a certain period, the bubble shows oscillatory behavior both in trajectory and velocity for that particular period. If vortices start to accumulate at the bottom surface as well, fully developed path instability occurs. With increasing vortex shedding, path instability intensifies and zigzag motion transforms into spiraling motion. It was noted that for spiral sub-regime, the wake structure takes corkscrew-like shape while counter-rotating against each other. So, streamwise vorticity is found to be the cause coupled with the bubble-walls interaction that influences the other bubble behavioral phenomena viz. path, shape, velocity.

# Recommendations

Future works extending the present study have a great prospect due to the advancement of numerical techniques developed along with the higher computing speed. Though this thesis has carried out the work to study two-wall effect on bubble dynamics to certain point, further works can be carried out to extend beyond what have been so far understood.

While regimes for a range of Galilei number were identified in present study focusing on finding when the path instability occurs, further study can be carried out beyond the highest Galilei number used in this study. Since spiraling sub-regime isn't fully explored in present study, further increment of Galilei number might give insight to more interesting phenomena of bubble dynamics.

In this study, Galilei number is varied while maintaining other three conditional parameters at constant values. Galilei number can be kept constant while varying Eötvös number given rest two conditional parameters are held constant. Phase diagrams presented by Tripathi et al. [19] and Cano-Lozano et al. [17] might be a good place for fixating the parameters to begin with as their works are based on unbounded condition and it would be easier to compare the results of bounded condition with unbounded condition.

Instead of two-wall effect as studied in this thesis, three-wall effect by adding the bottom wall as well can be an investigation to seek out. This would give an insight of whether the additional wall has any unwarranted impact on the present investigated bubble dynamics.

Bubble bounded by an axi-symmetric domain can be a study worth carrying out. But the current tool viz. Basilisk used here doesn't yet have the function to define complex domain in three-dimension yet for this kind of interfacial flows. It is yet to be seen whether they can incorporate the feature in near future. However, two-dimensional study of such configuration is possible to simulate in Basilisk.

# References

- [1] A. W. G. de Vries, "Path and wake of a rising Bubble," PhD Thesis, 2001.
- [2] M. K. TrIpathi, "Rising bubbles and falling drops," PhD Thesis, 2015.
- [3] C. D. Ohl, A. Tijink and A. Prosperetti, "The added mass of an expanding bubble," *Journal of Fluid Mechanics*, vol. 482, pp. 271 - 290, 2003.
- [4] W. L. Haberman and R. K. Morton, "An experimental investigation of the drag and shape of air bubbles rising in various liquids," *Tech. Rep. No. DTMB 802, Publisher: David taylor model basin Washington DC*, 1953.
- [5] P. G. Saffman, "On the rise of small air bubbles in water," *Journal of Fluid Mechanics*, vol. 1, no. 3, pp. 249-275, 1956.
- [6] R. A. Hartunian and W. Sears, "On the instability of small gas bubbles moving uniformly in various liquids," *Journal of Fluid Mechanics*, vol. 3, no. 1, p. 27–47, 1957.
- [7] H. Tsuge and S. Hibino, "The onset conditions of oscillatory motion of single gas bubbles rising in various liquids," *Journal of Chemical Engineering of Japan*, vol. 10, no. 1, pp. 66-68, 1977.
- [8] D. Bhaga. and M. E. Weber, "Bubbles in viscous liquids: shapes, wakes and velocities," *Journal of Fluid Mechanics*, vol. 105, no. 1, p. 61–85, 1981.
- [9] P. C. Duineveld, "Rise velocity and shape of bubbles in pure water at high Reynolds number," *J. Fluid Mech.*, vol. 292, p. 325, 1995.
- [10] A. Tomiyama, G. Celata, S. Hosokawa and S. Yoshida, "Terminal velocity of single bubbles in surface tension force dominant regime.,," *International Journal of Multiphase Flow*, vol. 28, p. 1497–1519, 2002.
- [11] C. Veldhuis, A. Biesheuvel and L. V. Wijngaarden, "Shape oscillations on bubbles rising in clean and in tap water," *Physics of Fluids*, vol. 20, no. 4, p. 040705, 2008.
- [12] R. Zenit and J. Magnaudet, "Measurements of the streamwise vorticity in the wake of an oscillating bubble," *International Journal of Multiphase Flow*, vol. 35, no. 2, pp. 195-203, 2009.
- [13] A. d. Vries, A. Biesheuvel and L. v. Wijngaarden, "Notes on the Path and Wake of a Gas Bubble Rising in Pure Water," *International Journal of Multiphase Flow*, vol. 28, no. 11, pp. 1823-1835, 2002.
- [14] B. Bunner and G. Tryggvason, "Direct numerical simulations of three-dimensional bubbly flows," *Physics of Fluids*, vol. 11, no. 8, p. 1967–1969, 1999.
- [15] J. Magnaudet and G. Mougin, "Wake instability of a fixed spheroidal bubble.,," *Journal of Fluid Mechanics*, vol. 572, p. 311–337, 2007.
- [16] J. C. Cano-Lozano, P. Bohorquez and C. Martínez-Bazán, "Wake instability of a fixed axisymmetric bubble of realistic shape," *International Journal of Multiphase Flow*, vol. 51, p. 11–21, 2013.

- [17] J. C. Cano-Lozano, C. Martínez-Bazán, J. Magnaudet and J. Tchoufag, "Paths and wakes of deformable nearly spheroidal rising bubbles close to the transition to path instability," *Physical Review Fluids*, vol. 1, p. 053604., 2016.
- [18] J. C. Cano-Lozano, J. Tchoufag, J. Magnaudet and C. Martínez-Bazán, "A global stability approach to wake and path instabilities of nearly oblate spheroidal rising bubbles," *Physics of Fluids*, vol. 28, no. 1, p. 014102, 2016.
- [19] M. K. Tripathi, K. C. Sahu and R. Govindarajan, "Dynamics of an initially spherical bubble rising in quiescent liquid," *Nature Communications*, vol. 6, p. 6268, 2015.
- [20] R. Krishna, M. I. Urseanu, J. M. Van Baten and J. Ellenberger, "Wall effects on the rise of single gas bubbles in liquids," *International Communications in Heat and Mass Transfer*, vol. 26, no. 6, p. 781–790., 1999.
- [21] F. Takemura, S. Takagi, J. Magnaudet and Y. Matsumoto, "Drag and lift forces on a bubble rising near a vertical wall in a viscous liquid," *Journal of Fluid Mechanics*, vol. 461, p. 277–300, 2002.
- [22] B. Figueroa-Espinoza, R. Zenit and D. Legendre, "The effect of confinement on the motion of a single clean bubble," *Journal of Fluid Mechanics*, vol. 616, p. 419–443, 2008.
- [23] H. Jeong and H. Park, "Near-wall rising behaviour of a deformable bubble at high reynolds number.," *Journal of Fluid Mechanics*, vol. 771, p. 564–594, 2015.
- [24] Y. Zhang, S. Dabiri, K. Chen and Y. You, "An initially spherical bubble rising near a vertical wall," *International Journal of Heat and Fluid Flow*, vol. 85, p. 108649, 2020.
- [25] J. Tchoufag, J. Magnaudet and D. Fabre, "Linear instability of the path of a freely rising spheroidal bubble," *Journal of Fluid Mechanics*, vol. 751, pp. 754 R4-1, 2014.
- [26] J. Tchoufag, D. Fabre and J. Magnaudet, "Global linear stability analysis of the wake and path of buoyancy driven disks and thin cylinders," *Journal of Fluid Mechanics*, vol. 740, pp. 278–311, 2014.
- [27] J. Hua and J. Lou, "Numerical simulation of bubble rising in viscous liquid," *Journal of Computational Physics*, vol. 222, no. 2, pp. 769-795, 2007.
- [28] D. Gaudlitz and N. Adams, "Numerical investigation of rising bubble wake and shape variations," *Physics of Fluids*, vol. 21, p. 122102, 2009.
- [29] D. Enright, R. Fedkiw, J. Ferziger and I. Mitchell, "A hybrid particle level set method for Improved Interface capturing," *Journal of Computational Physics*, vol. 183, no. 1, pp. 83-116, 2002.
- [30] S. Osher and R. P. Fedkiw, "Level Set Methods: An overview and some recent results," *Journal of Computational Physics*, vol. 169, no. 2, pp. 463-502, 2001.
- [31] D. Sharaf, A. Premlata, M. K. Tripathi, B. Karri and K. C. Sahu, "Shapes and paths of an air bubble rising in quiescent liquids," *Physics of Fluids*, vol. 29, p. 122104, 2017.

- [32] F. Takemura and J. Magnaudet, "The transverse force on clean and contaminated bubbles rising near a vertical wall at moderate reynolds number," *Journal of Fluid Mechanics*, vol. 495, p. 235–253., 2003.
- [33] A. Zaruba, D. Lucas, H. M. Prasser and T. Höhne, "Bubble-wall interactions in a vertical gas–liquid flow: Bouncing, sliding and bubble deformations," *Chemical Engineering Science*, vol. 62, no. 6, p. 1591–1605, 2007.
- [34] S. Popinet, "<http://basilisk.fr/>," [Online]. Available: <http://basilisk.fr/>. [Accessed April 2022].
- [35] R. R. Chowdhury, "Higher-order adaptive methods for fluid-dynamics," PhD Thesis, 2019.
- [36] M. J. Berger and P. Colella, "Local adaptive mesh refinement for shock hydrodynamics," *Journal of Computational Physics*, vol. 82, no. 1, pp. 64-84, 1989.
- [37] W. Coirier, "An Adaptively-Refined, Cartesian, Cell-Based Scheme for the Euler and Navier-Stokes Equations.," Computer Science, 1994.
- [38] L. H. Howell and J. Bell, "An adaptive-mesh projection method for viscous Incompressible flow," *SIAM Journal on Scientific Computing*, vol. 18, no. 4, 1997.
- [39] A. M. Khokhlov, "Fully Threaded Tree Algorithms for Adaptive Refinement Fluid Dynamics Simulations," *Laboratory for Computational Physics and Fluid Dynamics, Code 6404, Naval Research Laboratory, Washington, DC 220375*, 1997.
- [40] A. v. Hooft, "<http://basilisk.fr/>," [Online]. Available: [http://basilisk.fr/sandbox/Antoonvh/The\\_Tree\\_Grid\\_Structure\\_in\\_Basilisk](http://basilisk.fr/sandbox/Antoonvh/The_Tree_Grid_Structure_in_Basilisk). [Accessed April 2022].
- [41] S. Popinet, "A quadtree-adaptive multigrid solver for the Serre–Green–Naghdi equations," *Journal of Computational Physics*, vol. 302, pp. 336-358, 2015.
- [42] S. Popinet, "<http://basilisk.fr/>," [Online]. Available: <http://basilisk.fr/Basilisk%20C#fields-and-stencils>. [Accessed April 2022].
- [43] S. Popinet, "<http://basilisk.fr/>," [Online]. Available: <http://basilisk.fr/Basilisk%20C#boundary-conditions>. [Accessed April 2022].
- [44] A. J. Chorin, "Numerical Solution of the Navier-Stokes Equations," *Mathematics of Computation*, vol. 22, no. 104, pp. 745-762, 1968.
- [45] S. Popinet, "Gerris: a tree-based adaptive solver for the incompressible Euler equations in complex geometries," *Journal of Computational Physics*, vol. 190, no. 2, pp. 572-600, 2003.
- [46] J. B. Bell, P. Colella and H. M. Glaz, "A second-order projection method for the incompressible navier-stokes equations," *Journal of Computational Physics*, vol. 85, no. 2, pp. 257-283, 1989.
- [47] S. Popinet, "<http://basilisk.fr/>," [Online]. Available: <http://basilisk.fr/src/navier-stokes/centered.h>. [Accessed April 2022].
- [48] R. Scardovelli and S. Zaleski, "Direct numerical simulation of free-surface and interfacial flow," *Annual review of fluid mechanics*, vol. 31, pp. 567-603, 1999.

- [49] E. Aulisa, S. Manservisi, R. Scardovelli and S. Zaleski, "Interface reconstruction with least-squares fit and split advection in three-dimensional Cartesian geometry," *Journal of Computational Physics*, vol. 225, no. 2, p. 2301–2319, 2007.
- [50] T. D. Taylor and A. Acrivos, "On the deformation and drag of a falling viscous drop at low Reynolds number," *Journal of Fluid Mechanics*, vol. 18, no. 3, pp. 466-476, 1964.
- [51] M. R. Ansari and M. E. Nimvari, "Bubble viscosity effect on internal circulation within the bubble rising due to buoyancy using the level set method," *Annals of Nuclear Energy*, vol. 38, no. 12, pp. 2770-2778, 2011.
- [52] S. Popinet, "<http://basilisk.fr/>," [Online]. Available: <http://basilisk.fr/src/examples/bubble.c>. [Accessed April 2022].
- [53] B. Yang and A. Prosperetti, "Linear stability of the flow past a spheroidal bubble," *Journal of Fluid Mechanics*, vol. 582, pp. 53-78, 2007.